TECHNISCHE UNIVERSITÄT DRESDEN

Leibniz-Institut
für Festkörper- und
Werkstofforschung
Dresden
IFW

Valence changes at interfaces and surfaces investigated by X-ray spectroscopy

Dissertation

zur Erlangung des akademischen Grades
Doctor rerum naturalium
(Dr. rer. nat.)

vorgelegt
der Fakultät Mathematik und Naturwissenschaften
der Technischen Universität Dresden

von

Diplom-Physiker Uwe Treske
geboren am 02.11.1985 in Lutherstadt Wittenberg

Die Dissertation wurde in der Zeit von Januar 2011
bis September 2014 am Leibniz Institut für Festkörper
und Werkstoffforschung Dresden angefertigt.

Abstract

In this thesis valence changes at interfaces and surfaces of $3d$ and $4f$ systems are investigated by X-ray spectroscopy, in particular X-ray photoemission (XPS), X-ray absorption (XAS) and resonant photoemission spectroscopy (ResPES). The first part addresses the electronic properties of the oxides $LaAlO_3$, $LaGaO_3$ and $NdGaO_3$ grown by pulsed laser deposition on TiO_2-terminated $SrTiO_3$ single crystals along (001)-direction. These polar/non-polar oxide interfaces share an insulator to metal phase transition as a function of overlayer thickness including the formation of an interfacial two dimensional electron gas. The nature of the charge carriers, their concentration and spatial distribution, and the band alignment near the interface are studied in a comparative manner and evaluated quantitatively. Irrespective of the different overlayer lattice constants and bandgaps, all the heterostructures behave similarly. Rising Ti^{3+} concentration is monitored by $Ti\,2p$ XPS, $Ti\,L$-edge XAS and by resonantly enhanced $Ti\,3d$ excitations in the vicinity of E_F (ResPES) when the layer number n increases. This indicates that the active material is in all cases a near interface $SrTiO_3$ layer of $\sim 4\,nm$ thickness. Band bending in $SrTiO_3$ occurs but no electric field is detected inside the polar overlayers. Essential aspects of the findings are captured by scenarios where the polar forces are alleviated by surface defect creation or the separation of photon generated electron-hole pairs in addition to the electronic reconstruction at $n = 4$ unit cells layer thickness.

Furthermore, deviations from an abrupt interface are found by soft X-ray photoemission spectroscopy which may affect the interface properties. The surface sensitivity of the measurements has been tuned by varying photon energy and emission angle. In contrast to the core levels of the other elements, the $Sr\,3d$ line shows an unexpected splitting for higher surface sensitivity, signaling the presence of a second strontium component. From a quantitative analysis it is concluded that during the growth process a small amount of Sr atoms diffuse away from the substrate and segregate at the surface of the heterostructure, possibly forming strontium oxide.

In the second part of this thesis the heavy fermion superconductors $CeM In_5$ (M = Co, Rh, Ir) are investigated by temperature- and angle-dependent XPS. In this material class the subtle interplay between localized $Ce\,4f$ and itinerant valence electrons dominate the electronic properties. The $Ce\,3d$ core level has a very similar shape for all three materials and is indicative of weak f-hybridization. The spectra are analyzed using a simplified version of the Anderson impurity model, which yields a $Ce\,4f$ occupancy that is larger than 0.9. The temperature dependence shows a continuous, irreversible and exclusive broadening of the $Ce\,3d$ peaks, due to oxidation of Ce at the surface.

Kurzdarstellung

In der vorliegenden Dissertation werden Valenzänderungen an Grenzflächen und Oberflächen mittels Verfahren der Röntgenspektroskopie untersucht, zu denen die Röntgenphotoelektronen- (XPS), die Röntgenabsorptions- (XAS) und die resonante Photoelektronenspektroskopie (ResPES) gehören. Kapitel 3 behandelt die elektronischen Eigenschaften der Oxide $LaAlO_3$, $LaGaO_3$ und $NdGaO_3$, welche mittels Laserdeposition (PLD) auf TiO_2-terminierte $SrTiO_3$ Einkristalle entlang (001)-Richtung gewachsen wurden. Diese polaren/nicht-polaren Oxidgrenzflächen weisen einen Isolator-Metall Phasenübergang als Funktion der Schichtdicke auf, bei dem sich ein zwei dimensionales Elektronengas an der Grenzfläche bildet. Die Eigenschaften dieser Ladungsträger, deren Konzentration und räumliche Ausdehnung, sowie der Verlauf der Energiebänder an der Grenzfläche werden vergleichend untersucht und quantitativ bestimmt. Es wird gezeigt, dass sich die drei untersuchten Grenzflächen, trotz unterschiedlicher Gitterkonstanten und Energiebandlücken, ähnlich verhalten. Das mit der Schichtdicke ansteigende Ti^{3+} Signal wird im $Ti\,2p$ XPS, $Ti\,L$-Kante XAS und durch die resonant verstärkten $Ti\,3d$ Anregungen nahe E_F (ResPES) nachgewiesen. Daraus lässt sich schlussfolgern, dass in allen Fällen eine $SrTiO_3$ Schicht mit einer Dicke von $\sim 4\,nm$ der eigentlich aktive Bereich ist. Im $SrTiO_3$ tritt eine Bandverbiegung auf, ein elektrisches Feld in der polaren Deckschicht kann jedoch nicht nachgewiesen werden. Grundlegende Aspekte dieser Ergebnisse sind in einem Szenario vereinbar, bei dem die polaren Kräfte durch die Entstehung von Oberflächendefekten, durch die Trennung von photoneninduzierten Elektronen-Lochpaaren und durch eine elektronische Umordnung bei 4 uc Schichtdicke eliminiert werden. Des Weiteren werden Abweichungen von einer abrupten Grenzfläche mittels weich-Röntgenphotoelektronenspektroskopie festgestellt, die die Grenzflächeneigenschaften beeinflussen können. Für oberflächenempfindlichere Messbedingungen zeigt die $Sr\,3d$ Anregung, im Gegensatz zu Rumpfniveaus anderer Elemente, eine unerwartete Aufspaltung, was nur durch das Vorhandensein einer zweiten chemischen Strontiumkomponente zu erklären ist. Aus quantitativen Betrachtungen lässt sich schließen, dass einige Strontiumatome während des Wachstums an die Oberfläche diffundieren und möglicherweise Strontiumoxid gebildet wird.

Der zweite Schwerpunkt der vorliegenden Arbeit ist die Untersuchung von Schwer-Fermionen Supraleitern $CeM\text{In}_5$ (M = Co, Rh, Ir) mittels temperatur- und winkelabhängiger XPS. Bei dieser Materialklasse dominiert das feine Zusammenspiel zwischen lokalisierten $Ce\,4f$ und frei beweglichen Leitungselektronen die elektronischen Eigenschaften. Das $Ce\,3d$ Rumpfniveauspektrum besitzt für die drei Materialien eine sehr ähnliche Form, die auf eine schwache f-Hybridisierung schließen lässt. Die Spektren werden mittels einer vereinfachten Version des Anderson-Impurity Modells analysiert, wobei sich eine $Ce\,4f$ Besetzung von mehr als 0,9 ergibt. Die Temperaturabhängigkeit zeigt eine kontinuierliche und irreversible Verbreiterung ausschließlich für die $Ce\,3d$ Anregung, dieser Umstand kann einer Oxidation der reaktiven Ceratome an der Oberfläche zugeordnet werden.

Contents

Acronyms

Θ	emission angle
$h\nu$	photon energy
2DEG	two-dimensional electron gas
ARPES	angle-resolved photoemission spectroscopy
BESSY II	Berliner Elektronenspeicherring-Gesellschaft für Synchrotronstrahlung
C-AFM	conducting tip atomic force microscope
CVD	chemical vapor deposition
DOS	density of states
EELS	electron energy loss spectroscopy
FWHM	full width half maximum
IIR	integrated intensity ratio
IMFP	inelastic mean free path
λ	inelastic mean free path
LAO	lanthanum aluminate ($LaAlO_3$)
LAO/STO	$LaAlO_3$ grown on TiO_2-terminated $SrTiO_3$
LGO	lanthanum gallate ($LaGaO_3$)
MBE	molecular beam epitaxy
NGO	neodymium gallate ($NdGaO_3$)
PES	photoemission spectroscopy
PEY	partial electron yield
PLD	pulsed laser deposition

|	
PVD	physical vapor deposition
ResPES	resonant photoemission spectroscopy
RHEED	reflection high-energy electron diffraction
STO	strontium titanate ($SrTiO_3$)
TEY	total electron yield
uc	unit cell
UHV	ultra-high vacuum
UPS	ultraviolet photoemission spectroscopy
VBO	valence band offset
XAS	X-ray absorption spectroscopy
XLD	X-ray linear dichroism
XPS	X-ray photoemission spectroscopy
XRD	X-ray diffraction

1 Introduction

Daily life in a modern society without computer technology is difficult to imagine. The fabrication of electronic devices like laptops, smart phones or navigation systems rests on the progress in semiconductor technology, which became a key technology in the 20th century. Conventional semiconductors consist either of pure elements or binary compounds with four valence electrons like silicon, germanium, gallium arsenide, indium phosphide, in particular they are made of elements found in the p block of the periodic table. The position in the periodic table indicates that delocalized half-filled sp orbitals define their chemical and electronic properties. The ongoing development, improvement and miniaturization of electronic devices consider also alternative materials which prospectively can complement or replace the silicon technology. One aspect is the investigation and integration of functional materials specialized for a certain purpose. Among them are correlated electron systems showing exotic physical properties absent in conventional semiconductors, for instance colossal magnetoresistance [1–3], multiferroic behavior [4], high temperature superconductivity [5] or piezoelectricity [6]. These and further phenomena are caused by electron-electron interactions of partly occupied d and f shells with rather localized orbitals and narrow energy bands. In contrast to the sp band in conventional semiconductors the wave function of d and f electrons are stronger confined to the atomic nucleus leading to a decreased average distance between electrons of double occupied orbitals. Therefore treating an electron in a material as charged particle in the mean field generated by the sea of all other electrons is no longer valid. Each electron has a complex influence on its neighbors – they are correlated. The subtle interplay of localized electrons leads to the manifold intriguing properties of this material class, which can be used for example to functionalize integrated circuits.

To manufacture correlated electron materials one has to extend the elemental composition including transition metals, lanthanides and actinides with partly filled d and f orbitals. Transition metal oxides, a huge material class showing electronic correlations, attracted much interest in the past. Despite a strong ionic bonding between oxygen and the transition metal, they include not only insulators but also metals and superconductors. Often insulator-metal phase transitions are induced by varying temperature, pressure or

doping level. There is a large variety of transition metal compounds and depending on their crystal structure and elemental composition one can stabilize different phases.

In semiconductors the active parts are actually the interfaces as it was highlighted by Herbert Kroemer in his famous Nobel Lecture with the phrase "the interface is the device". Even the interface between two correlated electron materials can exhibit entirely unexpected properties absent in both bulk constituents. Therefore the development and investigation of high quality interfaces are essential for possible future applications and a topic of current science. In former years, remarkable progress in pulsed laser deposition [7, 8] and molecular beam epitaxy [9] enabled the epitaxial film growth of various compounds on certain substrates with high quality.

One famous example is the formation of a highly-mobile two dimensional electron gas which occurs at the interface between the two insulating transition metal oxides lanthanum aluminate and strontium titanate [10]. The origin of the interface metallicity and its properties is still under passionate debates. Several mechanisms might play a role, e.g. the formation of a potential well caused by polar discontinuities [11], extrinsic doping by oxygen vacancies and cation intermixing [10, 12–14] as well as structural distortions [15, 16]. The charge carriers in these systems occupy $Ti\,3d$ orbitals at the strontium titanate side of the interface [17] and reveal therefore correlation effects. The transport properties can be controlled by electric and magnetic fields [18, 19], temperature [10], chemical reactions on the surface [20] and light illumination [21] enabling a possible application in electronic devices or sensors. In 2008, Cen *et al.* reported about writing and erasing conducting nanowires by a voltage-biased tip of an atomic force microscope [22]. Fig. 1.1 illustrates their experimental setup with a nanowire of only 3.3 nm width, which is well below the current technology node in semiconductor industries.
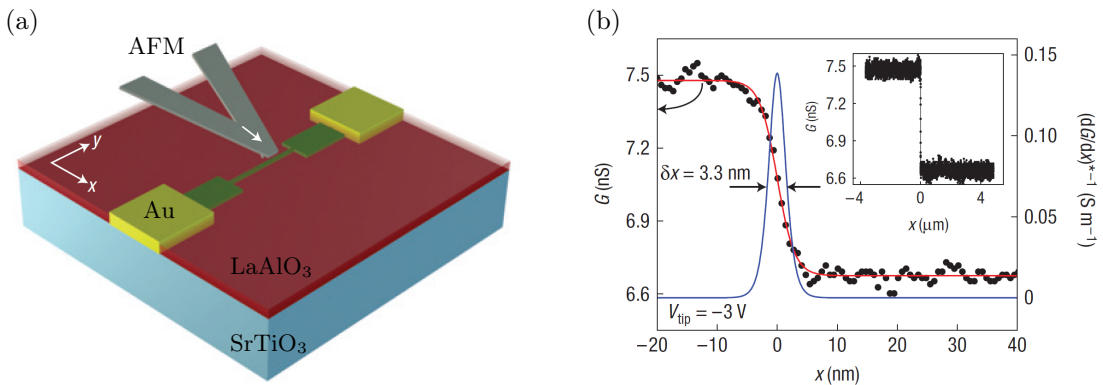
Figure 1.1: (a) Schematic diagram of the experimental set-up for writing and erasing a conducting nanowire at the $LaAlO_3/SrTiO_3$ interface by a voltage-biased atomic force microscope tip. (b) Change in conductance G while moving the tip with a negative bias-voltage perpendicular to the nanowire to estimate its width. Taken from [22].

Another exciting material class exhibiting even stronger correlation effects than present in transition metals are heavy fermion materials. These are intermetallic alloys made of lanthanides or actinides. Their f electrons interact with the sea of conduction electrons forming quasiparticles with for instance up to three orders of magnitude higher effective masses than for normal metals, first discovered in $CeAl_3$ in 1975 [23]. By varying the lattice parameters one can influence this interaction and study the resulting properties. $CeM In_5$ is a quasi 2D heavy fermion family [24], whose lattice constants can be tuned by the substitution of the transition metal M with Co, Rh, and Ir [24–26]. Furthermore they exhibit unconventional superconductivity, which cannot be described by BCS-theory.

Both, the interfaces between transition metal oxides and the surface of cleaved heavy fermion materials are subjects of this thesis. They have been investigated by three different types of X-ray spectroscopic techniques, namely X-ray photoemission spectroscopy, resonant photoemission spectroscopy and X-ray absorption spectroscopy. These nondestructive techniques are in principle able to study the properties of interfaces and the underlying chemical and physical mechanisms. Due to the high surface sensitivity of these experimental methods thin layers can be investigated. Additionally, one can tune the surface sensitivity by varying the detection angle, detection mode or photon energy, in order to disentangle the signals coming from the surface, interface or bulk. The measurements have been carried out in standard laboratory photoemission setups at the Leibniz Institute for Solid State and Materials Research Dresden (IFW Dresden) and at the synchrotron facility BESSY in Berlin.

In chapter 2, the applied X-ray spectroscopic techniques and experimental setups are introduced. Chapter 3 addresses the insulator-metal phase transition at polar/non-polar transition metal oxide interfaces. Different interfaces were investigated to ascertain and to distinguish between universal and material specific parameters. After the introduction, this chapter is divided in a first part dealing with growth dependent Sr diffusion and a second part which is related to the intrinsic formation and properties of the interface conductivity. The subtle interplay between strongly localized electrons and itinerant conduction electrons in the heavy fermion materials $CeM In_5$ (M = Co, Rh, and Ir) are characterized in chapter 4 by X-ray photoemission spectroscopy. Important hybridization parameters have been extracted from the data. Additionally, specific surface properties of these compounds are discussed.

2 Experimental and theoretical background

The fields of surface physics and surface chemistry serve as a basis for the investigations in this thesis. The history of both fields is closely linked to the development of analysis methods, which utilize electrons carrying characteristic information of the studied materials. Electrons exhibit key advantages in comparison with other measurable particles such as ions, photons or neutrons [27]:

- Electrons have a mean free path of a few angstrom (Å) depending on their kinetic energy.

- Energy and momentum of fundamental surface excitations are easily accessible via electrons.

- Electrons can easily be de- and accelerated or focused by means of electric fields and in case of the latter also by magnetic fields.

- Various sensitive tools are available to visualize and detect electrons.

Several *X-ray spectroscopy* methods benefit from these properties and are indispensable for the field of surface physics and surface chemistry. Especially *photoemission spectroscopy* (PES) and *X-ray absorption spectroscopy* (XAS), which rest on the photoelectric effect and auger effect, are of particular importance in this context. They are applied extensively to investigate electronic and chemical properties of gases, liquids, solids as well as surfaces and interfaces. Both, PES and XAS, exhibit a lot of information on the ground state and various physical properties of the analyzed materials and of course in combination they provide even more insights.

PES and XAS, with their various methods of measurements, have been used to investigate several material systems, that are discussed in this thesis. In the following chapter a detailed discussion about the physical fundamentals of these techniques is given.

2.1 Photoemission spectroscopy

2.1.1 Photoelectric effect

In 1887, H. Hertz and W. Hallwachs reported that metal surfaces emit electrons when they are exposed to electromagnetic radiation. Sufficient short wavelengths in the range of visible and ultra-violet light are necessary to observe this effect [28]. First, A. Einstein described these observations theoretically in 1905, therefore he was honored with the Nobel Prize in 1921 [29]. He interpreted the photoionization process quantum mechanically, analogous to the description of black body radiation in thermal equilibrium by M. Planck (*Planck's law*, Planck constant h). Light has both wave and particle character and a certain energy $E_{\mathrm{photon}} = h\nu$ depending on its frequency ν. Electrons in a solid with binding energy E_{B} get excited by absorption of such light quanta and can escape from the surface, if the photon energy overcomes the work function Φ of the solid. The residual energy is transformed into kinetic energy of the excited electron E_{kin} by the following equation:

$$E_{\mathrm{kin}} = h\nu - E_{\mathrm{B}} - \Phi \ . \tag{2.1}$$

This process is called photoelectric effect and is essential for PES, which is classified in *ultraviolet photoemission spectroscopy* (UPS) and *X-ray photoemission spectroscopy* (XPS) depending on the used photon energy.

2.1.2 Three-step model

The photoemission of an electron is a complex and coherent process that comprises many physical effects. For an easier interpretation C. Berglund und W. Spicer divided the photoemission into three steps (1960):

I photoabsorption,

II path to the sample surface,

III escape from sample surface.

The *three-step model* is shown schematically in Fig. 2.1 and will be explained in more detail in the following sections [30–35].
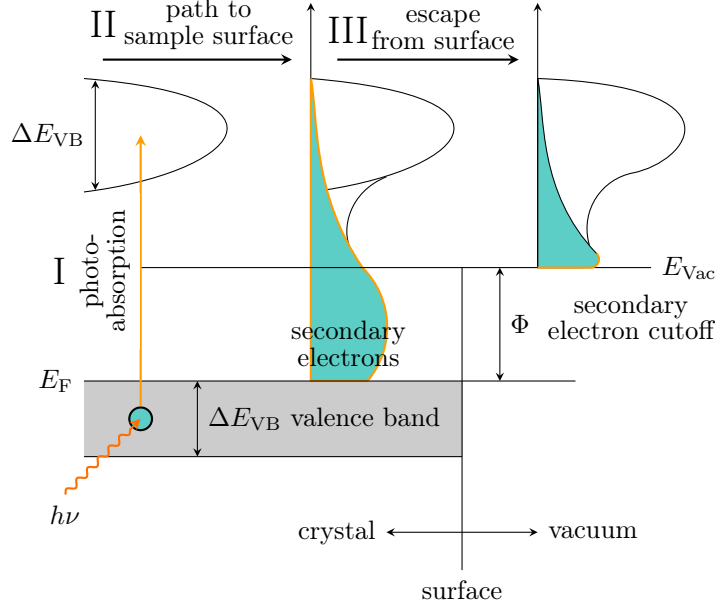
Figure 2.1: Sketch of the *three-step model* of photoemission, according to [32].

I Photoabsorption – cross section

The interaction between a photon and an electron can be calculated by substituting the momentum operator $\hat{\boldsymbol{p}}$ in the Hamiltonian $\hat{H}$ with:

$$\hat{\boldsymbol{p}} \longrightarrow (\hat{\boldsymbol{p}} - \frac{e}{c}\boldsymbol{A}). \tag{2.2}$$

In this way the effect of the electromagnetic field (vector potential $\boldsymbol{A}$) on the momentum of the electron is taken into account. Note that spin-orbit coupling ($\sim \hat{\boldsymbol{S}}\cdot\hat{\boldsymbol{L}}$), interaction between spin and magnetic field ($\sim \hat{\boldsymbol{S}}\cdot\boldsymbol{B}$), relativistic corrections (Darwin term $\sim \boldsymbol{E}\cdot\hat{\boldsymbol{p}}$) and any electron exchange correlations are not considered. Then the Hamiltonian can be split into a free particle Hamiltonian $\hat{H}_0$ and a perturbation Hamiltonian $\hat{H}_{\mathrm{Int}}$:

$$\hat{H} = \frac{1}{2m}(\hat{\boldsymbol{p}} - \frac{e}{c}\boldsymbol{A})^2 + eV(\hat{\boldsymbol{r}}) \tag{2.3}$$

$$= \frac{\hat{\boldsymbol{p}}^2}{2m} + eV(\hat{\boldsymbol{r}}) - \frac{e}{2mc}(\boldsymbol{A}\cdot\hat{\boldsymbol{p}} + \hat{\boldsymbol{p}}\cdot\boldsymbol{A} - \frac{e}{c}\boldsymbol{A}^2) \tag{2.4}$$

$$= \hat{H}_0 + \hat{H}_{\mathrm{int}}. \tag{2.5}$$

Furthermore, the $\boldsymbol{A}^2$ can be neglected for low light intensities. The Coulomb gauge claims $\nabla\cdot\boldsymbol{A} = 0$, which enables the commutation $\boldsymbol{A}\cdot\hat{\boldsymbol{p}} = \hat{\boldsymbol{p}}\cdot\boldsymbol{A}$. In the *dipole approximation* it is considered that $\boldsymbol{A}$ is constant over atomic distances. This is valid up to photon energies

in the soft X-ray regime. Thus, the plane wave character of the vector potential can be approximated by $\boldsymbol{A} = \boldsymbol{A}_0 \, \mathrm{e}^{(\mathrm{i}\boldsymbol{kr}-\mathrm{i}\omega t)} \sim \boldsymbol{A}_0 \, \mathrm{e}^{(-\mathrm{i}\omega t)}$ and $\hat{H}_\mathrm{int}$ simplifies to:

$$\hat{H}_\mathrm{int} \;=\; -\frac{e}{mc}\boldsymbol{A}\cdot\hat{\boldsymbol{p}} \approx -\frac{e}{mc}\boldsymbol{A}_0\mathrm{e}^{(-\mathrm{i}\omega t)}\cdot\hat{\boldsymbol{p}} \tag{2.6}$$

$$\approx \;\; \mathrm{e}^{(-\mathrm{i}\omega t)}\hat{\mathcal{H}}_\mathrm{int}\;. \tag{2.7}$$

This enables the treatment of the photon absorption by time-dependent perturbation theory. The transition probabilities from an initial to a final state $w_\mathrm{i\to f}$ during a periodic perturbation is then given by *Fermi's golden rule*:

$$w_\mathrm{i\to f} = \frac{2\pi}{\hbar}\left|\left\langle \Psi_\mathrm{f} \,\middle|\, \hat{\mathcal{H}}_\mathrm{int} \,\middle|\, \Psi_\mathrm{i} \right\rangle\right|^2 \cdot \delta(E_\mathrm{f} - E_\mathrm{i} - h\nu)\;. \tag{2.8}$$

Here Ψ_i and Ψ_f denote the N-particle wave functions of the initial and final state with total energies E_i and E_f, respectively. In this equation the energy conservation is fulfilled due to the delta function δ. The most important quantity in Eq. 2.8 is the transition matrix element $M_\mathrm{f,i}$, that can be rewritten with the help of the commutator relation $[\hat{H}_0, \hat{\boldsymbol{r}}] = \frac{\hbar}{\mathrm{i}m}\hat{\boldsymbol{p}}$ to:

$$M_\mathrm{f,i} = \left|\left\langle \Psi_\mathrm{f} \,\middle|\, \hat{\mathcal{H}}_\mathrm{int} \,\middle|\, \Psi_\mathrm{i} \right\rangle\right| = -\frac{\mathrm{i}e}{\hbar c}\hbar\omega\boldsymbol{A}_0 \cdot \left|\left\langle \Psi_\mathrm{f} \,\middle|\, \hat{\boldsymbol{r}} \,\middle|\, \Psi_\mathrm{i} \right\rangle\right|\;. \tag{2.9}$$

A non-trivial final step is necessary to deal with this problem. In the commonly used *sudden approximation* the N-particle wave functions are factorized into the single electron $|\Phi_\mathrm{i,k}\rangle$, that gets excited from the orbital k and the remaining, passive $(N-1)$ electron system $\left|\Psi_\mathrm{i,k}^{N-1}\right\rangle$. In this limit, the photoemission process is assumed to be fast so that no interaction between photoelectron and the remaining system can happen. The electron is removed instantaneously [32, 34]. Note that this procedure is inappropriate for photoelectrons with low kinetic energies, however it is valid exemplarily in the case of cuprates for photon energies as low as $20\,\mathrm{eV}$ [36]. Then it can be written:

$$\langle \Psi_\mathrm{f} \,|\, \hat{\boldsymbol{r}} \,|\, \Psi_\mathrm{i} \rangle = \langle \Phi_\mathrm{f,k} \,|\, \hat{\boldsymbol{r}} \,|\, \Phi_\mathrm{i,k} \rangle \left\langle \Psi_\mathrm{f,k}^{N-1} \,\middle|\, \Psi_\mathrm{i,k}^{N-1} \right\rangle \tag{2.10}$$

$$= D_\mathrm{f,i}^k \sum_s \tilde{c}_s^k \left\langle \Psi_\mathrm{s,k}^{N-1} \,\middle|\, \Psi_\mathrm{i,k}^{N-1} \right\rangle\;, \tag{2.11}$$

with the one-particle dipole matrix element $D_\mathrm{f,i}^k$. The second term symbolizes the $(N-1)$ electron overlap integral. In fact, $\left|\Psi_\mathrm{f,k}^{N-1}\right\rangle$ is no longer an eigenstate it can be expressed in s eigenstates with the wave functions $\left|\Psi_\mathrm{s,k}^{N-1}\right\rangle$ and energy E_s^{N-1} of the $(N-1)$ electron

system. The total photoemission intensity measured from an electron of the orbital k (or with momentum k) as a function of E_{kin} is thus proportional to the sum:

$$I(k, E_{\mathrm{kin}}) \sim \sum_{\mathrm{f}} w_{\mathrm{i} \to \mathrm{f}}$$

$$\sim \sum_{\mathrm{f}} |D_{\mathrm{f},\mathrm{i}}^k|^2 \sum_{s} |c_{s,\mathrm{i}}^k|^2 \, \delta(E_{\mathrm{kin}} + E_s^{N-1} - E_{\mathrm{i}}^N - h\nu) \,, \qquad (2.12)$$

with $c_{s,\mathrm{i}}^k = \tilde{c}_s^k \left\langle \Psi_{s,k}^{N-1} \,\middle|\, \Psi_{\mathrm{i},k}^{N-1} \right\rangle$ is the probability that the removal of the kth electron from the initial state will leave the $(N-1)$ electron system in the sth excited eigenstate. In the *frozen-orbital limit*, meaning the remaining electron system stays unaffected upon photoemission, one particular $c_{s,\mathrm{i}}^k$ is unity and all others are zero. However, for strongly correlated electron systems many of the $c_{s,\mathrm{i}}^k$ will be different from zero due to strong changes in the system upon electron removal. This results in a main line and additional satellite features in the photoemission spectra [32, 34].

Nevertheless, the main term for the cross section is the one-electron dipole matrix element

$$D_{\mathrm{f},\mathrm{i}} = \langle \mathrm{f} \,|\, \hat{\boldsymbol{r}} \,|\, \mathrm{i} \rangle \,, \qquad (2.13)$$

which is extremely valuable as its quantity can be calculated for selected symmetries of the wave functions and yields dipole selection rules.

The measured photoelectron intensity of a certain orbital is proportional to the cross section σ and consequently also to the transition probability in Eq. 2.12. Therefore the intensity I depends on the initial state and on the radiation energy. Furthermore, the signal intensity is affected by other factors as for example the density of the corresponding atomic species n, the light flux f [photons/cm²s] as well as the efficiency of the spectrometer η [37]:

$$I \sim \sigma \, n \, f \, \eta. \qquad (2.14)$$

II Path to the sample surface

High energetic ultraviolet (UV) light or X-rays penetrate up to several micrometer (μm) beneath the sample surface and are able to excite electrons. The excited electrons propagate through the solid and get scattered elastically and inelastically by electron-electron, electron-phonon or electron-plasmon interactions. This results in a loss of energy and information about their initial state. Hence, the scattered electrons contribute only to the secondary electron background of the spectrum (see Fig. 2.1), which increases with de-

creasing kinetic energy. This effect can be described by the *Beer–Lambert law* (Eq. 2.15), that takes advantage of the energy and material dependent *inelastic mean free path* (λ) of the photoelectrons. According to this exponential damping the differential intensity I coming from an infinitesimal thin layer at depth x below the surface is given by:

$$\mathrm{d}I(x) = I_0 \, \mathrm{e}^{\left(-\frac{x}{\lambda \cos \Theta}\right)} \mathrm{d}x \; . \tag{2.15}$$

Here Θ is the emission angle between surface normal of the sample and the direction to the detector. For $\Theta = 0\,°$ it is called normal emission, see Fig. 2.2.

The number of photoelectrons carrying spectroscopic information decreases with increasing depth x. On the one hand this results unfortunately in a worsening of the signal-to-noise ratio but on the other hand it enables the following advantages of PES:

- surface sensitivity,

- determination of the thickness of a certain organic or inorganic overlayer (see chapter 2.1.4),

- ascertaining the work function Φ of a material due to the secondary electron cutoff.

The utilization of the *Beer–Lambert law* and the required calculation of λ are explained in more detail in section 2.1.4 and 2.1.5, respectively.

III Escape from sample surface

When the photoelectrons reach the sample surface, they have to overcome the potential barrier of the work function Φ, whereby electrons with lower energy are reflected back into the solid. As a result of this, a sharp drop of photoelectron intensity at low kinetic energies can be found. This edge is called *high binding energy* or *secondary electron cutoff*, which is visualized in the third part of Fig. 2.1. The photoelectrons lose kinetic energy perpendicular to the sample surface and therefore only the momentum component parallel to the surface $\boldsymbol{k}_{\mathrm{f}_{\parallel}}$ is conserved (see Fig. 2.3). Afterwards the photoexcited electrons travel through the vacuum and obey the free electron dispersion relation:
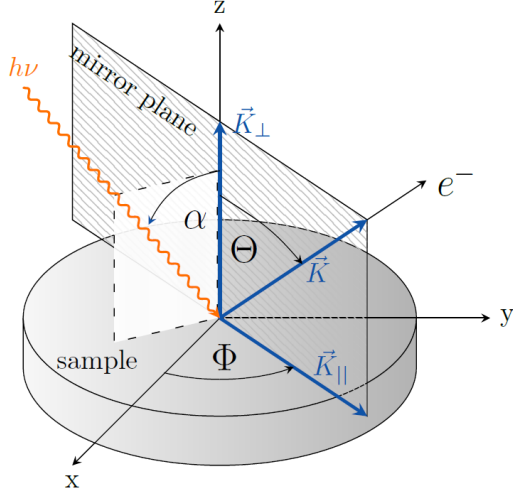
$$E_{\mathrm{kin}} = \frac{\hbar^2 \boldsymbol{K}^2}{2\,m_{\mathrm{e}}} \; , \tag{2.16}$$

with the free electron momentum in vacuum $\boldsymbol{K}$.

The initial wave vector of a *Bloch state* in a crystal $\boldsymbol{k}_{\mathrm{i}}^{\mathrm{Bloch}}$ is equal to the wave vector in the final state $\boldsymbol{k}_{\mathrm{f}}^{\mathrm{Bloch}}$ because of momentum conservation during the photoemission process. If the emission angles Θ and Φ are also detected (Fig. 2.2), one can extract the

band structure parallel to the surface of a single crystal by Eq. 2.17. This is utilized in *angle-resolved photoemission spectroscopy* (ARPES):

$$\boldsymbol{k}_{\mathrm{i}_{||}}^{\mathrm{Bloch}} = \boldsymbol{k}_{\mathrm{f}_{||}}^{\mathrm{Bloch}} = \boldsymbol{K}_{||} = \sqrt{\frac{2\,m_{\mathrm{e}}}{\hbar^2} E_{\mathrm{kin}}}\;\sin\Theta\;. \tag{2.17}$$


Figure 2.2: Geometric illustration of the photoelectric effect including the polar angle Θ and azimuth Φ.
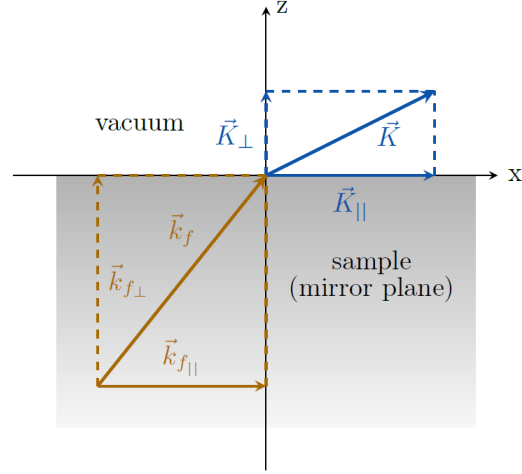
Figure 2.3: Momentum conservation upon photoemission at the sample surface. Only the parallel momentum component $\boldsymbol{K}_{||}$ is conserved, due to the work function.

2.1.3 Interpretation of X-ray photoemission spectra

A photoemission experiment usually starts with a survey spectrum to characterize the sample and its composition. The XPS survey spectrum exemplary for a 3 uc thick $LaAlO_3$ film grown on $SrTiO_3$ is shown in Fig. 2.4. It displays the intensity of photoelectrons depending on their binding energy. Each element has characteristic binding energy regions, where its core levels appear. The main core levels have been identified and labeled in the spectrum. Specific energy regions are measured in detail with a smaller energy step and a lower pass energy of the analyzer to increase the energy resolution. In a hemispherical energy analyzer the pass energy defines the kinetic energy of the electrons, which can pass through the analyzers hemispheres to get detected. With higher pass energy the signal-to-noise ratio improves but the energy resolution worsens. In the following subsections basics for the interpretation of XPS spectra are given.
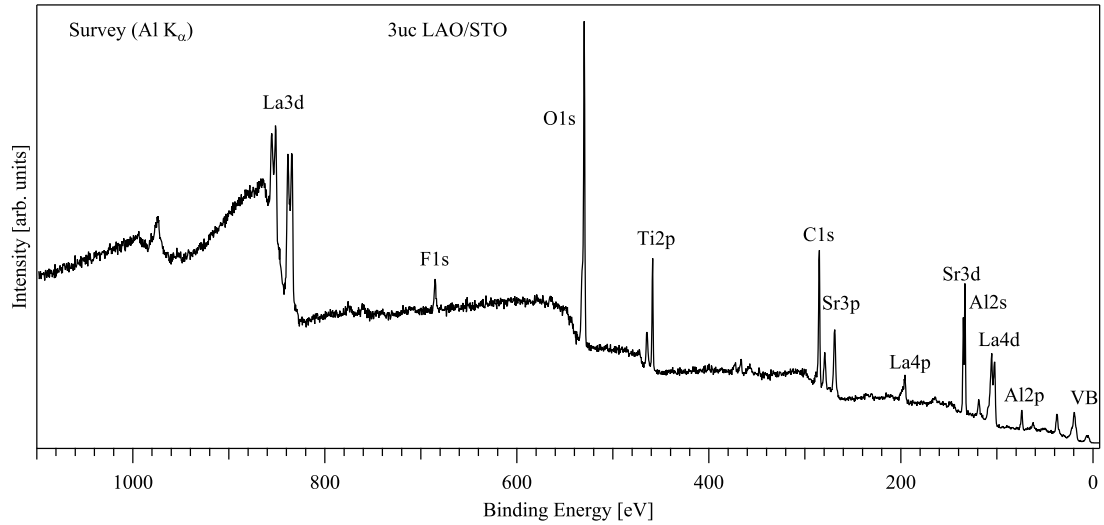
Figure 2.4: XPS survey spectrum of a 3 uc thick $LaAlO_3$ film grown on $SrTiO_3$ and measured with an Al K_α X-ray source ($h\nu = 1486.5$ eV).

Energy calibration

In photoemission the binding energy axis is referred to the Fermi-edge, which is located at
0 eV binding energy. Due to the bandgap, no Fermi-edge is discernible in the valence band
spectra of semiconductors and insulators. If no charging effects occur, the spectra can
be aligned to the Fermi position of a clean metal (gold or silver foil), since the chemical
potentials of the clean metal and the sample are the same when both are electrically
connected. Additionally, certain core levels can be used for XPS to calibrate the energy
axis, e.g. Au $4f_{7/2} \rightarrow 84.0$ eV, Ag $3d_{5/2} \rightarrow 368.27$ eV. If finite charging occurs, i.e. the whole
spectrum is shifted to higher binding energy, the situation becomes more difficult. In this
case the spectrum can be referred to the energy position of the C $1s$ peak of adsorbates
on the sample surface. Usually, a binding energy of 285.0 eV is assumed for this peak.
Because of different chemical compositions of the adsorbates and surface effects, as for
instance interface dipoles, this procedure is less accurate.

Background correction

Inelastic scattering processes lead to a steady increase of secondary electrons with increasing binding energy (decreasing kinetic energy), as shown in Fig. 2.4. This results in
asymmetric peak shapes and can be corrected by various algorithms (linear-, Shirley-,
Touggard-background). Shirley described the most common iterative method [38], which
assumes an energy independent inelastic scattering probability. Then, the background

is proportional to the integrated intensity of the spectrum. Eq. 2.18 elucidates this algorithm for discrete energy steps E_i and measured intensities $I(E_i)$:

$$I'(E_i) = I(E_i) - I(E_0) \left(\frac{\sum\limits_{j>i} I(E_j)}{\sum\limits_{j>0} I(E_j)} \right) \ . \tag{2.18}$$

Chemical shift

The binding energy measured by XPS depends not only on the specific element and orbital but also on the chemical environment of the atom. The energy for the same core level can vary up to a few electron volt (eV) according to its chemical state. Neighboring atoms influence the valence, the electrostatic potential as well as the electronic structure of an atom. Depending on the electronegativity, the wave functions of valence electrons are changed, which leads to a different amount of core hole screening. In general, for larger electronegativity of the neighboring atoms more valence electrons are deducted and due to the lower core hole screening a higher binding energy is measured [39]. This *chemical shift* can cause, besides the binding energy shift, variations in the shape and broadening of the measured peak. A prominent example with large chemical shifts in the C 1s level of differently bonded carbon atoms is shown in Fig. 2.5. In addition to the stoichiometry it is possible to determine the chemical composition of the sample and the valence of certain atoms.
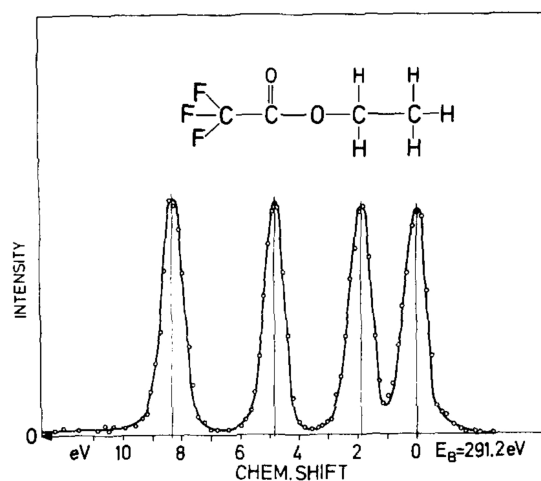
Figure 2.5: Chemical shift in the C 1s core level spectrum of different carbon atoms in ethyl fluoroacetate [40]. Fluor is more electronegative than oxygen and, therefore, increases the binding energy of the bonded carbon atom.

Spin-orbit and multiplet splitting

In XPS, core level excitations are often split into doublets or into even more peaks. Primarily, two processes are responsible for the appearance of such multiplet structures:

- the spin-orbit coupling (LS coupling),

- the spin-spin coupling.

For orbitals with non-zero angular momentum ($l > 0$) the spin ($s = 1/2$) of the core hole couples to its angular momentum. Two final states can occur with total momentum of $j = |l \pm s| = |l \pm \frac{1}{2}|$. The final state with smaller total momentum is energetically favored and appears at higher binding energy. The multiplicity $m = 2j + 1$ is the number of electronic states with equal total momentum. The intensity ratio of the doublet is defined by the orbital momentum of the measured excitation, shown in Eq. 2.19 [37], and can help to identify the corresponding element. In Tab. 2.1 the intensity ratios for orbital momentums up to $l = 3$ are given.

$$\frac{I_{j=l-s}}{I_{j=l+s}} = \frac{2(j - \frac{1}{2})}{2(j + \frac{1}{2})} = \frac{l}{l+1} \tag{2.19}$$

Table 2.1: Parameters of the spin-orbit coupling [37].

orbital	momentum l	spin s	total momentum $j = |l \pm s|$		intensity ratio $2j + 1$
s	0	$1/2$	$1/2$		-
p	1	$1/2$	$1/2$	$3/2$	1:2
d	2	$1/2$	$3/2$	$5/2$	2:3
f	3	$1/2$	$5/2$	$7/2$	3:4

Analogous splittings were found in s orbitals of heavy elements [32], which can be ascribed to spin-spin interactions between core hole and unpaired electrons in not-fully filled shells. Both, spin-orbit and spin-spin interactions, can occur at the same time for certain elements leading to complex peak shapes [41]. Further satellite peaks and energy shifts can appear in core level spectroscopy, which can be solely explained by treating the photoemission process as sophisticated many-body problem. Such final-state effects have been already introduced within the sudden approximation (Eq. 2.12).

2.1.4 Angle-resolved X-ray photoemission spectroscopy

Depth-depending stoichiometry profiles or overlayer thicknesses of structured samples can be determined by angle-resolved X-ray photoemission spectroscopy. In section 2.1.2 the high surface sensitivity of XPS was already mentioned. In the *Beer–Lambert law* (Eq. 2.15) it is obvious that the XPS intensity of a certain element from a thickness x depends also on the relative orientation of the sample with respect to the analyzer. For *grazing emission*, an emission angle Θ close to $90\,°$, the photoelectrons from a deeper layer have to travel for a longer path through the sample in order to reach the vacuum. This results in a reduced photoelectron intensity from the bulk, i.e. the surface sensitivity is enhanced. For homogeneous samples with abrupt interfaces parallel to the surface plane one can take advantage of this effect in several ways. The theoretical basis can be directly derived from the integration of the *Beer–Lambert law*.
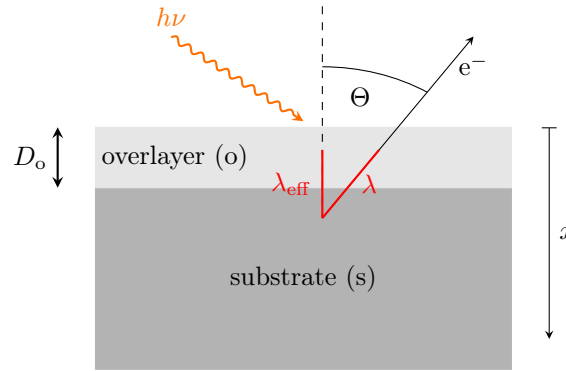
Figure 2.6: Schematic sample configuration for an angle resolved XPS experiment. The photoemission intensities of the substrate and overlayer are given in Eq. 2.20 – 2.22 depending on the emission angle Θ.

A realistic example is shown in Fig. 2.6. Assuming a grown overlayer (o) on top of a substrate (s) with both having a known homogeneous composition and an abrupt interface in between, the intensity for a species of the overlayer I_o and substrate I_s is given by:

$$I_\mathrm{o} \sim \sigma_\mathrm{o}\,\rho_\mathrm{o} \int_0^{D_\mathrm{o}} \mathrm{e}^{\frac{-x}{\lambda_\mathrm{o,o}\ \cos\Theta}}\ \mathrm{d}x = I_\mathrm{o}^\infty\,(1 - \mathrm{e}^{\frac{-D_\mathrm{o}}{\lambda_\mathrm{o,o}\ \cos\Theta}}) \tag{2.20}$$

$$I_\mathrm{s} \sim \sigma_\mathrm{s}\,\rho_\mathrm{s} \int_{D_\mathrm{o}}^{\infty} \mathrm{e}^{\frac{-x}{\lambda_\mathrm{s,s}\ \cos\Theta}}\ \mathrm{d}x\ \ = I_\mathrm{s}^\infty \cdot \mathrm{e}^{\frac{-D_\mathrm{o}}{\lambda_\mathrm{s,o}\ \cos\Theta}} \tag{2.21}$$

$$I_\mathrm{o}^\infty = \sigma_\mathrm{o}\,\rho_\mathrm{o}\,\lambda_\mathrm{o,o}\ \cos\Theta \tag{2.22}$$

Here σ and ρ are the photoemission cross section and atomic density of the specific site, respectively. In the case of the overlayer the integration boundaries are chosen with reference to the overlay thickness. The thickness of the substrate is assumed to be very large in comparison to λ which simplifies the upper integration limit to infinity. Then, the whole signal from the substrate is exponentially damped by the overlayer with an inelastic mean free path of the photoelectrons from a substrate element in the overlayer material $\lambda_{s,o}$. The material dependent parameter I_o^∞ and I_s^∞ correspond to the absolute photoemission intensity of an infinite thick and clean sample made of the overlayer or substrate material, respectively. By means of the derived formulas for the intensity and for overlayer thicknesses in the range of λ the following statements can be formulated.

For grazing emission, $\Theta >> 0\,^\circ$:

- higher surface sensitivity is achieved,

- the signal coming from the overlayer is enhanced,

- the substrate signal originating from the interface is increased relative to the bulk signal.

For normal emission, $\Theta = 0\,^\circ$:

- higher bulk sensitivity is achieved,

- the signal of the substrate is enhanced,

- the overlayer signal originating from the interface is increased relative to the overlayer surface signal.

If the photon flux, analyzer efficiency and the change of X-ray spot size upon rotation of the sample are additionally taken into account, a comparison of absolute intensities is feasible. From an experimental point of view it is more common to compare relative intensities. Analytical solutions for the thickness determination are possible under the conditions that various inelastic mean free paths are almost equal. Then, as an example [42], the thickness D of a SiO_2 overlayer on top of a Si substrate is determined by the intensity ratio I_o/I_s in:

$$D = \lambda \cos\Theta \ln\left(\frac{I_o}{I_o^\infty} \frac{I_s^\infty}{I_s} + 1 \right) \,. \tag{2.23}$$

Critical reviews about quantitative depth profiling with angle resolved XPS can be found elsewhere [43–45]. An often discussed but crucial parameter is the *inelastic mean free path* (IMFP). Depending on the theoretical or experimental method the obtained values vary drastically. The formalism used in this work is elucidated in the next section. However, angle-resolved XPS is able to disentangle bulk, interface and surface signal.

2.1.5 Inelastic mean free path

The inelastic mean free path λ is an important parameter for quantitative statements, as demonstrated in the Beer-Lambert law (Eq. 2.15) and the previous section. Usually the IMFP is used to account for the exponential damping of the photoelectron intensity. It represents the average path length, which an electron travels between two successive inelastic interactions and can be calculated using the dielectric function for the valence band. However, the correct value for λ is the attenuation length, which is the projected distance of the IMFP along the direction to the detector [46]. The IMFP does not account for elastic scattering. This additional elastic scattering causes an elongation of the electron path due to its higher scattering probability compared to that of the inelastic scattering events. Therefore using the IMFP for depth profiling overestimates the attenuation length up to 30 % [46]. Additionally, interface and surface roughness can exhibit a large error to the degree of surface sensitivity.
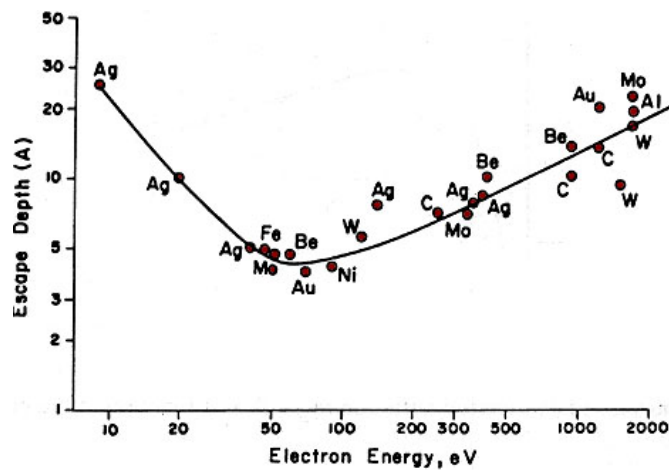
Figure 2.7: *Universal curve* of the inelastic mean free path of electrons in a solid and its dependence on the kinetic energy, from [47].

Commonly, the IMFP is considered to determine the sensitivity depth of the photoemission measurements and is also utilized in this work. In the case of soft X-rays it is in the range of several Å up to a few nanometer. In 1979, Seah and Dench [48] showed that the IMFP varies only marginal on the material but mostly on the kinetic energy of the photoelectrons as shown with the *universal curve* in Fig. 2.7. This empirical curve underlines the fact that the bulk contribution to the PES signal is enhanced by increasing the photon energy.

TPP-2M

The semi-empirical model by Tanuma, Powell and Penn (TPP-model) is a more accurate way to estimate the IMFP. In several articles [49, 50] they comment on the calculation of the IMFP using material dependent parameter, for instance the free-electron plasmon energy $E_{\mathrm{P}} = 28.8(\frac{\rho\,N_{\mathrm{V}}}{M})^{1/2}$, the number of valence electrons per unit cell N_{V}, the density ρ (in $\mathrm{g\,cm^{-3}}$), the molar weight M and the bandgap E_{g}. They propose that the kinetic energy E dependence of the IMFP can be approached by:

$$\lambda = \frac{E}{E_{\mathrm{P}}^2 \left[\beta \ln(\gamma E) - C/E + D/E^2\right]} \ . \tag{2.24}$$

The detailed formulas for β, γ, C and D as well as values for N_{V} can be found in [49]. Note that N_{V} is not the valency of the atoms but the number of valence electrons up to a certain binding energy, which take part in plasmon excitations, therefore the recommended values should be used.

2.2 X-ray absorption spectroscopy

On the basis of the derived one-particle dipole matrix element for the photoemission process in Eq. 2.13, XAS can be explained briefly. In contrast to photoemission, in which an electron has to be excited into continuum states above the vacuum level to escape from the surface, XAS measures excitations from occupied to unoccupied states close to the Fermi energy by the absorption of a photon. Basically, one determines the absorption coefficient $\mu(E)$ as a function of photon energy E close to the absorption edge that is defined by:

$$\frac{I(E)}{I_0} = \mathrm{e}^{\mu(E)d} \ , \tag{2.25}$$

with $I(E)/I_0$ being the relative light intensity transmitted through a sample with thickness d [51]. The absorption coefficient is proportional to the sum over all initial and final states given by Fermi's golden rule (Eq. 2.8):

$$\mu(E = h\nu) \sim \sum_{\mathrm{i,f}} \left| \langle \Psi_{\mathrm{f}} | \hat{\mathcal{H}}_{\mathrm{int}} | \Psi_{\mathrm{i}} \rangle \right|^2 \cdot \delta(E_{\mathrm{f}} - E_{\mathrm{i}} - h\nu) \ . \tag{2.26}$$

However, a direct measure of $\mu(E)$ by the light transmittance is impracticable. The absorption coefficient is instead determined indirectly by measuring the photocurrent caused by the emission of photoelectrons and Auger electrons. Auger electrons are generated when an electron refill the core hole of the photoexcited atom. Thereby, the

electron loses energy, which can be transferred to a second outer shell electron. The second electron will be emitted if the transferred energy is greater than its binding energy, shown in Fig. 2.11(c). While driving the photon energy across an absorption edge of a specific element in the sample, the energy matches those of a transition from an occupied to an unoccupied electronic state. By light absorption various core holes are generated at these photon energies, which generate many Auger electrons by the above mentioned Auger effect [52]. As a result, the sample current increases and is proportional to the absorption coefficient shown in Eq. 2.26.

The photocurrent of the sample can be determined either by measuring the sample current or by the detection of the emitted electrons. The former is called *total electron yield* (TEY) since all electrons, which are removed from the sample, increase the current irrespective of their kinetic energy. Especially, many low-energetic secondary electrons exist, which have a larger IMFP (see Fig. 2.7) and, therefore, increase the sensitivity depth up to $3 - 5$ nm [53, 54]. For the direct detection of the emitted electrons with for instance a channeltron detector the contribution of low-energy electrons can be removed by a retardation voltage. In this way, the depth sensitivity of the *partial electron yield* (PEY) absorption signal can be reduced compared to those of the TEY. For high retardation the PEY information depth approaches the photoemission IMFP.

Although the formula for the PES cross section and XAS signal looks quite similar, both methods are complementary to each other and in combination very powerful. Whereas PES depends mainly on the initial state, XAS measures the unoccupied *density of states* (DOS) of a local site. Also the experimental requirements for XAS are more sophisticated since a light source with tunable energies close to an absorption edge is needed and thus it is usually performed at synchrotron facilities. Another method, which uses a similar theoretical formalism is the *electron energy loss spectroscopy* (EELS).

2.2.1 One-electron picture

In order to understand the features, that are present in XAS, it is useful to start by neglecting any electron-electron correlations. In Fig. 2.8 the XAS intensity of a $3d$ band insulator is explained in such a one-electron picture. Since the dipole matrix element holds for dipole selection rules, only excitations from a $2p$ core level into an unoccupied $3d$ orbital have sufficient absorption cross sections. These are the commonly investigated excitations for $3d$ transition metals. Other possible excitations for the transition metals ($1s, 2s \rightarrow 4p$, $3p \rightarrow 3d$) are less informative since they give less intensive and broader features or do not probe the valence shell directly. In transition metal oxides, also investigations on the oxygen absorption edge are possible (O $1s \rightarrow$ O $2p$) but are not
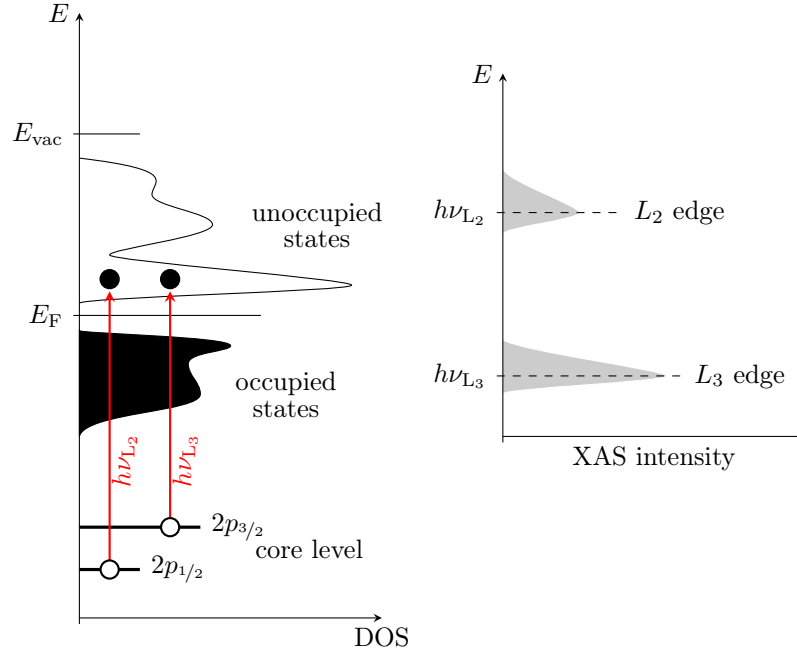
Figure 2.8: Scheme of photon induced electron excitation into an unoccupied state in a one-electron picture, from [55].

considered here. Note that the DOS of the transition metal $2p$ core level at deep energies is assumed by two delta functions, as shown in Fig. 2.8. The created photohole with spin $\frac{1}{2}$ interacts via spin-orbit coupling with its orbital momentum of 1. This results in a total angular momentum $j = \frac{1}{2}$ or $j = \frac{3}{2}$ with a degeneracy of 2 and 4, respectively. In the scheme other core levels are omitted for clarity. Historically, excitations from the $j = \frac{1}{2}$ state are called the L_2-edge and excitations from the $j = \frac{3}{2}$ state are called the L_3-edge. The latter is located at a lower photon energy $h\nu_{L_3}$ than the photon energy $h\nu_{L_2}$ of the L_2-edge. Their intensity ratio follows the degeneracy and the energy separation increases with climbing up the atomic number of the $3d$ metals (increased spin-orbit coupling).

2.2.2 Crystal field splitting

In the case of transition metal oxides the crystal field splitting caused by the surrounding oxygen atoms plays a major role determining the electronic ground state. In a perovskite structure the transition metal is located in the center of an oxygen octahedron, whose $2p$ orbitals are oriented towards the center. Due to their Coulomb potential and possible hybridization they lift the degeneracy of the unoccupied $3d$ states and therefore affect the absorption spectra. In such a symmetry it is reasonable to entitle the $3d$ orbitals according to Cartesian coordinates but not according to quantum numbers of spherical

harmonics, which are used in a free ion picture. As shown in Fig. 2.9, they are split into e_g and t_{2g} states in an octahedral crystal field (O_h symmetry). If additional distortions occur, the symmetry is further reduced and the degeneracy of these states is also lifted. This is shown exemplary for a tetragonal symmetry (D_{4h}), i.e. an elongation of the octahedron along z direction. The crystal field splitting of $3d$ orbitals in transition metal oxides is usually greater than their spin-orbit coupling strength and is thus able to elude *Hund's rules.*
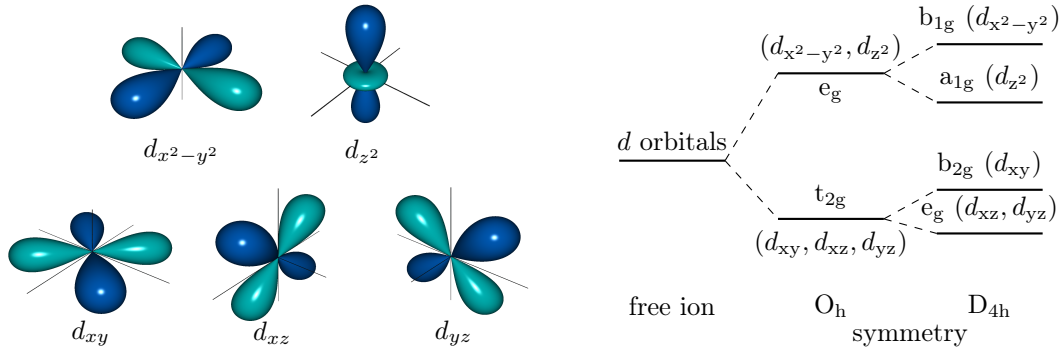

Figure 2.9: $3d$ orbitals of transition metals (left) and their splitting in an octahedral (O_h) and tetragonal (D_{4h}) crystal field (right).

The above mentioned assumptions are sufficient to explain the absorption spectra of Ti^{4+} ions surrounded by an oxygen octahedron. Calculations of the atomic multiplet in octahedral coordination are shown in Fig. 2.10. As a result of the spin-orbit coupling of the $2p$ hole, the atomic spectra consist of mainly two lines. In an octahedral crystal field the additional splitting of each component into e_g and t_{2g} peaks takes place. However, the one-electron picture is sufficient only for d^0 and d^9 configurations in the ground state.

2.2.3 Many-body effects

For an arbitrary d^n configuration the whole N-particle wave function has to be considered which increases the number of initial and especially final state configurations called multiplets. Additionally, electron-electron correlation, spin-spin and spin-orbit coupling become crucial for the energy of each multiplet. For instance the Coulomb repulsion for a $3d_{z^2}$ and a $2p_z$ orbital is larger than between a $3d_{x^2-y^2}$ and a $2p_z$ orbital, which can be understood by looking at the overlap integral of these orbitals. Fortunately, the excitations into many of these multiplets are forbidden by the dipole selection rules of the matrix element. Therefore, sharp features in L-edge spectra are still visible although these multiplets can be spread out over wide energy ranges. Furthermore, the selection

rules are the main reason that XAS is very sensitive to changes in the ground state, for instance changes in valency, orbital occupation or spin state.
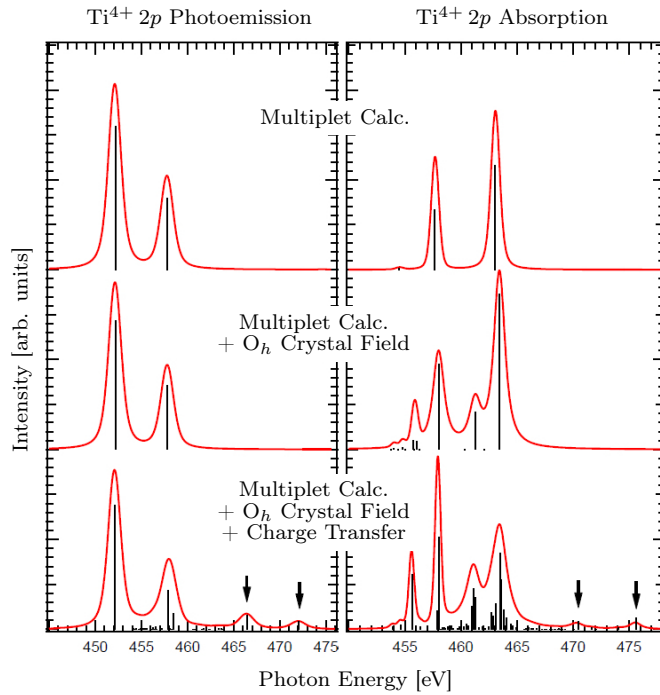
Figure 2.10: Multiplet calculations of Ti^{4+} XPS and XAS spectra in spherical and octahedral symmetry including charge transfer, from [56].

At this point, also the possible charge transfer has to be mentioned. Attracted by the hole in the excited state and because of the hybridization to neighboring atoms, it is possible that an additional electron is transferred from the ligand (oxygen in the case of transition metal oxides) into a $3d$ orbital of the excited atom. Depending on the material system such final states have either higher or lower energy compared to the excitation without charge transfer. Hence, in PES and XAS new features appear, which are usually referred to $3d^{n+1}\underline{L}$. Here $\underline{L}$ denotes a hole on the ligand (oxygen $2p$ band). Fig. 2.10 is a summary of the discussed effects based on multiplet calculations for the photoemission and absorption signal of a Ti^{4+} ion. Due to the initial d^0 configuration spin-spin interactions are almost absent, leading to very similar PES and XAS spectra. Predominantly, the XAS signal is affected by the octahedral crystal field, which changes mainly the energy of the unoccupied states. If additional charge transfer effects are included, both spectra change even more.

In conclusion, XAS is a very powerful type of spectroscopy that delivers a huge amount of informations on the ground state and crucial physical parameters driving the electronic

properties. The XAS excitation process is strongly excitonic-like because of the large $2p$ core hole - $3d$ electron attraction. Many effects that may alter the spectra drastically were mentioned above. The absorption process is very local which enables the simulation by atomic multiplet theory. Incidentally, the work by Thole [41] as well as the "XTLS" program of Tanaka [57] should be mentioned. In this thesis the program CTM4XAS (*charge transfer multiplet for XAS*) that is based on the "Cowan"-code by Thole and Cowan has been used. The CTM4XAS front end was/is developed by the group of de Groot [41, 58, 59] who compares calculations with experimental data comprehensively. This section should be treated as a starting point for the interpretation of XAS and *X-ray linear dichroism* (XLD) spectra. A detailed description can be found in the given literature and the references within.

2.3 Resonant photoemission spectroscopy

Resonant photoemission spectroscopy (ResPES) can be seen as a combination of both types of X-ray spectroscopy described above. The valence band spectra are taken by changing the photon energy across an absorption edge. The following Fig. 2.11, according to [60], illustrates not only the principle of ResPES but also summarizes valence band PES (a), core level PES (b), XAS (d) and for the sake of completeness Auger spectroscopy (c).

In a ResPES experiment the normal valence band photoemission can interfere coherently with the different final states depicted in (a) and (e)/(f) of Fig. 2.11. If the photon energy is set across an absorption edge of a certain element in the specimen, an excitation of a core electron into the unoccupied orbitals can occur (d). Then the system is in an intermediate excited state with a core hole and an additional electron in the conduction band. For de-excitation an autoionization or Auger effects happen, in which the core hole is filled by an outer shell electron and the residual energy is released in terms of Auger electrons. This results in greatly enhanced or suppressed spectral weight of the specific atomic species in the valence band. If the excited electron in the previous empty state of the conduction band is emitted, the process is called *participator decay*. In Fig. 2.11 it is shown that the final state of the latter described process (e) is exactly the same as that of a normal valence band photoemission (a) and yields equal kinetic energy for the emitted electron. To calculate the photoemission intensity for this situation the cross section of both processes have to be summed up coherently since the participator decay
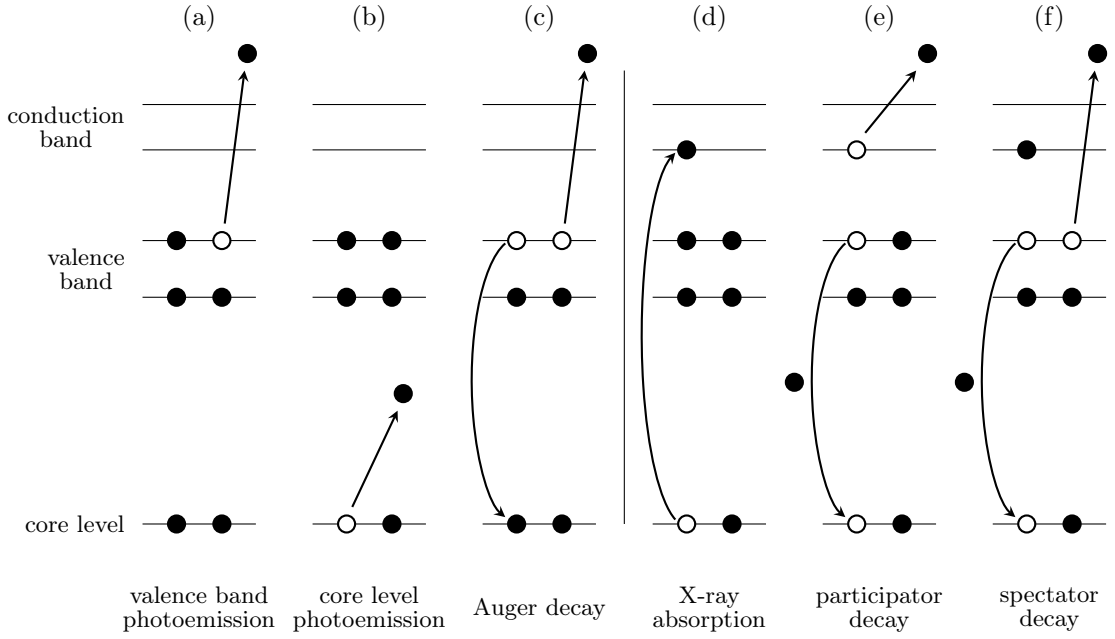
Figure 2.11: Scheme of the different excitation and de-excitation channels during XPS, XAS and ResPES experiments, according to [60].

that contains an intermediate state $|\Psi_j\rangle$ happens at very low time scales. This leads to interference effects for the photoemission probability and can be expressed by:

$$
w_{i \to f} \sim \left| \left\langle \Psi_f | \hat{\mathcal{V}}_r | \Psi_i \right\rangle + \sum_j \frac{\left\langle \Psi_f | \hat{\mathcal{V}}_A | \Psi_j \right\rangle \left\langle \Psi_j | \hat{\mathcal{V}}_r | \Psi_i \right\rangle}{E_g - E_j + i\Gamma_j/2} \right|^2 \delta(E_f - E_i) .
\tag{2.27}
$$

Here, $\hat{\mathcal{V}}_r$ and $\hat{\mathcal{V}}_A$ denote the radiative dipole ($\hat{\mathcal{H}}_{int}$) and Coulomb operator, respectively. Γ_j is the core-level lifetime-induced width of the intermediate state $|\Psi_j\rangle$ [60].

In contrast to this, the first excited electron remains in its state during the *spectator decay*. Here, an electron from the valence band is emitted when the initially core hole is refilled. As it can be seen in Fig. 2.11(f) the system remains in a state, in which two electrons from the valence band are missing, equivalent to Auger decay (c) but with one additional electron located in the conduction band. The spectral weight, arisen by Auger and spectator decays, is therefore similar in shape. Important to distinguish between participator and spectator decay is the fact that the features in the valence band, caused by the latter, shift in binding energy for scanning the photon energy across the absorption edge, whereas they stay constant for the participator decay. Furthermore, intensity resonances can only be seen for the participator decay.

2.4 Experimental setup

2.4.1 Synchrotron facility
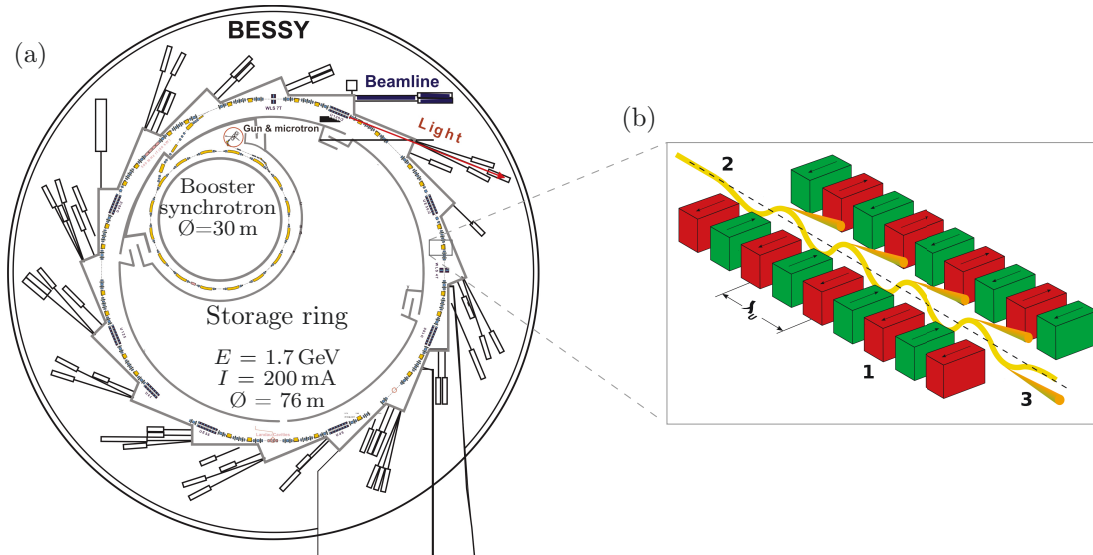
Figure 2.12: Scheme of the BESSY II synchrotron facility (a). The electrons are accelerated up to about 1.7 GeV by the "Booster" and then injected into the storage ring. The undulator (b), an arrangement of magnets, bend the electron beam periodically and generates tangential electromagnetic radiation. The radiation is then monochromatized and guided via beamlines to the experiment.

XAS and ResPES experiments require a high quality light source with tunable photon energy, variable polarization, high energy resolution, high intensity, small spot size and high stability of the beam. The brilliance is an important parameter to characterize and compare X-ray sources. It takes the number of photons per second, their angular divergence, their energetic bandwidth and the spot size into account. Especially, synchrotron light sources provide X-rays with tunable photon energy and high brilliance, many orders of magnitude higher than conventional X-ray tubes. Here, the electromagnetic radiation is emitted when charged particles (electrons, positrons, protons) with high kinetic energies are accelerated radially, i.e. perpendicular to their direction of movement. For this purpose particles are accelerated usually in a linear accelerator or in a small synchrotron to energies of several giga-eV. Afterwards, they are injected into the storage ring, which achieves a lifetime of several hours by compensating radiative energy loses. Either bending magnets (dipoles), which keep the particles in the closed orbit, or insertion devices, such as wigglers or undulators situated in the straight sections, create the synchrotron radiation within the storage ring [61]. By changing the arrangement of the undulator magnets the polarization can be changed to vertical, horizontal or left and right circular

polarized light. Mirrors in the beamline are used to guide, monochromatize and focus the tangential emitted light on the sample located in the analyzing chamber. For the whole experiment *ultra-high vacuum* (UHV) conditions are necessary from generating the electrons, via their acceleration through to the irradiation of the specimen.
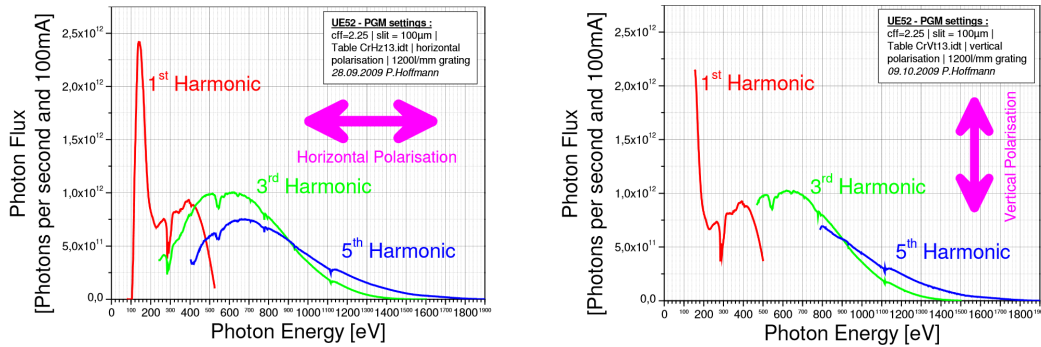

Figure 2.13: Photon flux of the UE52-PGM beamline for horizontal (left) and vertical (rigth) polarized light measured with a GaAs diode and an exit slit of 100 μm.

The data of the present work have been acquired at the *Berliner Elektronenspeicherring-Gesellschaft für Synchrotronstrahlung* (BESSY II) at the UE52-PGM beamline, that is equipped with a plane grating monochromator. In Fig. 2.12 a scheme of the BESSY II synchrotron and an undulator is shown. The photon flux and energy bandwidth depend on the chosen photon energy, polarization, exit slit and the used harmonics of the undulator. For standard operation the photon flux depending on photon energy is shown for horizontal and vertical polarization in Fig. 2.13. The end-station is equipped with a Scienta R4000 hemispherical electron analyzer, a channeltron, that can be used as an PEY detector, and a photo diode for measuring partial electron and/or total fluorescence yield. In combination with a manipulator, that enables the detection of the photocurrent, i.e. TEY, the apparatus is designated for high resolution XPS and XAS studies. In addition, due to the available dispersive mode fast ResPES measurements are possible. The preparation chamber is equipped with a Al K_α X-ray source, a LEED (*low energy electron diffraction*), a mass spectrometer and a sputter gun, all of them are necessary for cleaning, preparing and preinvestigating the sample.

2.4.2 Laboratory spectrometer

Nearly all laboratory XPS investigations of this work were done at the IFW Dresden with a spectrometer system constructed by the company *SPECS*. The experiments were carried out under UHV conditions with a base pressure of $p = 2 \cdot 10^{-10}$ mbar. A sketch with all components of the spectrometer system can be seen in Fig. 2.14.
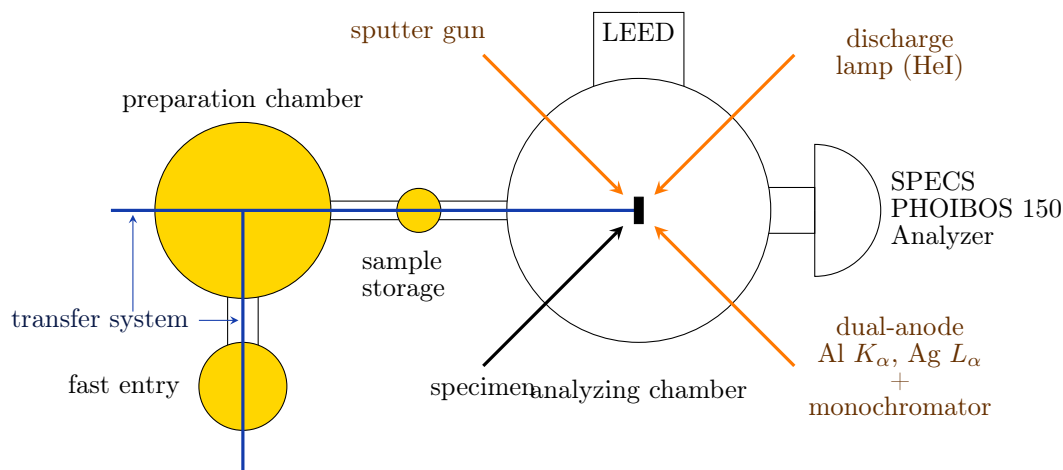
Figure 2.14: Schematic layout of the laboratory spectrometer system.

The sample holder can be introduced into the system via the fast entry. It is possible to heat the sample up to $1000\,°C$ with an integrated electron beam heater in the preparation chamber. A VAT vacuum valve separates the preparation from the analyzing chamber, which can be reached by a transfer system. Different characterization tools are on hand in the analyzing chamber, including a LEED and hemispherical electron analyzer (PHOI-BOS 150) manufactured by *SPECS* company. A monochromatized, dual anode X-ray source XR-50 M (Al K_α 1486.6 eV, Ag L_α 2984.3 eV) and a helium discharge lamp (*UVS 300*) are the available light sources. Additionally, the sample can be cleaned with a sputter gun (*SPECS IQ 12/38*) via the bombardment with noble gas ions (Ar$^+$). The energy resolution at room temperature is about 0.3 eV for XPS and 0.1 eV for UPS.

3 Insulator-metal phase transition at polar/non-polar oxide interfaces

3.1 Introduction

The main task of this thesis is the investigation of functional interfaces between perovskite oxides. Perovskites entitle all ABO_3 cubic crystal structures (space group $Pm\bar{3}m$), which consist of twelve-fold coordinated cations at the A-site and six-fold coordinated cations at the B-site, surrounded by an oxygen octahedron (shown in Fig. 3.1(a)). Orthorhombic distortions or tilting of the oxygen octahedron are characteristic for this chemical family. There are only little restrictions concerning the A and B-site ions, for instance their overall oxidation state has to be six (valency of A + B = 6). Thus a large variety of cation combinations exists, and many of these compounds have complex phase diagrams and show considerable variety of physical properties and exotic phenomena [62, 63], e.g.:

- ferroelectric ceramics with high dielectric constant ($BaTiO_3$) [64],

- large magnetoresistance in manganites (La, Sr)MnO_3 [3],

- ferromagnetism and large spin polarization above room temperature [65],

- high temperature superconductivity in cuprates (e.g. $YBa_2Cu_3O_7$ [5]).

The main reason for the observed properties is the occupancy of the transition metal $3d$ orbitals and hence, the subtle interplay between strong electron-electron correlations at atomic sites and their hybridization with oxygen p electrons. The Coulomb repulsion keeps the $3d$ electrons more localized, while the hybridization causes delocalization/itinerancy [66, 67]. In recent years, the epitaxial growth of perovskite oxide films with very high quality, shown in Fig. 3.2, became possible by *reflection high-energy electron diffraction* (RHEED) assisted *chemical vapor deposition* (CVD), *pulsed laser deposition* (PLD) or *molecular beam epitaxy* (MBE), introducing the interface as an additional degree of freedom. A tremendous amount of different oxide heterostructures or superlattices seem to be manufacturable. These exhibit an even more complex situation at the interface leading to new physical properties. Not only the break in translational
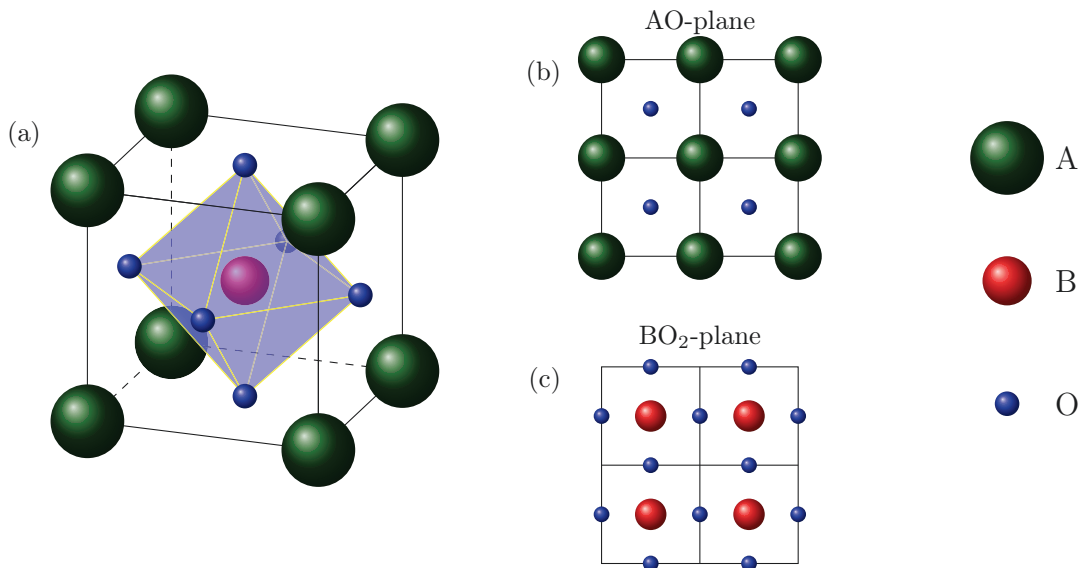
Figure 3.1: Side view on the cubic crystal structure of the ABO_3-perovskite family (a), top view on the AO-plane and (b) on the BO_2-plane (c).

symmetry but also strain induced structural distortions, point defects, dislocations and stacking faults can alter the electronic system.

One famous example is the interface between lanthanum aluminate ($LaAlO_3$) and strontium titanate ($SrTiO_3$), briefly called LAO and STO. In a simple ionic picture the valencies for each site are: Sr^{2+}, La^{3+}, Ti^{4+}, Al^{3+} and of course O^{2-}. Both perovskites are non-magnetic wide bandgap insulators with a closed electronic shell, $4f^0$ for LAO and $3d^0$ for STO. In 2004, Ohtomo and Hwang reported about a high-mobility electron gas, which is surprisingly formed at the interface between these two insulating perovskite oxides [10]. The presence of Shubnikov-de Haas oscillations, whose period depends only on the perpendicular component of the magnetic field [69], is a prove for its two-dimensional nature, and therefore it is often called a *two-dimensional electron gas* (2DEG) or even a two-dimensional electron liquid, since electron-electron interactions have to be taken into account. In the following, besides the electric conductivity also superconductivity [70, 71], ferromagnetism [72, 73], large in-plane magnetoresistance [19, 74, 75] and giant persistent photoconductivity [21, 76] were found at this interface.

The interface conductivity occurs only for LAO films grown on TiO_2-terminated STO substrates, but not for films grown on SrO-terminated STO. The transport properties for LAO/STO heterostructures determined by Hall measurements have been controversially discussed in literature. High mobilities up to $10\,000\,cm^2(Vs)^{-1}$ have been reached for samples grown under low oxygen partial pressure [10]. However, samples grown under higher oxygen pressures reveal much lower mobilities. Furthermore, the transport prop-
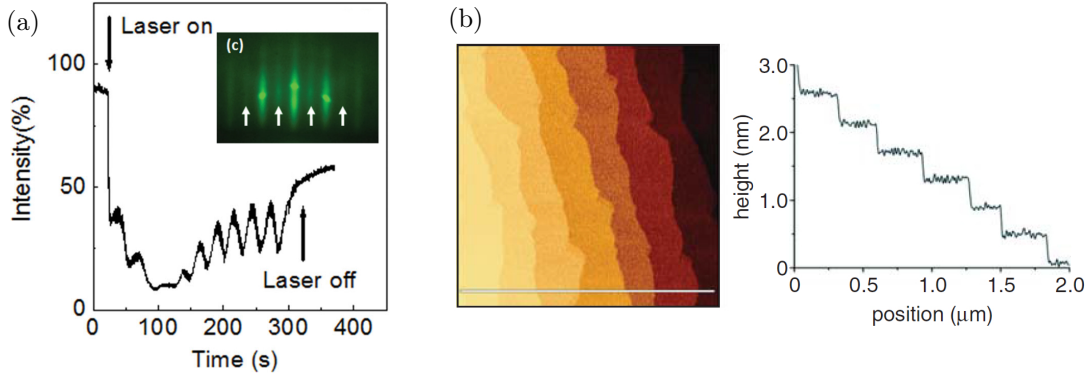
Figure 3.2: During the growth of oxides, structures in the RHEED-pattern (c) and their intensity oscillations (a) indicate a epitaxial layer-by-layer growth. The data are taken from [21] and show the RHEED pattern/oscillations for a NGO film grown on STO ($T = 700\,°C$, $p(O_2) = 5 \cdot 10^{-2}$ mbar). Atomic force microscopy image of a 26 uc LAO film grown on TiO_2-terminated STO (b), from Ref. [68]. A sign of high quality are the reproduced terraces from the substrate with one unit cell step height.

erties are affected by electric fields [77], which enables their application in field effect devices. Superconductivity in LAO/STO with a critical temperature of ~ 200 mK and with signs of two dimensionality was observed by Reyren *et al.* [70, 71]. Hysteresis in the magnetoresistance at low temperatures [19], SQUID measurements [72, 73] and torque magnetometry measurements [78] indicate the existence of ferromagnetism. The coexistence of ferromagnetism and superconductivity in the same sample [72] raises further scientific interest. By scanning SQUID experiments Bert *et al.* imaged sub-micrometer ferromagnetic domains incorporated in a rather uniform paramagnetic background, which becomes diamagnetic and superconducting at low temperatures. The transport properties of LAO/STO and other oxide heterostructures appeared to be strongly influenced by light irradiation, for instance a large decrease in resistivity under UV-light (by a factor of ~ 2) was reported, which persists for several hours after light illumination [21, 79].

The physical mechanisms, that drive all these exciting properties, are still a subject of passionate debates. The four itemized hypotheses can cause an effective doping of the interface region and will be explained in the following [68]:

- "polar catastrophe" scenario,

- oxygen vacancies,

- structural distortions,

- cation intermixing.

"Polar catastrophe" scenario

In Fig. 3.3 it is illustrated, how an electronic reconstruction is able to avoid a polar catastrophe and leads to conductivity at the interface [11]. It can be understood within an ionic limit, as mentioned before, whereby STO along (001)-direction consists of neutrally charged $Sr^{2+}O^{2-}$ and $Ti^{4+}O^{2-}_2$ planes, while the $La^{3+}O^{2-}$ and $Al^{3+}O^{2-}_2$ layers in LAO are charged alternating $+1$ and -1. The 2D unit cells of these AO- and BO_2-planes can be seen in Fig. 3.1(b) and (c). Obviously, an electrostatic potential V builds up with increasing layer number. Fig. 3.3(b) illustrates how the system undergoes an electronic reconstruction to avoid an unphysical diverging potential. This is only possible due to the variable valency of the Ti-ion, whose oxidation state is known to vary between $+2$ and $+4$ in nature. In this way, half an electron per 2D unit cell is transferred from the surface of the LAO to the topmost TiO_2 layer of STO and changes the occupancy of the Ti $3d$ levels from the generic $3d^0$ (Ti^{4+}) to a $3d^{0.5}$ ($Ti^{3.5+}$) state. The additional correlated electrons at the interface can lead to the intriguing properties of the 2DEG. This scenario rests on the build-in potential discontinuity at polar/non-polar heterostructures and is therefore referred to as an intrinsic mechanism. It predicts a critical thickness of LAO as onset for conductivity, which, indeed, was found by Thiel *et al.* and is shown in Fig. 3.4 [77]. In fact, strong overlayer thickness dependences were reported for nearly all 2DEG-properties.
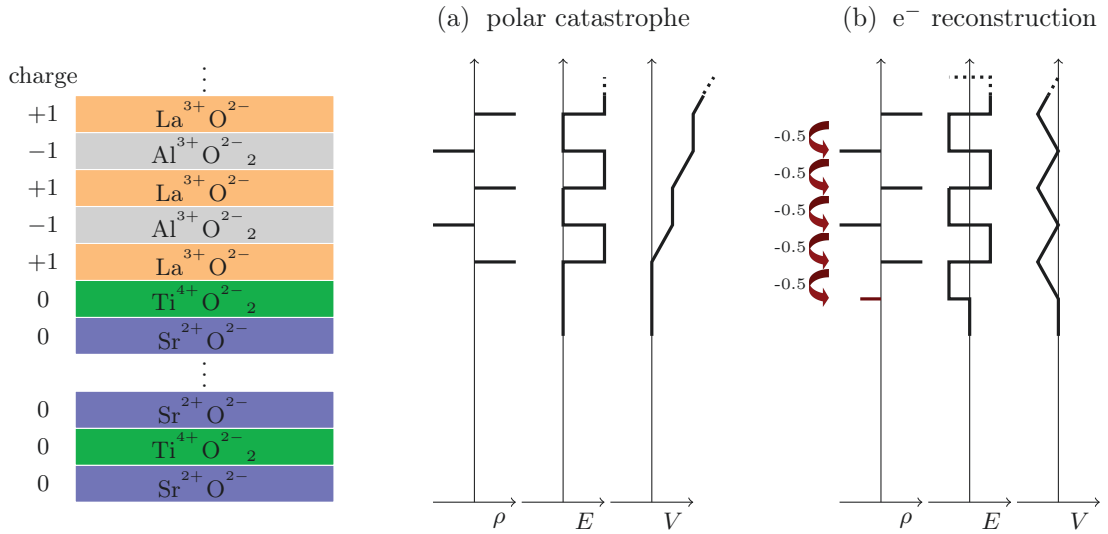
Figure 3.3: Schematic illustration of the polar/non-polar oxide interface and the behavior of physical parameters (effective charge density ρ, electric field E, electrostatic potential V) in the case of (a) the polar catastrophe scenario and (b) after electronic reconstruction.

Despite of the advantages mentioned above, the "polar catastrophe" scenario reveals also discrepancies with experiments. For instance, interfacial conductivity occurs also when amorphous LAO films, which have no preferential polarization direction, are grown on STO. But it turned out that oxygen vacancies play a major role here, since the conductivity does not persist upon oxygen treatment [80]. Furthermore, *photoemission spectroscopy* (PES) is not able to detect strong polar fields in the LAO overlayer material, which should cause an energy shift of all related states [81–84]. The 2DEG at the interface with a robust critical thickness is only formed if LAO is deposited on TiO_2-terminated STO but not for the reversed SrO-AlO_2 interface structure [10, 68]. Similar behavior as for LAO/STO was found for other polar overlayer materials but not for other non-polar substrates than STO. Density functional theory [85–89] and dynamical mean field theory calculations [90–92] confirm on the one hand the intuitive picture of the rising electrostatic potential and show how the electron density accumulates at such oxide interfaces, but on the other hand they also predict that structural deformations, charge, orbital and/or magnetic ordering as well as the formation of oxygen vacancies play a crucial role [93].
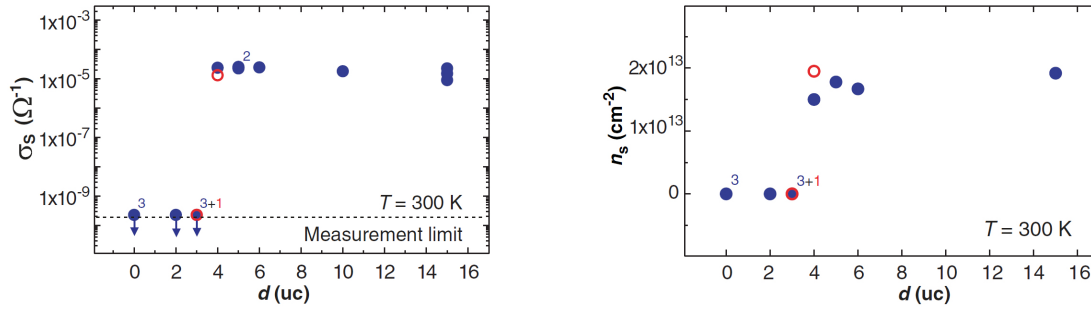

Figure 3.4: Sheet conductance and sheet carrier density of LAO/STO interfaces depending on LAO thickness d, taken from [77]. The LAO layers were grown on TiO_2-terminated STO by RHEED assisted PLD in an oxygen atmosphere of $2 \cdot 10^{-5}$ mbar and a substrate temperature of $770 - 815°C$. Afterwards, they were cooled to room temperature in 400 mbar oxygen partial pressure. An insulator-metal phase transition occurs at a critical thickness of 4 uc.

Oxygen vacancies

It is well known that the wide bandgap insulator STO can be easily doped n-type or p-type. Commonly, n-type conductance is achieved by the substitution of Sr^{2+} by La^{3+}, of Ti^{4+} by Nb^{5+} or by reduction, whereby every oxygen vacancy releases two electrons. Oxygen vacancies, acting as electron donors, tend to get mobile at ordinary PLD growth conditions with substrate temperatures of about $T = 750 - 850°C$ [68]. Oxygen poor STO exhibits superconductivity with transition temperatures of $300 - 400$ mK and

unexpected high low-temperature mobilities up to $30\,000\,\mathrm{cm}^2\mathrm{V}^{-1}\mathrm{s}^{-1}$, that scatter over wide ranges depending on reference [94]. The similarities to the LAO/STO interface, which properties vary strongly on the oxygen partial pressure during growth [95], are obvious. As it is shown in Fig. 3.5, samples grown under high oxygen partial pressure show magnetism. Low oxygen pressure leads to the formation of oxygen vacancies, while superconductivity is found in the intermediate regime [96]. However, *conducting tip atomic force microscope* (C-AFM) measurements reveal a confinement of conductivity towards the interface region ($< 7\,\mathrm{nm}$) only for well oxidized samples. Otherwise, the conducting part penetrates several micrometers into the STO bulk. To suppress this extrinsic effect of oxygen vacancies a post-growth oxygen treatment is usually performed by cooling down the samples over several hours in $0.3 - 1\,\mathrm{bar}$ oxygen partial pressure. Nonetheless, an accumulation of oxygen vacancies at the interface, probably induced by distortions or by the polar character, cannot be ruled out. An indication that oxygen vacancies do not dominate the physical mechanisms at the interface is the absence of the carrier "freeze-out effect" at low temperatures [97], that would be observed for carriers from thermally activated donor levels of oxygen vacancies [94, 98]. In the case of an electronic reconstruction the degenerated $3d$ levels get filled with additional electrons, which do not need to get activated to take part in transport.
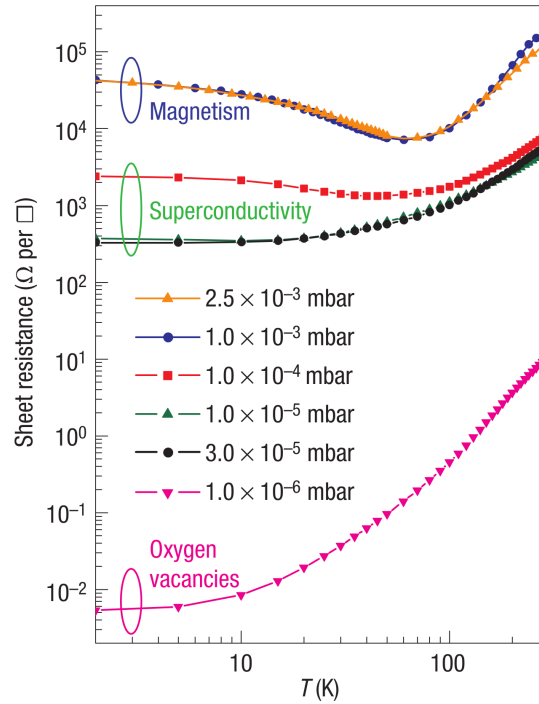
Figure 3.5: Temperature dependence of the sheet resistance for LAO/STO conducting interfaces, grown at various partial oxygen pressures, taken from [68].

Structural distortions and cation intermixing

Structural distortions and cation intermixing across the interface are two alternative mechanisms, which may contribute to the fascinating physics of polar/non-polar interfaces. Finite intermixing and deviations from an abrupt interface were found for the A-site (La $\leftrightarrow$ Sr) and B-site sublattice (Al $\leftrightarrow$ Ti) [14, 99–101], e.g. by *X-ray diffraction* (XRD) [13], medium energy ion scattering [102] and photoemission spectroscopy [103, 104], indicating a much more complex nature of the 2DEG. Recent scanning transmission electron microscopy and electron energy loss spectroscopy (STEM/EELS) data, performed on samples similar to the ones employed in this work, have posed nevertheless stringent upper limits to the amount of La cations crossing the interface [105]. The experimental Ti and La elemental profiles across the interface, shown in Fig. 3.6, deviate only marginally from simulated profiles. Also distortions, buckling or rotations of the TiO_6 octahedron, induced by the strain at the interface, can change the Ti $3d$ bandwidth or can split their degeneracy. This may favor the occupation of a certain Ti $3d$ orbital which can lead to conductivity [15, 106, 107].

Atomic rearrangements, defects and interface roughness are widely recognized as possible mechanisms to decrease or to eliminate polar discontinuities and interface dipoles at ordinary group II, III, IV and V semiconductor heterostructures [108]. Furthermore, atomic intermixing can effectively dope the interface region. However, it seems questionable that these effects alone can provide the entire free carrier density at the interface and can cause the large variety of properties. In particular the variable valency of Ti in STO based oxide heterostructures, seems to be a prerequisite to eliminate a "polar catastrophe" and opens new fundamentals for the engineering of functional electronic interfaces.

3.2 Samples

There are different ways to gain more insights into the mechanisms which drive the physical properties at polar/non-polar oxide interfaces. They range from first principle calculations via the growth and characterization of interfaces, made by other materials, up to their detailed experimental investigation with various techniques. For example electron-electron correlations [92] or certain defect structures and distortions can be taken into account in theoretical calculations, the band insulator LAO can be substituted by other polar oxides including also Mott insulators (e.g. $LaTiO_3$ [87, 109], $LaVO_3$ [110]), and for instance high resolution X-ray reflectometry or X-ray standing wave spectroscopy can be performed. In this work the properties of three different materials, namely lanthanum
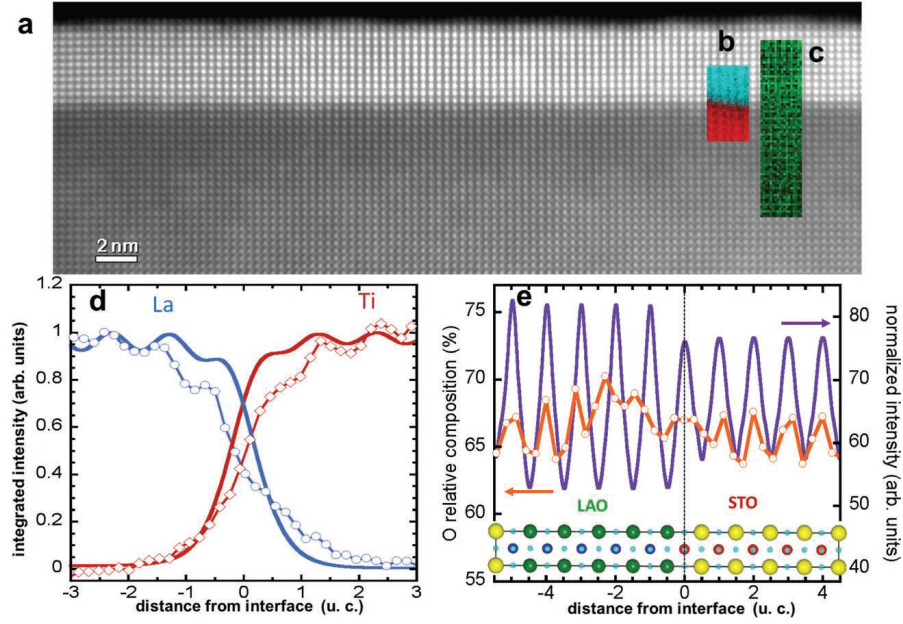
Figure 3.6: High structural and chemical quality of the LAO/STO heterostructures inves-
tigated in this thesis has been proven by high angle annular dark field micrograph (a) and
superimposed *electron energy loss spectroscopy* (EELS) Ti and La elemental map (b) and O
map (c). (d) Experimental La $M_{4,5}$ and Ti $L_{2,3}$ EELS profiles (open symbols) are compared
to simulated profiles (solid lines) for an atomically abrupt interface. (e) Experimental (line
+ symbols) and simulated (solid line) O K-edge profiles: Both data express two slightly dif-
ferent quantities, thus their different amplitude does not indicate different oxygen content.
Taken from [105].

aluminate LaAlO$_3$ (LAO), lanthanum gallate LaGaO$_3$ (LGO) [111–114] and neodymium
gallate NdGaO$_3$ (NGO) [21, 79, 115], all grown on STO in (001)-direction, are inves-
tigated in detail by X-ray spectroscopy techniques. The interfaces of these three polar
compounds with STO share some properties considered to be crucial for the electronic
reconstruction scenario. LGO and NGO also consist of alternating positively charged
AO-planes and negatively charged BO$_2$-planes and therefore, grown on STO, they ex-
hibit a polar/non-polar interface characteristic. Both compounds have a larger bandgap,
3.8 eV for NGO and 4.4 eV for LGO, than STO (3.2 eV), which however are smaller than
the 5.6 eV bandgap of LAO. The larger bandgap was proposed to be necessary to align
the conduction band of the polar film energetically above the conduction band of STO.
Only in this case, electrons can be transferred from the surface valence band primarily
into the conduction band of the interfacial TiO$_2$ layer of STO. Finally, strong similarities
with LAO/STO interfaces were found, i.e. an insulator to metal phase transition with a
critical thickness of about 4 *unit cells* (uc), similar transport properties strongly depend-
ing on oxygen partial pressure during growth, superconductivity with $T_c \sim 200-300$ mK,
persistent photoconductivity [21, 111, 115]. In this manner, the effect of the lattice mis-

Table 3.1: Properties of the four investigated perovskite oxides, i.e. chemical formula, valency in an ionic limit, polarity of the layers in (001)-direction, bandgap [116–120], lattice constant [121–123] and mismatch towards the STO substrate, as well as superconducting T_c of bulk STO (doped) [124] and reported T_c for the 2DEG at the three interfaces to STO [70, 71, 111, 125].

name	strontium titanate	lanthanum aluminate	lanthanum gallate	neodymium gallate
chem. formula	$SrTiO_3$	$LaAlO_3$	$LaGaO_3$	$NdGaO_3$
ionic limit	$Sr^{2+}Ti^{4+}O_3^{2-}$	$La^{3+}Al^{3+}O_3^{2-}$	$La^{3+}Ga^{3+}O_3^{2-}$	$Nd^{3+}Ga^{3+}O_3^{2-}$
(100) layers	non-polar	polar (+1,−1)	polar (+1,−1)	polar (+1,−1)
bandgap	3.2 eV	5.6 eV	4.4 eV	3.8 eV
lattice constant	3.905 Å	3.79 Å	3.896 Å	3.864 Å
lattice mismatch	-	-2.94 %	-0.23 %	-1.04 %
n_{critical} for 2DEG	-	4 uc	4 uc	4 uc
superconducting T_c	350 mK	200 mK	150 mK	200 mK

match can be analyzed. The substitution of aluminum by gallium on the B cationic site results in an increase of the pseudocubic lattice constant. Contrary, neodymium has a smaller ionic radius than lanthanum. This yields to a smaller lattice constant for NGO than LGO but an even larger than for LAO, which implies that the smallest lattice mismatch compared to STO is achieved with LGO. A small lattice mismatch is a prerequisite for high quality epitaxial growth. An increase in lattice mismatch can be the origin for a higher degree of disorder and structural distortions. Secondly, the effect of different chemical environments for the Ti-sites can be investigated. Important parameters of STO, LAO, NGO and LGO are summarized in Tab. 3.1.

Most of the transition metal oxide thin films, studied in this thesis, were fabricated by RHEED assisted pulsed laser deposition in the MODA lab (Modular facility for Oxides Deposition and Analysis) at the CNR-SPIN institute, Naples, Italy. A sketch of the growth chamber is shown in Fig. 3.7. Within this type of *physical vapor deposition* (PVD) the light of a high-power pulsed KrF excimer laser (wavelength 248 nm, repetition rate $\sim$ 0.5 Hz) is focused on a stoichiometric target inside a vacuum chamber, which is vaporized due to the introduced energy of about 1.5 $^{J}/_{cm^{-2}}$ per laser pulse. The ions in the created plasma plume are deposited as a thin film on the heated substrate located at about 40 mm in front of the target. An optimized substrate temperature (about 730 °C) and oxygen partial pressure in the vacuum chamber are essential to achieve epitaxial layer

by layer growth of a well oxidized film, which yields reproducible metallic interfaces with above mentioned properties [21]. Single TiO_2-terminated STO substrates were purchased from TSST BV. During the growth, the structure, the morphology and the roughness can be analyzed *in situ* by the RHEED pattern. In addition, the intensity variation/oscillation of the RHEED pattern is a measure for the thickness of the film with sub-monolayer sensitivity [126]. A relatively high oxygen partial pressure of about 10^{-2} mbar was adopted in order to decrease the risk of incorporating oxygen vacancies into STO during the growth process. This method has proved to produce high quality samples if proper growth conditions are adopted [21, 112, 114, 127]. A slow cooling down to room temperature was performed after growth by keeping the oxygen pressure unchanged. The high quality of a LAO/STO sample grown in the same laboratory under similar condition has been proven with TEM/EELS measurements by Cantoni *et al.* [105], shown in Fig. 3.6.

The samples were transported in air and cleaned by rinsing them in acetone prior the experiment. They were glued on the sample holder by conducting silver paint to avoid charging effects. Nevertheless, finite charging were observed for samples with a thickness below the conductivity threshold. The thickness of the investigated samples is limited by the sensitivity depth of the experimental technique. As a result of the small inelastic mean free path of photoelectrons, only samples with an overlayer thickness up to 8 uc can be investigated.
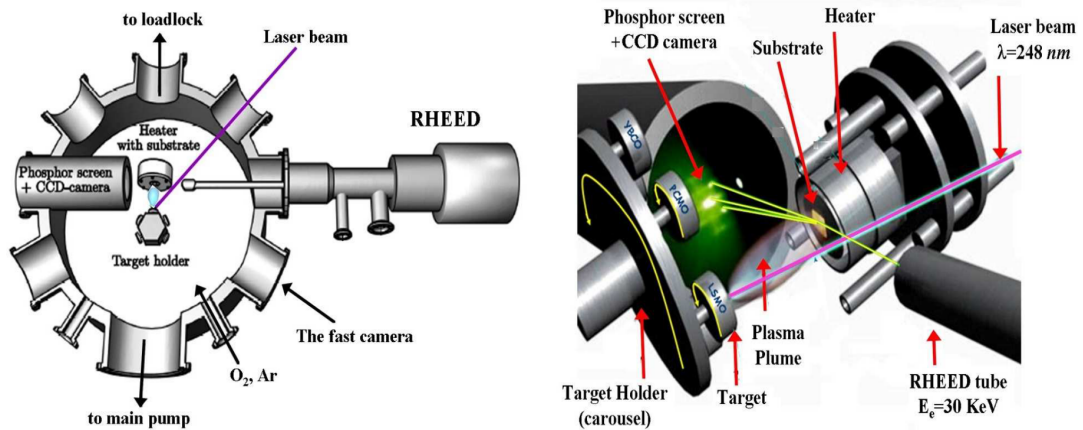
Figure 3.7: Sketch of the MODA PLD growth chamber and a close view on all important parts during the PLD process, taken from [127].

3.3 Strontium segregation at polar/non-polar oxide interfaces

The following section is related to the growth and the stoichiometric structure of the samples. The cation core levels of all samples were investigated by detailed *X-ray photoemission spectroscopy* (XPS) measurements. To disentangle bulk, interface and surface signal the sensitivity depth was tuned by varying the *photon energy* ($h\nu$) and the *emission angle* (Θ) (see section 2.1.4). It is shown that an unexpected second strontium component, that can be attribute to surface segregation of Sr cations, clearly emerges from the collected spectra. Such phenomena are found in perovskites like $La_xSr_{1-x}MnO_3$ [2], $SrTiO_3$ [128], $SrTi_{1-x}Fe_xO_{3-\delta}$ [129] and in the $TiO_2/SrTiO_3$ system [130, 131] frequently, especially when the grown compound is composed of strontium itself. Also the role of Sr-vacancies at the LAO/STO interface is under discussion [132]. The Sr segregation effect occurs for all heterostructures and film thicknesses addressed in this work.

Fig. 3.8 shows the background corrected and normalized Sr $3d$ core levels for pure STO (a) and 3 uc LAO/STO (b) measured with varying photon energy and emission angle. The Sr $3d$ line consists of a doublet due to spin-orbit splitting (Sr $3d_{3/2}$, Sr $3d_{5/2}$). Charging-related energy shifts have been encountered during the measurements. Therefore, I am going to refer to the binding energy shifts with respect to the Sr $3d_{5/2}$ peak maximum, rather than to absolute binding energy values. The surface sensitivity of the experiment can be tuned by changing the photon energy and the emission angle. Lower photon energies and higher emission angles increase the surface contribution to the overall signal and decrease the effective IMFP λ_{eff} – the projection of the IMFP λ to the surface normal (see Fig. 2.6 and Eq. 3.1):

$$\lambda_{\text{eff}} = \lambda(E_{\text{kin}}) \cdot \cos\Theta\,. \tag{3.1}$$

Values for the *inelastic mean free path* (IMFP) and its dependency on the kinetic energy of the photoelectrons have been calculated by the semi-empirical TPP-2M model described in section 2.1.5 [49].
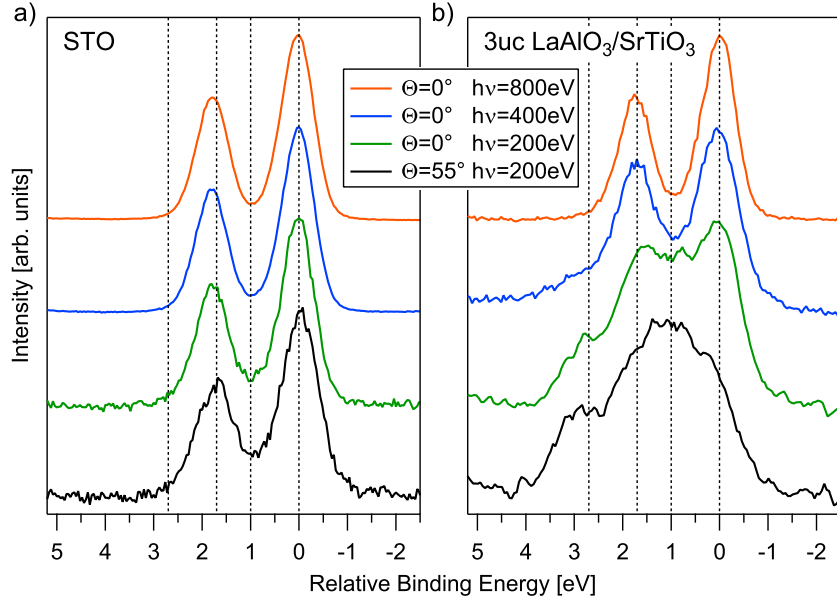
Figure 3.8: Background subtracted and normalized Sr $3d$ photoemission core level spectra of a STO substrate (a) and the 3 uc LAO/STO sample (b) measured at different photon energies $h\nu$ and emission angles Θ. Surface sensitivity is enhanced for lower photon energies and higher emission angles. The energy scale is referred to the Sr $3d_{5/2}$ maximum in order to neglect charging effects.

The STO spectra show two single peaks with little dependence of the shape on measuring parameters, although in the most surface sensitive conditions ($\Theta = 55°$, $h\nu = 200\,\text{eV}$) a slight broadening might be present. The spectra collected for LAO/STO, on the contrary, feature a strong dependence on λ_{eff}. Whereas the $h\nu = 800\,\text{eV}$ spectrum resembles the one of STO, at lower photon energies and higher emission angle an increasing high binding energy component is found, which dominates the spectrum for $\Theta = 55°$, $h\nu = 200\,\text{eV}$.

Such behavior is observed on the Sr $3d$ doublet of all the LAO/STO, NGO/STO and LGO/STO samples, irrespective of polar film thickness. The core levels of the other cations do not show, instead, any comparable dependence on the measuring conditions.

The change of the Sr $3d$ line in Fig. 3.8 is most naturally associated with the appearance of a second Sr component, which is chemically inequivalent with respect to the Sr^{2+} cations populating the perovskite A-site in STO. Alternative possibilities, as a strong band bending in STO near the interface, would also cause a λ_{eff} dependence of the spectra. Such hypothesis is nevertheless inconsistent with the absence of a comparable broadening for the other core levels. Furthermore, band bending would lead to a continuous shift of the peak positions of the Sr spectra as a function of λ_{eff} between the two extreme binding energy values, for which no evidence was found in the data.

In order to extract quantitative information from the spectra a global fitting scheme was implemented. All the spectra for a given sample have been fitted with two doublets and the following constraints:

- intensity ratio for the spin-orbit components has been set to 3 : 2

$$\frac{I_{d_{5/2}}}{I_{d_{3/2}}} = \frac{3}{2}\,,$$

- spin-orbit splitting is an atomic value and was set to 1.76 eV [37],

- equal *full width half maximum* (FWHM) and an equal Gaussian to Lorentzian ratio for doublet lines were imposed

$$\mathrm{FWHM}(d_{5/2}) = \mathrm{FWHM}(d_{3/2})\,,$$

- same energy separation between the two doublets and equal FWHM for each doublet were globally claimed for all measurements of a sample.
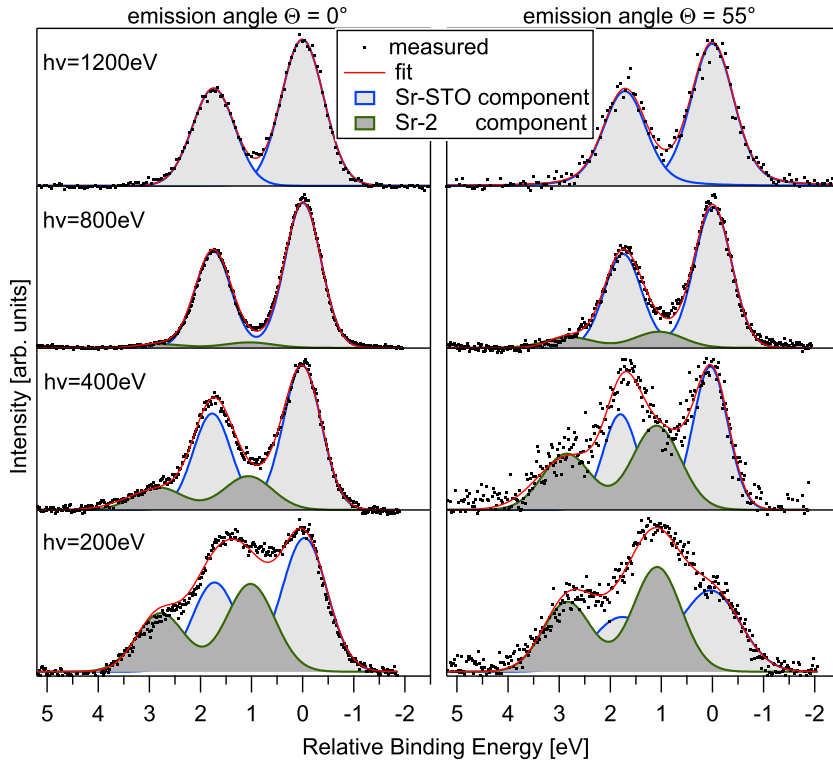
Figure 3.9: Fitted Sr 3*d* core level photoemission spectra of a 3 uc LAO/STO sample, that was measured at different photon energies $h\nu$ and emission angles Θ. For higher emission angles or lower photon energies (higher surface sensitivity) the second Sr component is enhanced.

Table 3.2: Global fit parameters for the three different heterostructures, given in eV.

| Parameter	3 uc LAO	3 uc NGO	6 uc NGO
Energy separation	1.06	0.95	1.00
FWHM(Sr-STO)	0.9	0.9	0.9
FWHM(Sr-2)	1.2	1.3	1.3

Such a global scheme is necessary since the spectral weight especially of the second doublet varies strongly with photon energy. In this manner, the energy separation between both doublets is mainly defined by very surface sensitive measurements (low photon energy), where both doublets can be well distinguished. Therefore, reliable values for the relative intensity up to $h\nu = 800$ eV can be extracted. At 1200 eV photon energy, the worse energy resolution and the decrease in spectral weight of the second component lead to indistinguishable doublets. This complex procedure has been applied to the data of a 3 uc LAO/STO, a 3 uc and a 6 uc NGO/STO sample.

Best fit curves for the 3 uc LAO/STO sample are plotted in Fig. 3.9, representatively. The plots for the 3 uc and the 6 uc NGO/STO samples can be found in the appendix (Fig. 5.1). The fit is of good quality and the fit parameters are shown in Tab. 3.2. For all three samples the same parameters satisfy and therefore validate the described procedure. The energy separation between the substrate and second Sr component is about 1 eV. The larger FWHM of the photoemission profile from the high binding energy component, called Sr-2 in the following, suggests a higher degree of disorder of Sr-2 cations with respect to the Sr-STO cations residing in crystalline STO.

In Fig. 3.9 it is obvious that the integrated intensity of the Sr-2 component increases for lower $h\nu$ and larger Θ compared to the integrated intensity of Sr-STO, proving that Sr-2 cations are located above the STO substrate.

Still, a number of more challenging issues about the Sr-2 component remain open:

- Where are Sr-2 cations located? Do they lying in-between LAO and STO? Are they homogeneously intermixed in LAO or do they segregate above LAO?

- Which is their amount?

- Which is their source and which is the origin of the chemical shift?

- Can they affect the interface properties?
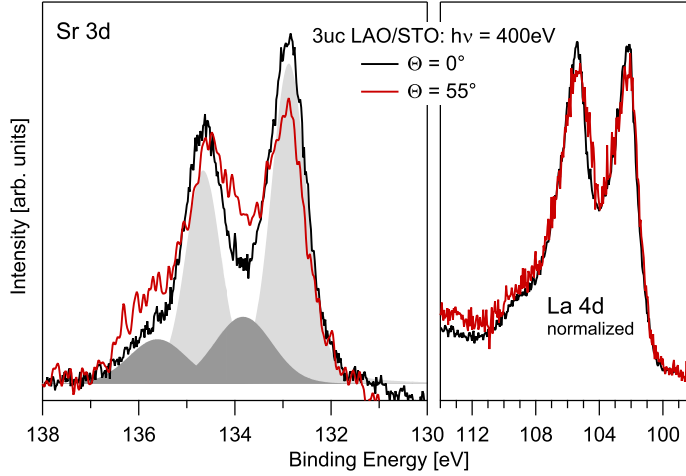
Figure 3.10: Sr $3d$ spectra (left) of the 3 uc LAO/STO sample measured at $h\nu = 400$ eV for both emission angles Θ. The data are normalized with respect to the La $4d$ intensity (right). The intensity for the Sr-2 component (dark gray shaded area) increases relatively for higher surface sensitive conditions ($\Theta = 55°$), whereas the Sr-STO intensity (light gray shaded area) decreases.

Location and amount of the Sr-2 species

The data for the integrated intensity ratio between Sr-2 and Sr-STO is not sufficient to answer the first question properly. It is more promising to compare the area below both components to the integrated intensity of core levels associated with elements of the overlayer material. To diminish errors caused for instance by the transmission function of the analyzer and different IMFPs, both depending on the kinetic energy of the photo-electrons, core levels energetically close to the Sr $3d$ excitation should be used primarily. In the case of LAO the Al $2s$, La $4d$ and Al $2p$ core levels lie in the energy range of 120 – 70 eV and comply with this restriction. In the following the integrated intensity of the Sr $3d$ line is compared to those of the La $4d$ line, since both share the same angular momentum quantum number exhibiting similar photoemission cross sections. In the left part of Fig. 3.10 the Sr $3d$ spectra for 3 uc LAO/STO measured at $h\nu = 400$ eV for both emission angles is plotted after normalizing them to the area of the corresponding La $4d$ line shown in the right part. The relative intensity of the Sr-STO component decreases, as expected, for higher surface sensitive conditions, e.g. $\Theta = 55°$. In contrast to this, the intensity of the Sr-2 component increases obviously.
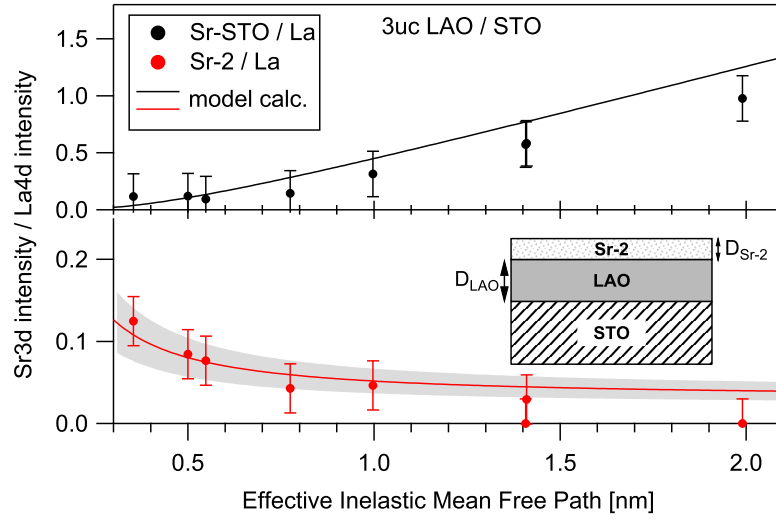
Figure 3.11: Sr $3d$/La $4d$ intensity ratio of the 3 uc LAO/STO sample vs. effective inelastic mean free path of the photoelectrons. Lines and gray area: Model calculations with $D_{\text{Sr}-2} = (0.035 \pm 0.01)$ nm. See main text for details. Inset: Sketch of the heterostructure including the inferred position of the Sr-2 component.

In Fig. 3.11 the *integrated intensity ratios* (IIR) between the Sr $3d$ and La $4d$ profiles in LAO/STO are plotted vs. λ_{eff} for both Sr components. Each data point corresponds to a given photon energy and emission angle, that is converted into λ_{eff}. The data were corrected for core level and photon energy dependent cross sections and asymmetry parameters [133]. As expected, the Sr-STO IIR decreases exponentially for lower λ_{eff}, due to the rising photoelectron damping by the LAO overlayer and the simultaneously increasing contribution of La. In contrast to this, the Sr-2 IIR (lower graph) increases for lower λ_{eff}. Once again, a similar behavior is observed for the NGO/STO samples shown in Fig. 3.12(a) and Fig. 3.12(b): the Sr-STO IIR measured with respect to Ga $3p$ rises with increasing λ_{eff}, while Sr-2 clearly shows an opposite trend.

If the Sr-2 cations were lying in between LAO (NGO) and STO, their IIR would show the same trend as Sr-STO. A homogeneous intermixing of Sr-2 in LAO (NGO) would cause a constant IIR vs. λ_{eff}. Only a top surface position of the Sr-2 cations entails the observed increase of IIR with decreasing λ_{eff}. Therefore, the measured IIR profiles can be compared to a model, which assumes an abrupt interface and an additional overlayer containing the Sr-2 species (see Fig. 3.11 inset). Within this scenario, the IIR values for Sr-STO and Sr-2 are expressed as a function of the thicknesses by Eq. 3.2 and 3.3 (see section 2.1.4):

$$\frac{I_{\text{Sr}-\text{STO}}}{I_{\text{La}}} = \frac{I^0_{\text{Sr}-\text{STO}} \times e^{-D_{\text{LAO}}/\lambda_{\text{eff}}}}{I^0_{\text{La}} \times (1 - e^{-D_{\text{LAO}}/\lambda_{\text{eff}}})}, \tag{3.2}$$

$$\frac{I_{\text{Sr}-2}}{I_{\text{La}}} = \frac{I^0_{\text{Sr}-2} \times \left(1 - e^{-D_{\text{Sr}-2}/\lambda_{\text{eff}}}\right)}{I^0_{\text{La}} \times \left(1 - e^{-D_{\text{LAO}}/\lambda_{\text{eff}}}\right) \times e^{-D_{\text{Sr}-2}/\lambda_{\text{eff}}}}. \tag{3.3}$$

Here the integrated intensities, directly extracted by fitting the data for Sr-STO, Sr-2 and La, are labeled with I.* I^0 reflects the concentrations and cross sections of the different elements. In order to reduce the number of free parameters we set $I^0_{\text{Sr}-\text{STO}} = I^0_{\text{Sr}-2}$, i.e. we assume the unknown atomic concentrations of Sr-2 to be equal to the Sr-STO case. D is the thickness of the layers (see Fig. 3.11 inset). The solid lines in Fig. 3.11 and 3.12 represent the calculated profiles of Eq. 3.2 and 3.3 for a 3 uc LAO and 3 uc and 6 uc NGO layer ($D_{3\text{uc}} = 1.2\,\text{nm}$, $D_{6\text{uc}} = 2.4\,\text{nm}$). The thickness of the Sr surface layer $D_{\text{Sr}-2}$ describing the datasets best is in the range of $D_{\text{Sr}-2} = 0.03 - 0.04\,\text{nm}$.
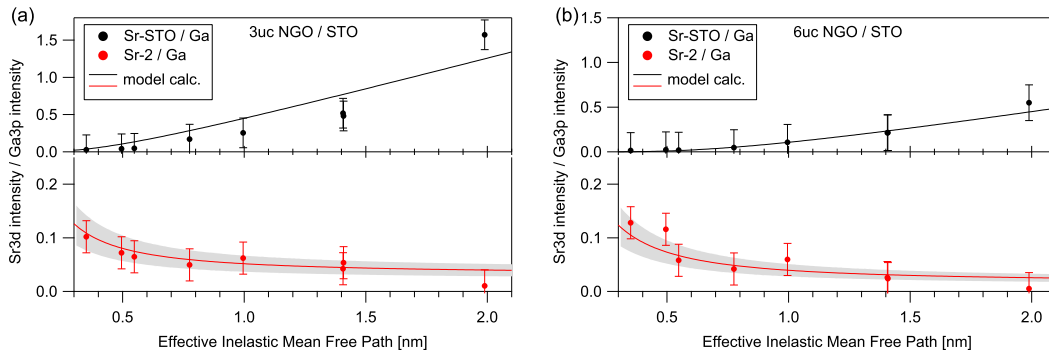
Figure 3.12: Sr $3d$/Ga $3p$ intensity ratio of the 3 uc NGO/STO (a), and 6 uc NGO/STO (b) sample vs. effective inelastic mean free path of the photoelectrons. Lines and gray area: Model calculations with $D_{\text{Sr}-2} = (0.035 \pm 0.01)\,\text{nm}$.

The model describes the data successfully and confirms that the Sr-2 cations lie predominantly at the surface of the heterostructures. $D_{\text{Sr}-2}$ appears to be much smaller than a STO unit cell and all λ_{eff}. For this situation the model employed in Eq. 3.2 and 3.3, which rests on the IMFP formalism, should be considered as an attempt to extract the order of magnitude of the top Sr concentration rather than exact quantization. The latter comes out as only a fraction of a single STO unit cell, which hints to partial coverage or island formation. The model itself assumes a homogeneous Sr-2 layer, realized if the Sr is incorporated in the terminating LAO layer or by finely dispersed Sr-based molecules or clusters. However, to discriminate between these situations or other forms of island growth is not possible based on the data in Fig. 3.11 and 3.12 with certainty and remains, in essence, a task for future studies. Interestingly $D_{\text{Sr}-2}$, i.e. the amount of Sr-2, appears to be independent of the chemical nature of the polar overlayer (LAO or NGO) and of its thickness.

---

*Substrate related spurious Si intensity has been observed for low λ_{eff}. The Si 2p line partly superimposes the La 4d line but can be removed by fitting with sufficient accuracy.

Laboratory XPS

The observation of the shown Sr segregation requires low photon energies, rarely used for core level studies. This is probably the reason why this interesting phenomenon escaped the attention of previous investigations [14, 134], although some broadening of the Sr $3d$ has been reported occasionally [81]. Standard laboratory XPS measurements with an Al K_α X-ray source were performed on the same 3 uc LAO/STO sample of Fig. 3.9 to confirm this statement. In Fig. 3.13 the result of the above mentioned global fitting scheme is plotted. In laboratory no tunable light sources are available and hence the sensitivity depth can be tuned by varying the emission angle Θ. To achieve small effective IMFPs, comparable to the synchrotron experiment described above, the angle between the sample surface normal and analyzer direction has to exceed 75°. Due to the cosinus of Θ in Eq. 3.1 the effective IMFP is quartered at 75° and reaches about 0.5 nm – the onset in Fig. 3.11 when the IIR of Sr-2 starts to increase. However, because of difficulties with the sample alignment and low intensities, larger emission angles are hardly feasible from an experimental point of view. Additionally, the surface roughness can strongly affect the IMFP due to scattering at the surface for grazing electron emission. The fitted spectra in Fig. 3.13 support the synchrotron data qualitatively. With increasing emission angle, i.e. raised surface sensitivity, the spectral weight of the broader Sr-2 component increases clearly. Note that a fixed energy separation of 1 eV between both components was demanded to ensure a well converged fit. Nevertheless, I abstain from quantitative statements due to expected large error bars because of problematic sample alignment and increased surface scattering at high emission angles. However, it has been demonstrated that the Sr segregation can be already observed with a laboratory XPS setup confirming the reliability of the synchrotron data.

Origin of Sr-2 species

Now, the origin of the Sr-2 component and its shift in binding energy is under consideration. The extra Sr might well migrate from the bulk of STO which can be considered for our purposes as an "infinite Sr reservoir". In this context, the driving force for Sr migration could either be an intrinsic non-stoichiometry of the single crystal or possibly the energy gain of a surface redox reaction of Sr in oxidizing conditions. As an alternative hypothesis, the excess Sr could lie initially on the nominally Ti-terminated STO surface as clusters of residual atoms (possibly close to step edges) not removed by the surface treatment nominally guaranteeing the single TiO_2 termination. This would suggest the existence of a driving force tending to maintain, even in the presence of a non-uniform STO termination, an uniform SrO-TiO_2-LaO-AlO_2 sequence across the whole interface,
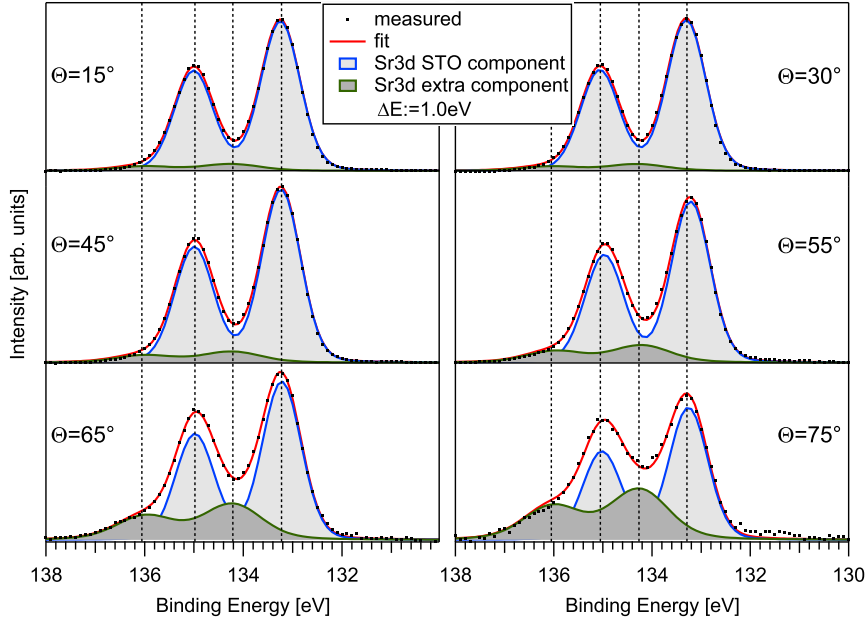
Figure 3.13: Laboratory Sr $3d$ core level photoemission spectra of a 3 uc LAO/STO sample measured with an Al K_α source at different emission angles Θ. The spectra were interpreted with the same global fitting scheme mentioned above. For higher emission angles (higher surface sensitivity) the second Sr component is enhanced.

by pushing the initial excess Sr to the top of the growing film. Finally, a finite amount of substrate surface Sr may be set free during the deposition process and experience an energy gain by floating at the surface of the heterostructure.

As for the binding energy shift between the two Sr components, it would be very tempting to attribute it to the electric potential foreseen to build-up across LAO, within the polar catastrophe scenario. Nevertheless the analysis of current literature suggests that a binding energy shift of pure chemical nature, rather than of electrostatic nature, might well play a role. Chemical shifts very similar to the ones reported above have been in fact reported for bare, thermally treated STO substrates and assigned to either SrO_x [135], or Sr bonded to carbon (e.g. $SrCO_3$) [136–138]. A formation of $Sr(OH)_2$, due to the reaction with water, can also cause a similar binding energy shift [137]. This hypothesis is consistent with the observation that binding energy shifts of electrostatic nature are hardly found in LAO/STO [82, 83, 134, 139].

### Sr-segregation and its impact on the physical properties

Any attempt to directly link the Sr segregation phenomenon to interface conductivity would be highly speculative at this point. Migration of positively charged Sr^{2+} atoms

from the interface to the upper LAO surface would certainly be an alternative or complementary way with respect to electronic reconstruction to alleviate the polar catastrophe. Nevertheless, this argument would apply to any of the four cation species present in the system. Furthermore, this effect could be neutralized, if the migration involved neutral Sr^{2+} - O^{2-} complexes rather than single ions. Finally, the very small amount of Sr-2 makes it insufficient to compensate a nominal polarity of $1/2\,e^-$ per two dimensional unit cell. In literature one can observe that the decade-long debate on the origin of the 2DEG in LAO/STO has taught us that the finest details in the atomic arrangement, including e.g. the STO atomic termination, or submonolayer differences in LAO thickness above 3 uc, or LAO stoichiometry variations of the order of 1 % [140], or undetectably low levels of oxygen vacancies, can alter the electronic properties of this system dramatically. Only a very accurate and complete understanding of the effective atomic configuration occurring in real systems will allow us to properly discern intrinsic and extrinsic effects.

Impact of growth conditions on the Sr segregation

Finally, I address recent measurements which were performed to figure out a possible impact of growth conditions on the Sr segregation. Therefore, two natural approaches were exploited. First, the amount of surface strontium was compared to a sample grown at three orders of magnitude lower oxygen partial pressure and secondly, the effect of a post-growth annealing step in oxygen was studied. Both are alternative ways to manufacture well oxidized and smooth, layer by layer grown oxide heterostructures. The three samples discussed above, 3 uc LAO, 3 uc and 6 uc NGO (grown at $p(O_2) = 10^{-2}$ mbar), were subsequently annealed and hold for 4 hours at 500 °C under 500 mbar oxygen pressure. Additionally, two 3 uc LAO/STO samples were grown in the same apparatus but under a lower oxygen partial pressure of $1 \cdot 10^{-5}$ mbar, whereby only one of them was exposed to the same post-growth annealing process in oxygen. The same photon energy and emission angle dependent measurements, discussed above, were carried out. The striking results are shown in Fig. 3.14 and a supplemental comparison of the whole dataset is attached (Fig. 5.3 and Fig. 5.2).

The Sr $3d$ spectra of the four 3 uc LAO/STO samples are normalized to the Al $2s$ intensity, shown in the right part of Fig. 3.14. Besides the comparison of the line shape, this also enables stoichiometric statements. All Sr spectra deviate from the generic STO spectra, which energy positions are marked with dashed lines. First of all, it is discernible that the differences to STO are larger for the as-grown (black, green curve) than for the post-growth treated samples (red, orange). The high binding energy component of Sr-2 seems to vanish upon oxygen annealing. More precisely, a part of the spectral
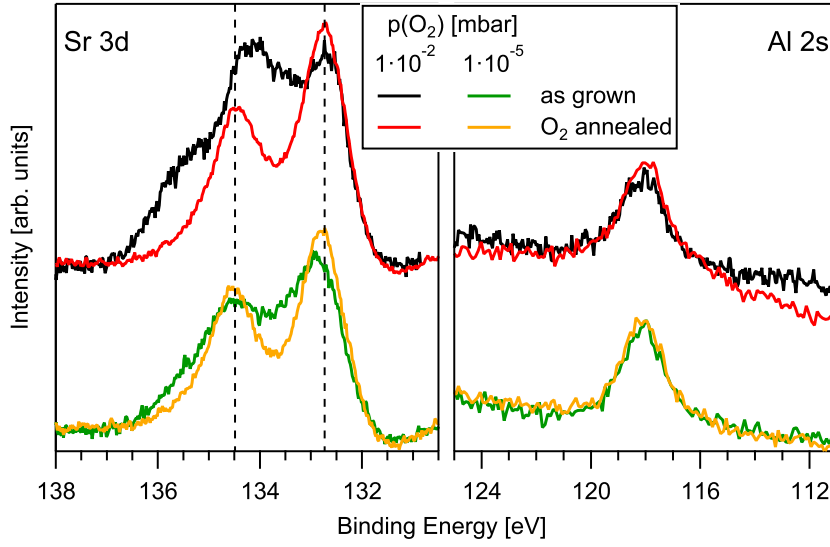
Figure 3.14: Sr 3d (left) core level photoemission spectra of different 3 uc LAO/STO samples measured at very surface sensitive conditions ($h\nu = 200\,\text{eV}$, $\Theta = 0°$). The spectra were normalized to Al 2s intensity (right). Both upper spectra were taken from samples grown under high oxygen partial pressure ($10^{-2}\,\text{mbar}$) and the two lower spectra from samples grown at $p(\text{O}_2) = 10^{-5}\,\text{mbar}$. The spectra of as-grown samples (black, green) and of samples exposed to a post-growth annealing step for 4 hours at $T = 500\,°\text{C}$, $p(\text{O}_2) = 500\,\text{mbar}$ (red, orange) are shown.

weight is transferred from the Sr-2 component to lower binding energy causing a slightly increased intensity of the STO component. However, the overall area underneath the profile is reduced compared to the Al 2s intensity. This behavior seen in Fig. 3.14 can be rationalized in the following way: former dispersed Sr or Sr–O molecules form upon oxygen annealing well oxidized clusters, which have the same spectroscopic signatures as Sr-STO. Due to the agglomeration in larger clusters, they contribute less to the spectrum. Note that this scenario is only possible if no Sr can vanish from the surface or can diffuse back to the interface. Both assumptions are justified by the high vapor pressure of Sr [141] and under the consideration that the post-annealing conditions are not much different from the growth conditions, respectively. The fact that the Sr 3d spectra of the annealed samples resemble the spectrum of Sr-STO is confirmed for all photon energies and also for the NGO/STO samples.

Secondly, the amount of surface Sr seems to be larger for the samples grown at higher than lower oxygen partial pressure. In particular, an increased high binding energy Sr-2 component is obvious for the black curve compared to the green curve, although both spectra are not plotted on top of each other for reasons of clarity. At first glance, this is surprising since a smoother growth is expected for higher oxygen pressure, which reduces the kinetic energy of the particles hitting the STO substrate. Nevertheless, the oxygen

pressure may be the driving force for the Sr diffusion away from the interface forming strontium oxide. Obviously, further investigations are necessary to understand every detail of the PLD growth process.

3.4 Electronic structure of polar/non-polar oxide interfaces

The electronic structure at the interface of polar/non-polar oxides is the primary topic of scientific interest. The nature of the highly mobile 2DEG and its intriguing properties raise questions about the origin of the conducting electrons. Chemical and structural modifications, such as the experimentally verified Sr diffusion to the surface, can affect the interface properties but do not seem to dominate the electronic structure. It is widely believed that the electron transfer from the surface to the interface region, caused by the rising electrostatic potential, induces the versatile 2DEG. Spectroscopic signatures corroborating this hypothesis are presented in this section. XPS measurements have been done in the IFW laboratory, whereas *resonant photoemission spectroscopy* (ResPES) and *X-ray absorption spectroscopy* (XAS) measurements have been carried out during various beamtimes at BESSY.

3.4.1 X-ray photoemission and absorption spectroscopy at Ti

Fig. 3.15 compares the titanium $2p$ core level and L-edge absorption spectra of LAO/STO samples with various overlayer thicknesses. The XPS spectra in Fig. 3.15(a) are referred to the peak maximum to encounter for sample dependent charging. The spectra consist of two main lines denoted by $2p_{3/2}$ and $2p_{1/2}$ separated by spin-orbit splitting of about 5.5 eV.

The spectra of the 1 uc and 2 uc LAO/STO samples coincide perfectly with the STO reference spectra. Their shape is characteristic for Ti with a valency of +4 and an empty $3d^0$ shell as it is the case for STO. The complex satellite features at higher binding energy, caused by charge transfer final state effects, are omitted for clarity. A low binding energy shoulder arises for samples with an overlayer thickness larger than the conductivity threshold. This region at about -2 eV relative binding energy is magnified in the inset and clearly shows additional spectral weight for the 5 uc and 6 uc thick samples. A little increased intensity of this feature is discernible for the 3 uc sample (blue curves in the inset). Low binding energy features in XPS are usually caused by a reduction of the valency of the respective site. Therefore, the occupation of former empty Ti $3d$ states in vicinity of the interface is proven. The complementary XAS Ti L-edge spectra of a 6 uc and a 2 uc LAO/STO sample are shown in Fig. 3.15(b). Here, the photon energy
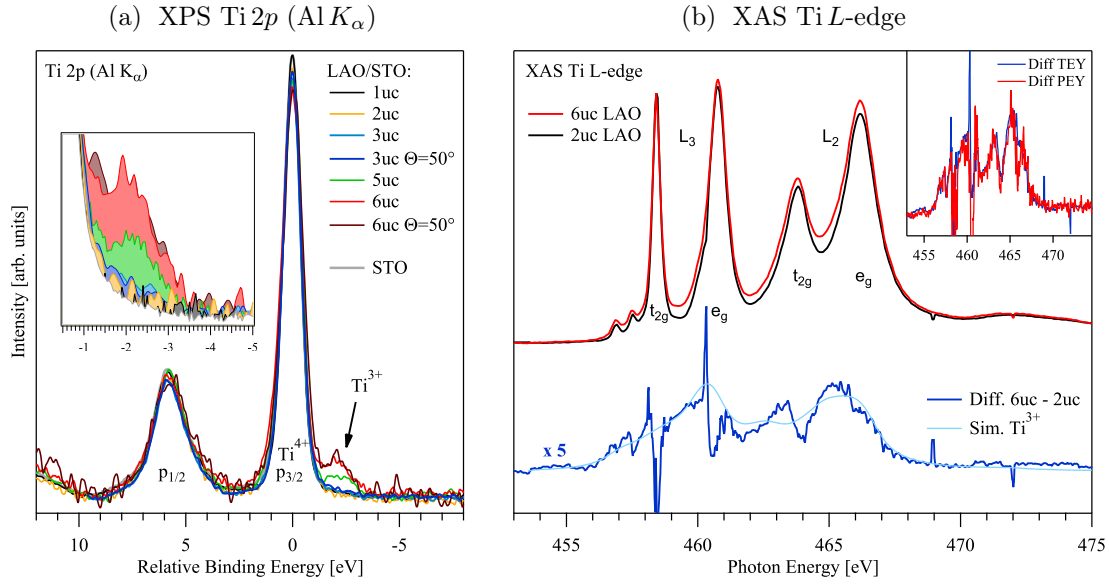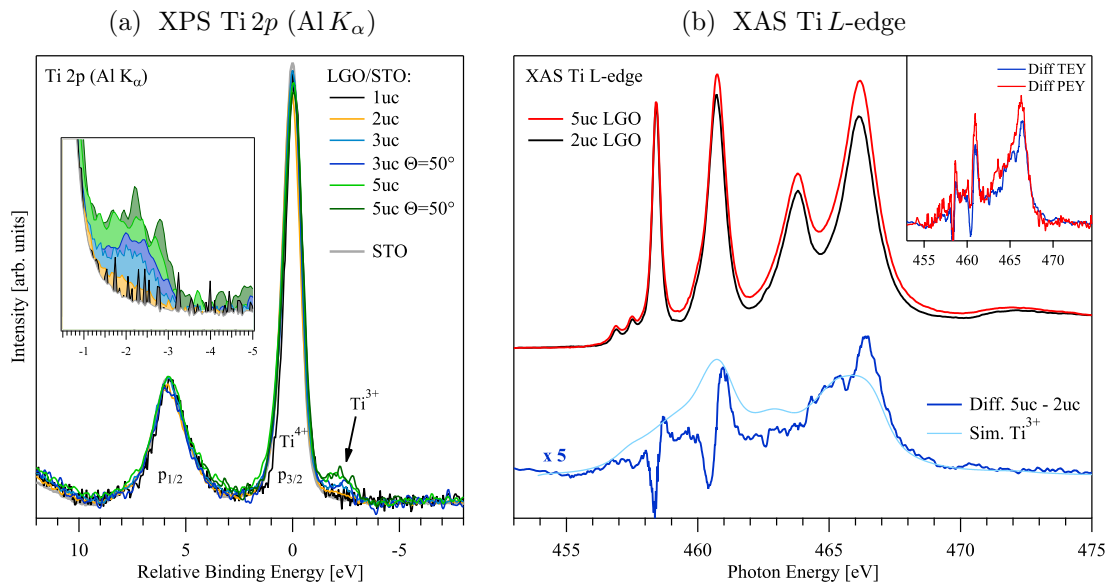
Figure 3.15: Ti $2p$ laboratory XPS spectra (a) of LAO/STO interfaces with various thicknesses and emission angles Θ. XAS Ti L-edge (b) of a 6 uc and 2 uc thick LAO/STO sample and their difference spectra in comparison to a simulated Ti^{3+} spectra.

dependent photocurrent of the sample has been measured. Again, these spectra resemble the typical Ti^{4+} related lineshape consisting of mainly four peaks, due to spin-orbit (L_3/L_2) and crystal field splitting denoted with t_{2g} and e_g, and less intense multiplet structures. The energy separation between the L_3 and L_2-edge is the same as the splitting in the XPS spectra. Furthermore, the energy separation of t_{2g} and e_g peaks is a direct measure of the crystal field splitting $10Dq$ of the empty states, which is in the range of 2.4 eV. Characteristic differences are found in the absorption spectra between 2 and 6 uc. In particular, the 6 uc sample shows an intensity enhancement in-between the t_{2g} and e_g peaks with respect to 2 uc, which is a sign of increased Ti^{3+} content. This is in agreement with the XPS results. Since this Ti^{3+} contribution is energetically not well separated from the more intense Ti^{4+}, as it is for XPS, it will be discussed on a more quantitative basis using a subtraction procedure. The blue curve represents the data after subtracting the 2 uc from the 6 uc spectrum. The overall line shape of this difference spectrum agrees to Ti^{3+} emission, which is verified by multiplet calculations (light blue curve). Ti^{3+} absorption spectra similar in shape can also be obtained from measurements on LaTiO$_3$ single crystals shown in Refs. [15, 142]. The spikes and deviations around the original Ti^{4+} L_3 peaks are due to changes in the peak positions as a function of layer number, which can be explained by distortion of the oxygen octahedron in STO close to the interface. The depth distribution of the extra electrons at the Ti sites can be investigated by tuning the surface sensitivity. Therefore, a larger emission angle of $\Theta = 50°$ has

been used in XPS and the absorption spectra have been measured in two yield modes, *total electron yield* (TEY) and *partial electron yield* (PEY). For PEY the low energy electrons are blocked from entering the detector by a retardation voltage, whereby the depth sensitivity of the absorption signal can be reduced. For high retardation the PEY information depth approaches the photoemission inelastic mean free path ($\lambda = 1.1\,\mathrm{nm}$ at $h\nu = 450\,\mathrm{eV}$). For TEY the information depth is larger ($\approx 3 - 4\,\mathrm{nm}$) [53, 54]. Both signals, TEY and PEY, are recorded during the absorption scans simultaneously. The difference spectra in the inset of the XAS graph are similar in shape and magnitude, irrespective of the yield mode. This indicates that the region of high Ti^{3+} concentration near the interface extends at least 3 nm towards the bulk. This is in accordance to the XPS data, which show no signs of increased Ti^{3+} spectral weight if the emission angle is increased. Representatively, this is shown for the $\Theta = 50°$ spectrum of the 3 uc and 6 uc LAO/STO sample. Both results are roughly consistent with previous estimations from X-ray photoemission spectroscopy [82, 143]. The Ti^{3+} XPS shoulder still increases from 5 uc to 6 uc LAO thickness but no further upturn was found for 12 uc, which is not shown in the graph. Transport measurements reveal a jump of the 2D charge carrier concentration at the critical thickness of 4 uc and afterwards a rather constant behavior [77]. The former is in line with the absence of Ti^{3+} intensity for LAO layers thinner than 4 uc and the latter with the demonstrated steady Ti^{3+} intensity for thicknesses of 6 uc and more. The 6 uc and 12 uc LAO/STO sample belong to a different batch of samples and the 6 uc sample exhibits also different properties which will be shown later in this work. Small variations in growth conditions can affect the amount of oxygen vacancies, can lead to the extrinsic doping and may explain the slight increase of Ti^{3+} signal from 5 uc to 6 uc. However, slightly increasing Ti^{3+} intensity was also reported in a HAXPES study (hard X-ray photoemission spectroscopy) by Sing *et al.* [143].

In Fig. 3.16 and Fig. 3.17 analogous comparisons of Ti 2*p* XPS and XAS data are given for LGO/STO and NGO/STO samples, respectively. Equal general conclusions can be drawn as for LAO/STO. Both techniques enable the detection of extra electrons at the Ti site for the three investigated polar/non-polar heterostructures. In contrast to LAO/STO, already a small Ti^{3+} shoulder in the XPS data of LGO/STO and NGO/STO is discernible with a monotonic increase up to 4–5 uc. Finite Ti^{3+} intensity was also observed frequently for the Ti 2*p* XPS line before the threshold [81, 82, 134], but could be in part defect related. LGO/STO shows a tiny angle dependency of this feature, that is confirmed by a slightly larger PEY XAS intensity compared to the TEY (see insets of Fig. 3.16). A smaller Ti^{3+} signal, but still a tendency to a higher signal for lower sensitivity depth, was also found for NGO/STO. One could roughly conclude that the 2DEG is confined up to 2 nm below the interface with a rather constant charge carrier concentration, which is lowered for TiO_2 layers further away from the interface.

Figure 3.16: Ti 2p XPS spectra (a) of LGO/STO interfaces with various thicknesses and emission angles Θ. XAS Ti L-edge (b) of a 5 uc and 2 uc thick LGO/STO sample and their difference spectra in comparison to a simulated Ti^{3+} spectra.
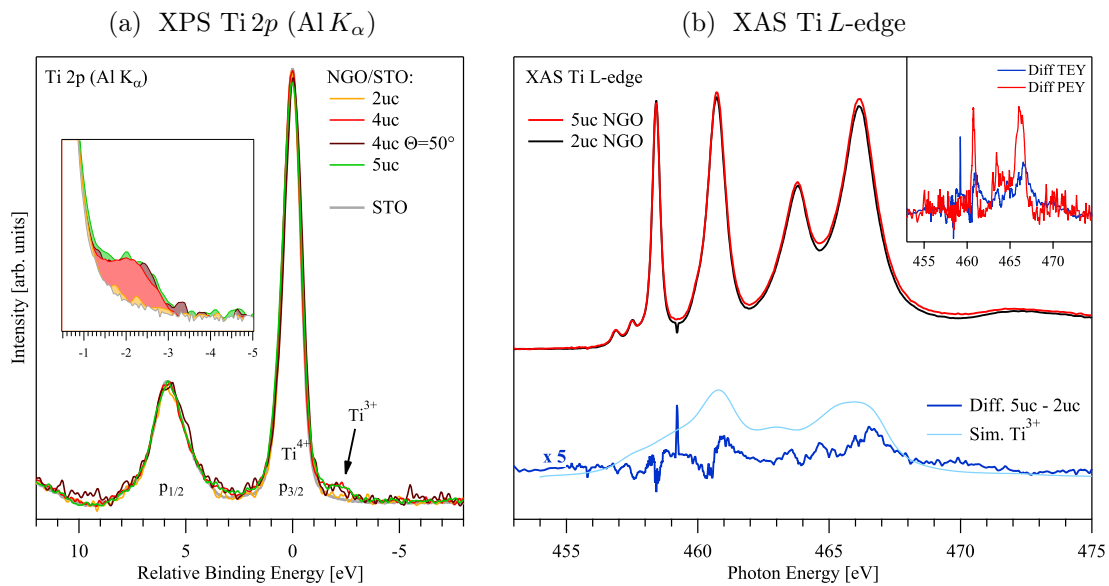

Figure 3.17: Ti 2p XPS spectra (a) of NGO/STO interfaces with various thicknesses and emission angles Θ. XAS Ti L-edge (b) of a 5 uc and 2 uc thick NGO/STO sample and their difference spectra in comparison to a simulated Ti^{3+} spectra.

(a) XPS Ti $2p$ (Al K_{α})   (b) XAS Ti L-edge
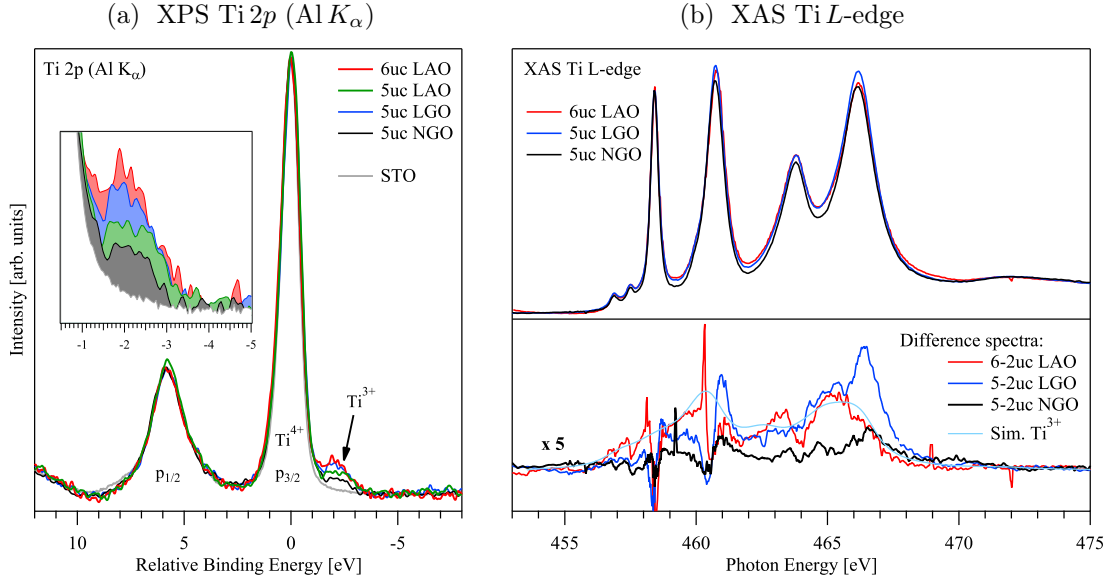
Figure 3.18: Comparison of Ti $2p$ spectra (a), XAS Ti L-edge and XAS difference spectra (b) of polar/non-polar heterostructures above critical thickness. Note, the difference spectra are emerged by a factor of 5.

Although the qualitative behavior of the three interfaces is similar, quantitative differences are revealed by a direct comparison. Thus, the spectra of three samples above thickness threshold are summed up in the same manner in Fig. 3.18 and their relative Ti^{3+} amount is given in Tab. 3.3. Fig. 3.18 shows the Ti $2p$ XPS and L-edge XAS spectra of 5 uc NGO/STO and LGO/STO as well as for 5 uc and 6 uc LAO/STO. Clearly, NGO/STO exhibits the lowest Ti^{3+} intensity for both, XPS and XAS measurements. Its low binding energy component in Ti $2p$ XPS is weaker than for LGO/STO and LAO/STO, that have approximately the same amount. This is confirmed directly by the observation of less XAS intensity between the t_{2g} and e_g peaks and more pronounced by the difference curve to a 2 uc sample. The LGO/STO and LAO/STO samples show similar shape and magnitude. The discrepancy in both difference spectra at higher photon energy can be traced back to differences in the background and again to thickness dependent energy shifts of the peaks. Note that 2 uc LGO/STO and NGO/STO exhibit already slight Ti^{3+} signal in XPS, that might be present also in XAS, and therefore may alter the XAS difference spectra. No reliable procedure could be applied to extract quantitative results from the XAS data. The relative amount of Ti^{3+} for XPS was estimated by fitting the Ti $2p_{3/2}$ peak with two Voigt profiles, one representing the Ti^{3+} and the other the Ti^{4+} species. The Ti $2p_{1/2}$ peak was not considered for the fit, since it possesses already an intrinsic asymmetric lineshape due to multiplet and final state effects [144]. Nevertheless, the Shirley background was subtracted over the whole Ti $2p_{3/2} - 2p_{1/2}$ energy range.

Depending on the constrains for the peak profiles and the chosen background slightly different concentrations could be achieved, which lie in the range of a 10 % error interval. In the presented analysis equal FWHMs for both peaks, Ti^{3+} and Ti^{4+}, were claimed.
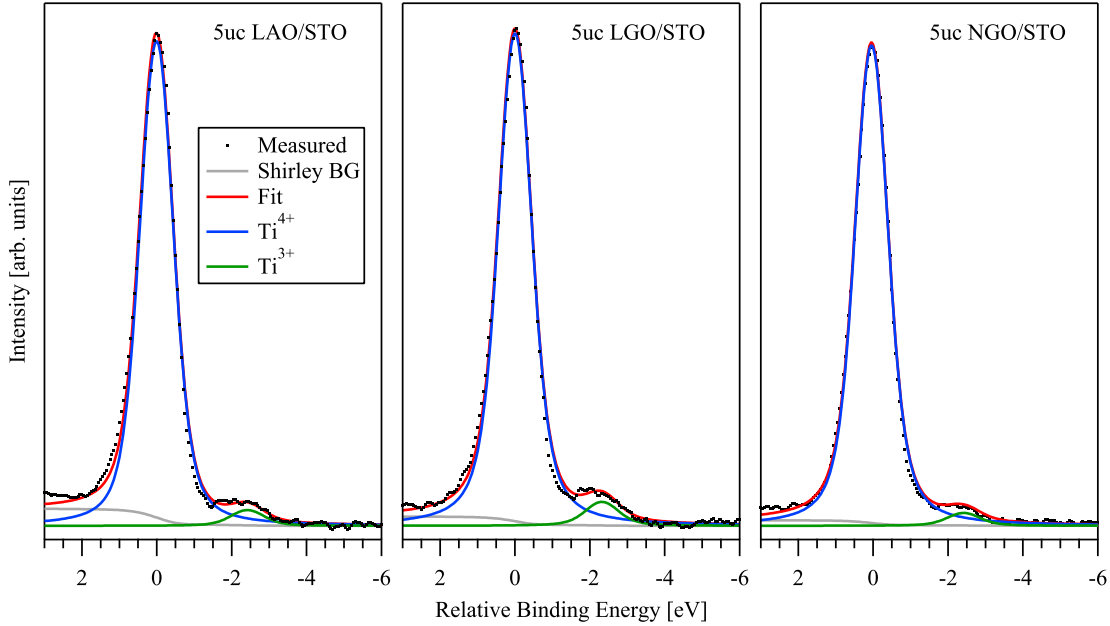
Figure 3.19: Fit of the measured $Ti\,2p_{3/2}$ peak with a Shirley background, subtracted over the whole $Ti\,2p_{3/2} - 2p_{1/2}$ energy range, and two Voigt profiles associated with Ti^{4+} and Ti^{3+}. In this way the relative Ti^{3+} intensity can be extracted for the 5 uc LAO/STO (left), LGO/STO (middle) and NGO/STO (right).

The fit presented in Fig. 3.19 is of good quality. After the subtraction of an empirical Shirley background [38] the three spectra can be fitted by the two Voigt profiles satisfactorily. The energy separations $\Delta E(Ti^{4+} - Ti^{3+})$ and FWHMs of the $2p_{3/2}$ peaks are the same for the three different polar overlayer materials, shown in Tab. 3.3. Compared to single crystalline STO the $Ti\,2p$ peak is not broadened (FWHM=1.1 eV), indicating a highly stoichiometric environment for the Ti ions even in the PLD grown heterostructures. Ishida *et al.* discussed the same signs of Ti^{3+} for Nb doped STO. They observed also an energy separation of about 2 eV and a relative intensity of approximately 6 % [145]. Following their interpretation, the valence of Ti is fluctuating between +3 and +4 with a time scale longer than characteristic time scales for a photoemission process ($\sim 10^{16}$ s). An alternative explanation for the two measured $Ti\,2p$ components is that a fraction x of the Ti sites has nominally a d^1 and the rest a d^0 configuration [145]. A measure for this fraction of Ti^{3+} ions is the relative integrated intensity of Ti^{3+} component, which is extracted by the fit in Fig. 3.19 and given in Tab. 3.3. Moreover, this value

can be used to roughly estimate the sheet carrier density n_{sheet}, if one assumes that the carriers are confined in a region with a thickness t of about $2\,\text{nm}$ as evaluated above:

$$n_{\text{sheet}} = \frac{\text{Ti}^{3+}}{\text{Ti}^{3+} + \text{Ti}^{4+}} \cdot \frac{t}{a^3} \quad . \tag{3.4}$$

Here, a denotes the cubic lattice constant of STO ($3.905\,\text{Å}$). The obtained values of about $1 \cdot 10^{14}\,\text{cm}^{-2}$ for n_{sheet} are comparable to transport data on samples grown in the same laboratory [21, 79] and close to the theoretical value of $3.2 \cdot 10^{14}\,\text{cm}^{-2}$ predicted by the "polar catastrophe", where $0.5\,e^-$ per 2D unit cell is transferred to the interface. They should be seen as a lower limit because a lower boundary of thickness with constant carrier concentration was assumed neglecting any contribution from free charges located further away from the interface. Transport data on well oxidized samples exhibit one order of magnitude lower charge carrier concentration [77]. However, localized charges are hidden in transport experiments but not in photoemission. Other techniques, for instance optical transmittance [146] or resonant inelastic X-ray scattering [147], have explicitly shown that more than one carrier species play a role. Samples, which suffer from a lack of oxygen, can easily show orders of magnitude higher sheet carrier concentrations [12], but in this case they cannot be addressed to an intrinsic property of the interface. However, because of the same deposition conditions and the fact that no Ti^{3+} signatures are detected for insulating LAO/STO, extrinsic oxygen defects seem to be an unlikely cause of Ti^{3+} spectral signs, shown in this chapter.

Table 3.3: Quantitative values and fit parameters concerning the relative Ti^{3+} concentration extracted from Ti $2p$ photoemission measurements. The error for the relative Ti^{3+} intensity is in the range of $10\,\%$ and can be significant higher for the estimated sheet carrier concentration.

Parameter	5 uc LAO	5 uc LGO	5 uc NGO
$\frac{\text{Ti}^{3+}}{\text{Ti}^{3+}+\text{Ti}^{4+}}$	3.1 %	4.6 %	2.5 %
$\Delta E(\text{Ti}^{4+} - \text{Ti}^{3+})$ [eV]	2.4	2.3	2.4
FWHM($\text{Ti}\,2p_{3/2}$) [eV]	1.1	1.1	1.1
n_{sheet} [$10^{14}\,\text{cm}^{-2}$]	1.0	1.5	0.84

3.4.2 Valence band photoemission spectroscopy

Experimental evidence for a partly reduced valency of titanium was demonstrated but this implies only in an indirect way that these carriers determine the interface properties. Rather localized electrons trapped in point defects will cause similar spectroscopic

signatures, extensively discussed in Refs. [15, 17]. A direct prove for metal-like behavior would be achieved by valence band photoemission spectroscopy. Laboratory valence band measurements could not be carried out successfully because of too low intensity and energy resolution for Al K_α XPS and tremendous charging caused by the intensive helium discharge lamp for UPS. Additionally, the electrons from the buried interface are exponentially damped by the overlayer material. Especially laboratory UPS with photon energies above 20 eV suffers from this since electrons with low kinetic energies have low inelastic mean free paths.

In the following, I want to present a study of the in-gap states by resonant photoemission spectroscopy (ResPES) at the Ti L-edge, a concept widely used to enhance the emission intensity of a specific site [17, 139, 142, 148, 149]. Thus, it is a convenient tool to obtain the partial density of states in the valence band [150]. For details see section 2.3. The ResPES synchrotron experiments have been carried out at BESSY, beamline UE52-PGM. In Fig. 3.20 the energy resolution is determined by fitting the Fermi-edge of a sputtered gold foil. The total energy resolution is given by:

$$\Delta E_{\mathrm{Instr}} = \sqrt{(4 \cdot \Delta E_{\mathrm{Fit}})^2 - (4 \cdot \Delta E_{\mathrm{Temp}})^2} = \sqrt{(4 \cdot k_{\mathrm{B}} T_{\mathrm{Fit}})^2 - (4 \cdot k_{\mathrm{B}} T_{\mathrm{Temp}})^2} \qquad (3.5)$$

Here, ΔE_{Fit} denotes the overall energy resolution extracted by the fit (see table in Fig. 3.20(a)) and $4 \cdot \Delta E_{\mathrm{Temp}}$ is the temperature broadening which is 100 meV at room temperature. The instrumental energy resolution for photon energies at the Ti L-edge is between $140 - 220$ meV depending on the chosen experimental parameters like beamline exit slit, analyzer entrance slit and pass energy, but is sufficient to resolve the relatively broad features in the valence band. This statement is confirmed by Fig. 3.20(b), which compares the spectral features measured at the oxide interfaces close to E_{F} and the Fermi-edge of the gold foil. In this study all spectra have been recorded in an angle integrated manner (transmission mode of the hemispherical analyzer).

Main characteristics of the valence band and normalization procedure

Prior to the investigation of the resonant photoemission spectra, one has to identify the features of the valence band in a wide energy range. The valence band characteristics of STO, LAO/STO heterostructures and pure LAO are explained in Fig. 3.21 based on the laboratory Al K_α XPS dataset. The spectra were energetically aligned concerning the C 1s peak. Referencing the C 1s peak to the ordinary energy position of surface contamination (285 eV) is a common procedure to account of sample dependent charging of semiconducting or insulating materials upon irradiation. The valence band, which is dominated by O 2p density of states, is located between 3 and 9 eV. Two main intensity
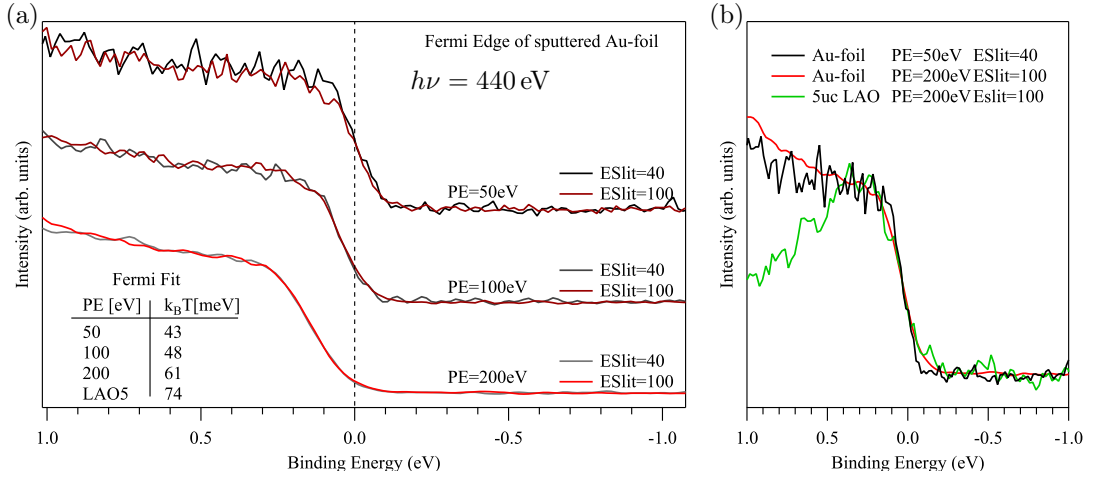
Figure 3.20: (a) Comparison of the width of the Fermi edge at 440 eV photon energy which was extracted by fitting and which corresponds to an instrumental energy resolution given by Eq. 3.5. (b) The sufficient energy resolution is confirmed by a comparison of the spectral features measured for the oxide interfaces and the Fermi-edge of the gold foil.

maxima, named V1 and V2, occur in this energy range. The peaks at higher binding energy are known as shallow core levels. Around 20 eV several features are visible. Two of them have mixed contributions and are therefore labeled with P1, P2 and the third peak can be associated with an O 2s excitation, which is very similar for LAO and STO. For STO P1 is absent and P2 belongs to an excitation of the Sr 4p core level with a small, not well resolved spin-orbit splitting. In pure LAO both features are present and belong to a La 5p excitation with a spin-orbit splitting of about 2.5 eV [151]. The LAO spectrum was calculated from a spectrum of a relative thick (12uc) LAO/STO heterostructure, that was corrected for residual STO contribution. The LAO/STO spectra can be described as linear superposition of both constituents. Thus, P1 and its relative intensity to P2 grow with increasing layer number, although La 5p contribute to both peaks. The same trend occur at around 36 eV, where the La 5s peak increases relative to the STO constituents, an overlap of Ti 3p and Sr 4s excitations. At about 26 eV a peak emerges depending on the sample, which could not be assigned to either LAO or STO. It was identified as an F 2s excitation of fluorine atoms distributed over the sample surface. This feature was also present on TiO$_2$-terminated STO substrates. Consequently, it stems presumably from substrate production or from the termination procedure by etching with buffered hydrofluoric acid (BHF). The most interesting region is the vicinity of the Fermi energy ($E_F = 0$ eV binding energy). Due to the low density and the damping of the photoelectrons by the LAO overlayer, there are no / tiny signs of spectral weight close to E_F in the Al K_α data, which can be attributed to mobile carriers.
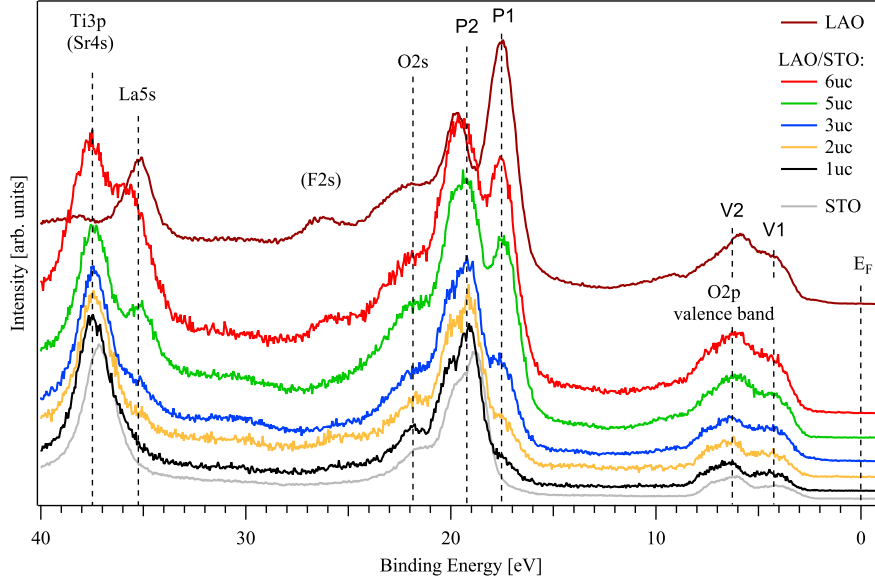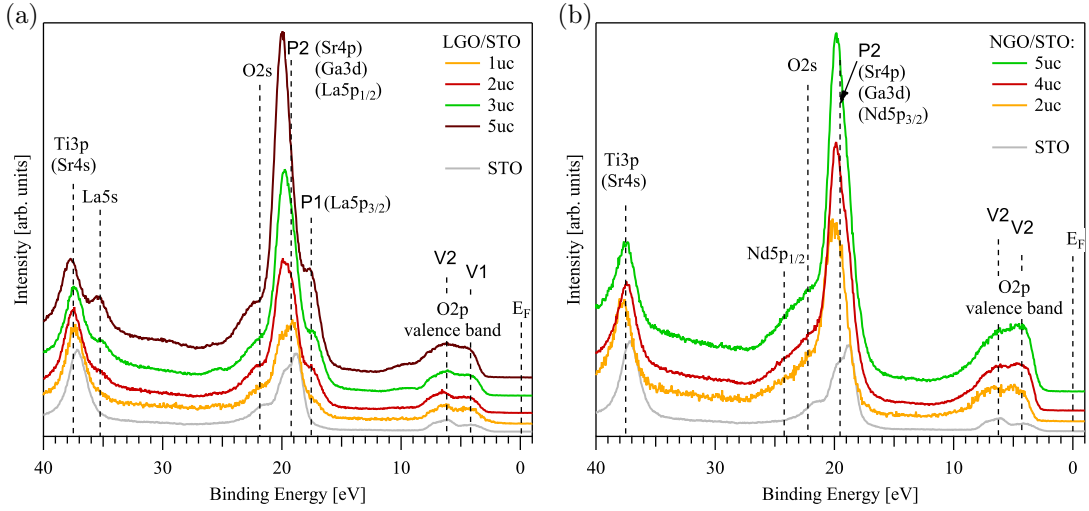
Figure 3.21: Photoemission valence band spectra and shallow core levels measured with an Al K_α X-ray source for STO, LAO/STO samples with increasing thickness and pure LAO, plotted from bottom to top. For the LAO spectrum a 12 uc LAO/STO spectrum was corrected for residual STO contribution.

For a quantitative analysis of the charge carrier concentration at the STO side of the interface one has to account of the overlayer damping, which can be done in various ways. Here, "quantitative" means not the specification of absolute numbers for the charge carrier density but rather a comparison of their relative amount between different heterostructures. Therefore, the data have to be normalized according to the STO signal. In Fig. 3.21 the shallow core levels around 20 eV were fitted by a linear combination of the LAO and STO constituents. All spectra except the pure LAO have been normalized for equal intensity of the STO constituent. This is confirmed by an almost equal Ti $3p$ signal at 37.5 eV, which can be used for normalization, too. For synchrotron experiments, also intensity above E_F, originated from higher harmonic light with doubled energy, could be considered for the normalization procedure. However, this intensity vanishes for larger thickness, thus only the first two methods were used in the following.

In the case of NGO/STO and LGO/STO heterostructures, shown in Fig. 3.22, the situation is quite similar except of an intense peak close to P2. This peak is dominated by a Ga $3d$ excitation, which has a higher photoemission cross section than the other involved shallow core levels (Sr $3p$, La $5p_{1/2}$ and Nd $5p_{3/2}$). Additional differences concern the La and Nd shallow core levels. For LGO the P1 (La $5p_{3/2}$) and La $5s$ features are discernible, comparable to LAO/STO heterostructures, while both are absent in NGO. However for NGO a Nd $5p_{1/2}$ line arises as high binding energy shoulder of the O $2s$ peak, due to the

larger spin-orbit splitting than for La $5p$. The overlap with the intense Ga $3d$ feature complicates the normalization by the Sr $4p$ line. Therefore, the Ti $3p$ excitation, which has the same intensity in Fig. 3.22 regardless of overlayer thickness, was predominantly used for the gallium based heterostructures. Note that under this circumstance the Re-sPES spectra have been normalized for off-resonant conditions. On Ti L resonance also the Ti $3p$ shallow core level is enhanced and cannot be considered for normalization.


Figure 3.22: Photoemission valence band spectra and shallow core levels measured with an Al K_α X-ray source for STO, LGO/STO (a) and NGO/STO samples (b) with increasing thickness, plotted from bottom to top.

Resonant valence band spectra at Ti L-edge

Usually, the same energy region as shown in Fig. 3.21 and Fig. 3.22 is measured for ResPES while scanning the photon energy across an absorption edge. In this work, ten selected photon energies at the Ti L-edge have been used to measure a large variety of heterostructures during several synchrotron beamtimes. The photoemission spectra have been recorded with photon energies at the absorption edge (on-resonant), where highest resonance effects occur, as well as before/behind the absorption edge (off-resonant). In the following, I will distinguish between T^{4+}- and T^{3+}-resonance conditions, which correspond to photon energies at the maxima of the Ti^{4+} spectrum of STO and to photon energies in-between the maxima in which Ti^{3+} has in part its absorption maxima, respectively. The chosen photon energy values are given and marked with colored bars in Fig. 3.23(a). The corresponding valence band spectra are shown with same colors and arbitrary offsets exemplary for a TiO_2-terminated STO substrate (Fig. 3.23(b)) and a 5 uc LAO/STO heterostructure (Fig. 3.23(c)). Note that identical colors were used in

all following graphs, which compare a certain binding energy region at different photon energies along the Ti L-edge.
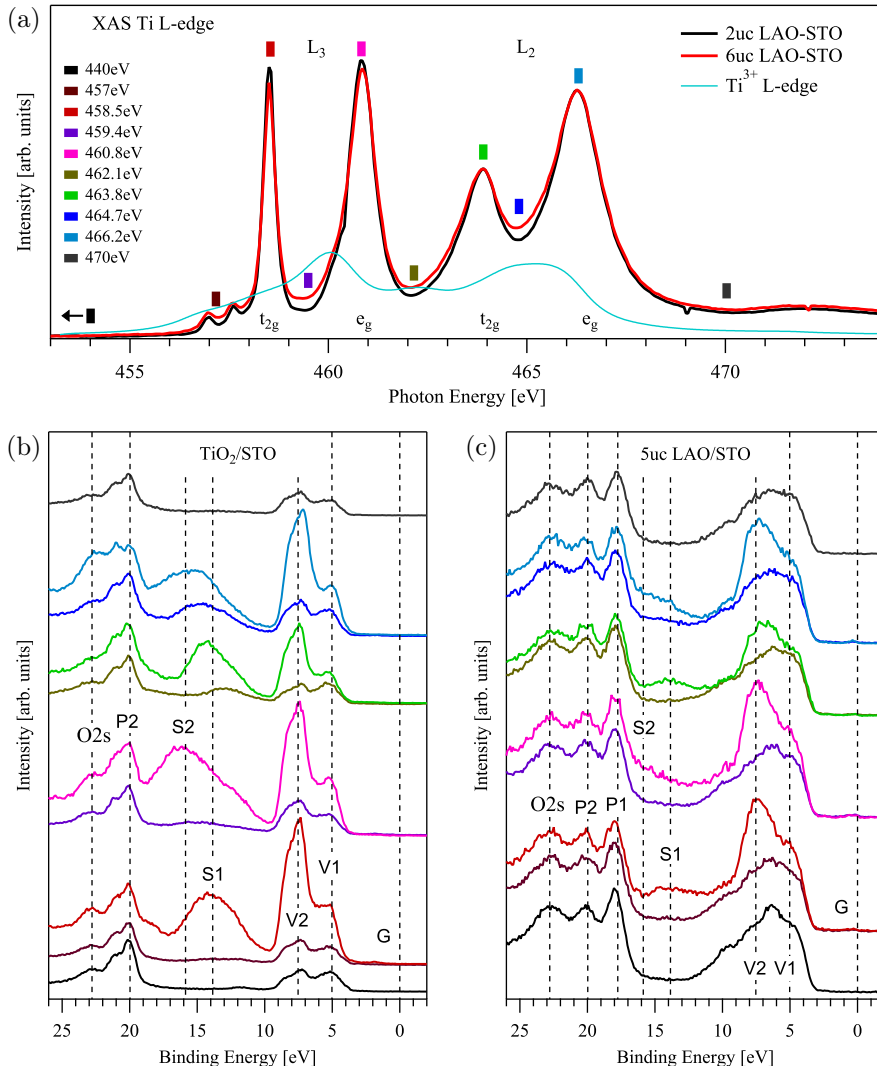
Figure 3.23: (a) Representative Ti L-edge absorption spectra and a calculated Ti^{3+} spectrum. Colored bars indicate the chosen photon energies, at which the resonant valence band spectra were taken, here exemplary for STO (b) and $5\,uc$ LAO/STO (c). In the following the same colors were used for the detailed spectra in vicinity of the Fermi energy.

The already mentioned features, which correspond to shallow core levels (O $2s$, P1, P2) and the valence band (V1 and V2), can be observed with photon energies around $440\,eV$ as well as for the Al K_{α} data (Fig. 3.21). Nevertheless, due to changes in the photoemission cross sections and surface sensitivities, differences especially for the intensity ratios occur. The P2 intensity of $5\,uc$ LAO/STO, for instance, is almost equal to the P1 intensity in Fig. 3.23(c), whereas it is higher for the Al K_{α} spectra, because of the

larger contribution of the substrate constituents (Sr $3p$) for higher photon energies. Apparently, strong resonance effects occur at certain photon energies. Especially for Ti^{4+} on-resonant conditions (red, pink, light green and blue curve) a tremendous intensity increase for the valence band and satellites at around $15\,\text{eV}$ can be seen, which are larger for the STO sample than for the 5 uc LAO/STO heterostructure. Resonance effects for photon energies at the Ti L-edge can only occur at Ti sites, which leads to the relative intensity differences between both samples. The resonantly enhanced features of STO are exponentially damped by the overlayer, being a 5 uc LAO film in the shown example. In a pure ionic picture, there are no intra-atomic Auger-decay channels in the O $2p$ energy region available, but DFT calculations reveal finite hybridization between O $2p$ and Ti $3d$ orbitals in STO [152]. Including hybridization the Ti-state of STO has to be considered as admixture of a $3d^0$ and a $3d^1\text{L}^1$ state, whereby L denotes a ligand hole in the O $2p$ orbitals:

$$|\text{Ti}^{4+}_{\text{STO}}\rangle = a \, |\text{Ti}3d^0 \, \text{O}2p^6\rangle + b \, |\text{Ti}3d^1 \, \text{O}2p^5\rangle := a \, |3d^0\rangle + b \, |3d^1\text{L}^1\rangle \, .$$

The enhancement of the valence band is a result of the coherent interference between the direct photoemission channel and the participator decay channel (autoionization) of the $3d^1\text{L}^1$ initial state leaving the system in a $3d^0\text{L}^1$ final state with still one ligand hole. Therefore, the resonant enhancement of features V1 and V2 is a proof for O $2p$-Ti $3d$ hybridization [153]. The high binding energy region of the O $2p$ valence band (V2) originates from orbitals with $t_{2\text{g}}$ and e_g symmetry. Because of this, a higher admixture with Ti $3d$ orbitals, which have the same symmetry, exists and the resonance effects are larger for these bonding states compared to the non-bonding V1 states located at lower binding energy [145, 153, 154].

The broad satellite features S1 and S2 resonate at $t_{2\text{g}}$ and e_g absorption maxima, too. In contrast to V2, both have a different binding energy indicating a spectator like decay. They can be associated with a $3d^1\text{L}^2$ final state configuration [17], whereby L^2 denotes two ligand holes (O $2p^4$) attracted by the core hole. Moreover, their energy separation matches approximately with the crystal field splitting of the Ti $3d$ orbitals. Spectator decays are characterized by an equal kinetic energy irrespective of the photon energy. This leads to the virtual shift in binding energy between $t_{2\text{g}}$ and e_g resonances, which is indeed noticeable for both samples.

In-gap excitations of LAO/STO

The central part of this study is the low binding energy region $(0 - 2\,\text{eV})$, labeled with
G in Fig. 3.23. In-gap states will arise here if partially occupied Ti $3d$ electrons exist in
the system close to the Fermi energy E_F. Detailed measurements of this region have
been performed for all samples. An overview of TiO$_2$-terminated STO substrate and of
LAO/STO heterostructures with different overlayer thicknesses n is shown in Fig. 3.24.
Again, the colors correspond to the same photon energies at specific structures in the XAS
spectrum. The leading edges of the valence bands have been used for energy alignment
and normalization. For STO and LAO/STO with $n \leq 2$, well below the conductivity
threshold, no intensity in the vicinity of E_F could be detected, except a feature linearly
dispersing to lower binding energies with increasing photon energy, which is emphasized
by the red line. This is the opposite direction as expected of a spectator decay, as it is seen
for S1 and S2. Since this feature survives above E_F the only plausible explanation is a core
level excitation caused by a higher photon energy. Photons with doubled energy can occur
in undulator beamlines equipped with a monochromator. While crossing an absorption
edge these photons excite electrons of the corresponding core level, Ti $2p$ in this case,
which has the same kinetic energy as the valence band excited by the primary photons.
Although their relative intensity should be relatively small, their spectral signs become
dominant around the magnified E_F region. Apart from that, the intensity is basically
flat indicating the absence of Ti related in-gap states and in particular the absence of
metallicity. Tiny spectral weight at around $1 - 2\,\text{eV}$ binding energy are observable just
for STO. In the past, they have been associated with localized defect states caused by
oxygen vacancies [17, 149, 154] or with incoherently screened decay channels due to strong
correlations [145]. Their absence in insulating LAO/STO samples grown under well
oxidizing conditions favor the scenario of oxygen defects, which are probably promoted
by the TiO$_2$-termination procedure in pure STO.

For $n = 3\,\text{uc}$ a clear intensity build up centered above E_F at about $E = 0.3$ eV and a
shoulder structure around $E = 1 - 1.5\,\text{eV}$ (G2) is found. The $E = 0.3\,\text{eV}$ feature, labeled
with G1, is noticeably enhanced for $5\,\text{uc}$ and $6\,\text{uc}$. Note, both spectra are multiplied with
a factor $1/4$ after normalization to the STO substrate. G1 is particularly intensive for
photon energies, where the Ti^{3+} absorption is large, i.e. for the purple and light blue
spectrum as can be seen in Fig. 3.23(a). The observation of two in-gap features with
different binding energy is consistent with previous publications [17, 149, 155]. The near
E_F spectral weight is responsible for the metallic behavior of the interface, whereas the
higher energy feature is defect related as already mentioned above for STO.
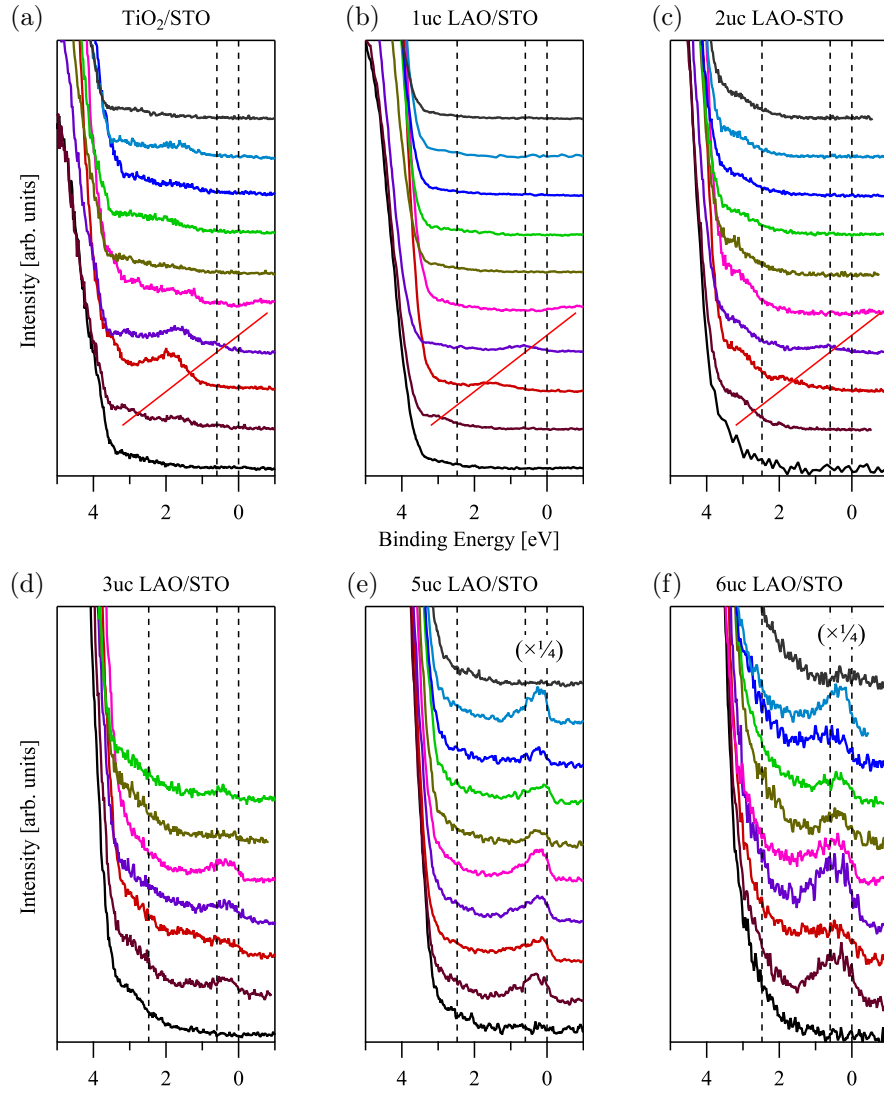
Figure 3.24: Detailed resonant photoemission spectra of the low energy region are plotted for TiO$_2$-terminated STO and 1 uc–6 uc LAO/STO. Higher order excitations from the Ti $2p$ core level are emphasized with the red line. Emission from in-gap states with a Ti $3d$ character arise for samples with an overlayer thickness of at least 3 uc. The spectra were normalized to the STO substrate to account for overlayer damping. Note that the spectra for 5 uc and 6 uc LAO/STO are downscaleded by a factor of $^1/_4$.

The right part of Fig. 3.25 shows the in-gap features for different layer numbers on-/off-resonant and in direct comparison, whereby the normalization procedure is illustrated by the left part. The gray area marks the STO contribution, which has the same amount for all thicknesses. While the intensity enhancement for $n = 5$ uc and 6 uc is in line with the insulator to metal phase transition at $n = 4$ uc [21, 77], the observation of near E_{F} in-gap

intensity for 3 uc is surprising as the samples are still insulating by then. This result is on the one hand in line with the observations by Drera *et al.*, who found near E_{F} in-gap intensity for both 3 uc and 5 uc, though with different intensity [142]. On the other hand Cancellieri *et al.* reported recently no in-gap intensity for $n = 2.5$ uc for a similar resonance photoemission experiment [149]. As for the clear difference between the 2 uc and 3 uc LAO/STO sample one can speculate that finite roughness could play a role. A finite fraction of the surface will be unavoidably covered with the fourth layer already when the third layer is completed during the deposition. The electronic reconstruction may set in but locally confined. Those regions will be isolated and macroscopic metallic behavior cannot occur until the fourth layer is deposited. However, the finite spectroscopic signs for metallicity for 3 uc coincide with an already slightly increased Ti^{3+} shoulder for the Ti $2p$ XPS line, shown in Fig. 3.15. Such intensity was also frequently observed before the threshold [81, 82, 134], and could be also defect related.
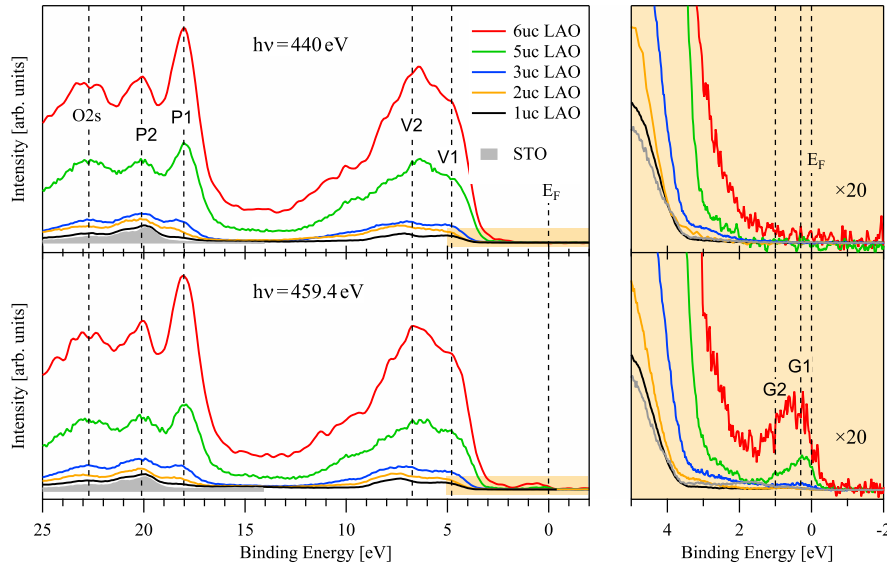

Figure 3.25: Direct comparison of off- and on-resonant valence band spectra and shallow core levels for STO, as well as for 1, 2, 3, 5 and 6 uc LAO/STO. The region around E_{F} (yellow background) is magnified in the right part by a factor of 20.

## In-gap excitations of LGO/STO and NGO/STO

The binding energy region close to E_{F} is plotted upon variation of the photon energy for the 2, 3 and 5 uc LGO/STO samples in Fig. 3.26 and for the 2, 4 and 5 uc NGO/STO samples in Fig. 3.27. In accordance with LAO/STO, in-gap states appear exclusively for photon energies at the Ti L absorption edge and are absent far below and above the absorption edge. The feature consists of a low energy component at 0.3 eV (G1), which is cut

by the Fermi function, and of a less intense high binding energy shoulder at around $1\,\mathrm{eV}$ (G2). Consequently, its Ti $3d$ character is proven as well as the metallic delocalized and localized origin of G1 and G2, respectively. Similarly to LAO/STO, intensity variations for different photon energies are present for LGO/STO and NGO/STO heterostructures following the Ti^{3+} absorption edge.
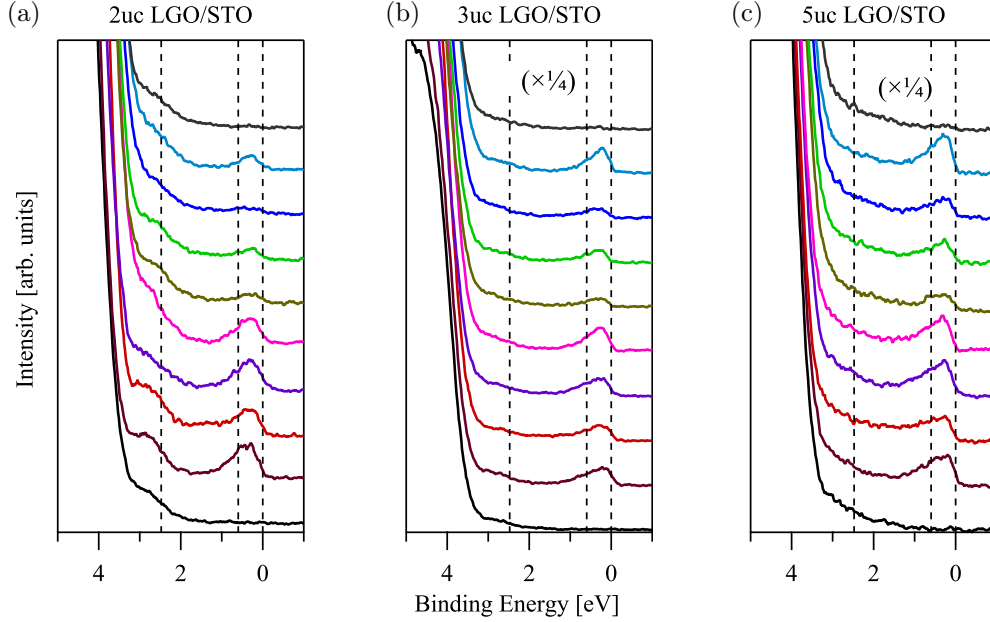
Figure 3.26: Detailed resonant photoemission spectra of the low energy region are plotted for 2, 3 and $5\,\mathrm{uc}$ LGO/STO. Emission from in-gap states with a Ti $3d$ character arise for all samples, but increase with overlayer thickness significantly. The spectra were normalized to the STO substrate to account for the overlayer damping. Note that the spectra for $3\,\mathrm{uc}$ and $5\,\mathrm{uc}$ LGO/STO are downscaled by a factor $1/4$.

However, finite in-gap states are already present for the $2\,\mathrm{uc}$ samples well below the conductivity threshold of $4\,\mathrm{uc}$. While their intensity increases significantly with layer number for LGO/STO, again illustrated by the factor $1/4$, only a slight intensity upturn is obvious for NGO/STO. A direct thickness comparison of in-gap states in the same manner as for LAO/STO is given for LGO/STO and NGO/STO in Fig. 3.28 and Fig. 3.29, respectively. The shallow core level region for Ga-based heterostructures is totally dominated by the strong Ga $3d$ emission making the Sr $4p$ normalization impossible, which was used for LAO/STO. Therefore, the spectra were firstly normalized to the Ga $3d$ emission and secondly the different layer thicknesses n were accounted by multiplication of the appropriate damping factors depending on n. As a result of this procedure, the intensity of the Ga $3d$ line increases with overlayer thickness as illustrated in the left part of Fig. 3.28 and Fig. 3.29. This normalization to the STO substrate was verified by an equal intensity of
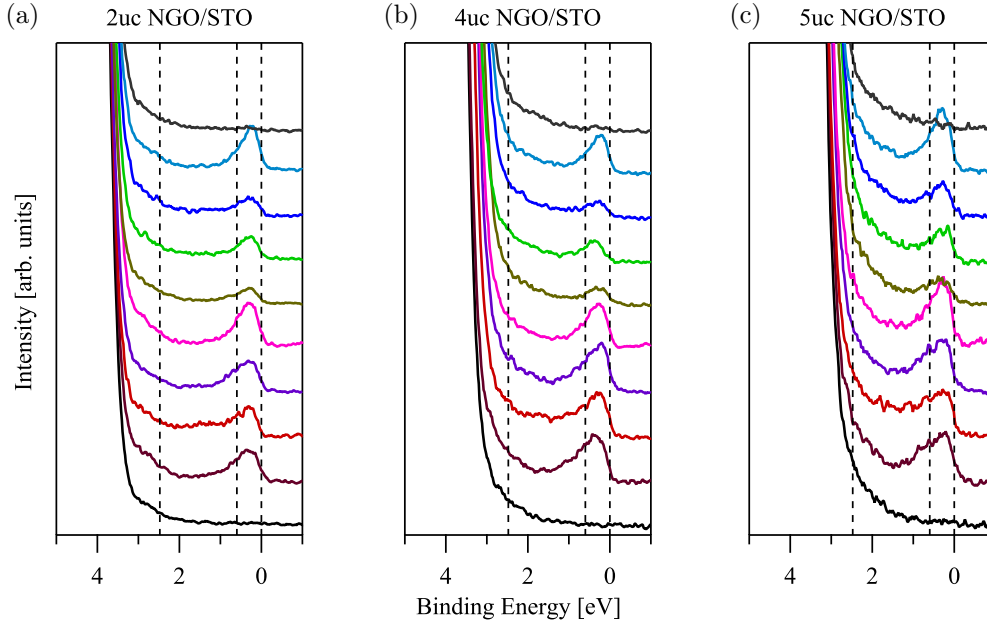
Figure 3.27: Detailed resonant photoemission spectra of the low energy region are plotted for 2, 4 and 5 uc NGO/STO. In contrast to LAO and LGO, emission from Ti $3d$ related in-gap states are present for all samples with similar intensity upon normalization to the STO signal.

the Ti $3p$ line at 37.5 eV binding energy. The magnification factor for the E_F region (right part of Fig. 3.28 and Fig. 3.29) was chosen to be 400, much higher than for LAO/STO, again because of the strong Ga $3d$ emission. In the case of LGO/STO obviously the G1 peak at E_F exists and increases with n. The intensity of the in-gap states is approximately the same for 4 uc and 5 uc NGO/STO. In fact, it saturates at 4 uc, which is in line with the critical thickness. While the occurrence of a less intense G1 peak in 3 uc LAO and 2 uc LGO can be attributed to a percolation scenario caused by finite roughness, the in-gap intensity of 2 uc NGO with slightly lower amplitude may be a result of uncertainties in the normalization procedure, of surface roughness, of a slightly higher defect concentration or of photoinduced charges discussed later in section 3.5. Similar to LAO/STO, the defect related G2 shoulder shifts to lower binding energy than in STO.

In conclusion, one can see that the appearance and relative intensity of in-gap states measured under resonance conditions at the Ti L-edge is consistent with the Ti^{3+} shoulder of the Ti $2p$ core level measured by XPS, although quantitative values could be extracted only for the XPS data. Both measurements are fundamentally different but very similar in the obtained conclusions. This underlines the reliability of the measurements, data analysis and results for both sections.
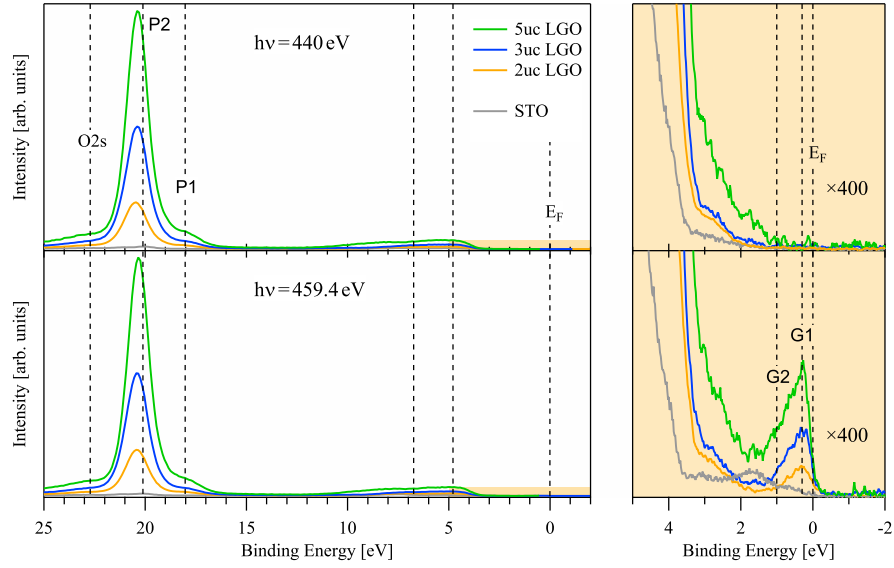
Figure 3.28: Off- and on-resonant valence band spectra and shallow core levels of STO in direct comparison to 2, 3 and 5 uc LGO/STO. The region around E_F (yellow background) is magnified in the right part by a factor of 400.
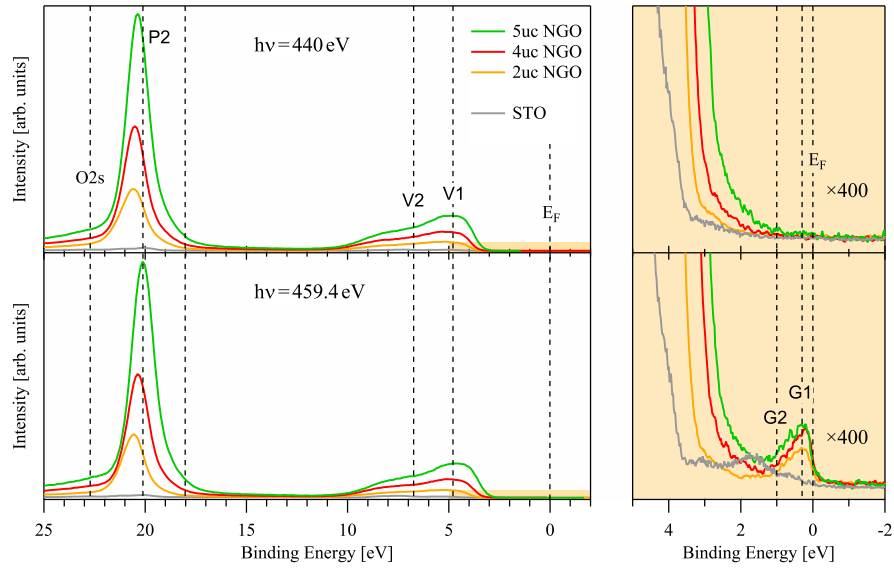

Figure 3.29: Off- and on-resonant valence band spectra and shallow core levels of STO in direct comparison to 2, 4 and 5 uc NGO/STO. The region around E_F (yellow background) is magnified in the right part by a factor of 400.

Shape and absolute intensity of the in-gap states

Finally, the in-gap states of the three different polar/non-polar heterostructures above critical thickness are compared regarding their absolute intensities and their shapes. In

Fig. 3.30(a) the ResPES spectra in the vicinity of E_{F} are presented for the 5 uc LAO/STO, LGO/STO and NGO/STO samples, for the 6 uc LAO/STO sample, and for STO. As mentioned above, the spectra are corrected for the overlayer damping in the upper part of the figure to directly reveal absolute intensities, whereas in the lower part the spectra are normalized to compare the shape of the in-gap excitations for different overlayer materials. The shapes of the in-gap states match very well for the three heterostructures with $n = 5$ uc, but 5 uc NGO/STO exhibits a factor of 2 lower intensity compared to 5 uc LAO/STO and LGO/STO, which have approximately the same amplitude. This is consistent with the Ti^{3+} shoulder in the $Ti\,2p$ XPS measurements, shown on page 62. Both, ResPES and XPS, reflect the charge carrier concentration, which is a bit lower in NGO/STO. The same shape of the in-gap states indicates a similar nature of the localized and delocalized electronic states irrespective of the grown overlayer material. Evidently, resonant excitations in STO arise at higher binding energy (1.8 eV) than the G2 feature in the heterostructures. They were attributed to localized $Ti\,3d$ states in proximity to oxygen vacancies [17, 145, 155]. Probably, the well oxidizing conditions during the growth of the presented samples cause a change in the defect configuration and therefore a shift in energy. At this point, the alternative explanation for G2, as a result of incoherently screened decay channels, has to be mentioned [145]. Such a scenario was excluded above for bare STO and insulating LAO/STO heterostructures because of the absence of feature G1. Apriori, this exclusion is not possible for n-doped STO or conducting interfaces, where locally screened states of the filled conduction band can occur due to electronic correlations.
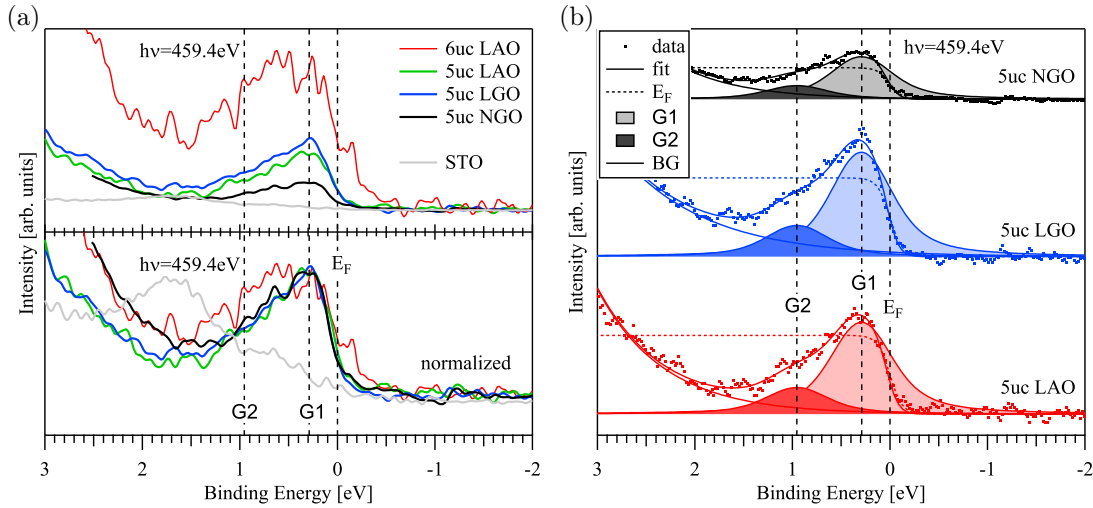

Figure 3.30: In-gap excitations close to E_{F} for STO, 5 uc NGO/STO, 5 uc LGO/STO as well as for 5 uc and 6 uc LAO/STO taken at $h\nu = 459.4$ eV: (a) direct comparison of absolute intensities (top) and shapes (bottom), (b) fit of the G1 and G2 feature for all heterostructures with $n = 5$ uc. An empirical background BG and the intensity cutoff caused by the Fermi function are considered for the fit.

The amplitude and shape of the in-gap states for 6 uc LAO/STO are quite different from the other samples and should therefore be discussed separately. On the one hand the excitations close to E_{F} are considerably broadened and G2 is shifted to higher binding energy. On the other hand, their intensity is higher, which is consistent with the Ti $2p$ XPS data. This heterostructure stems from another batch of samples and was measured during another synchrotron beamtime. Slight differences in growth conditions or in experimental configurations might cause these deviations. Because of this, only in-gap states of 5 uc thick samples were discussed in detail. Fig. 3.30(b) presents a fit of the features G2 and G1 after the subtraction of a smooth, exponential background. The G1 peak was multiplied by a Fermi function to account for its metallic nature. To obtain reliable parameters a global fitting scheme was adopted. All spectra (3 samples × 8 photon energies) were fitted globally with the same parameters:

- equal energy position of G1 and G2,

- same FWHM,

- identical width for the Fermi function, which cuts peak G1.

The exponential background (BG) and the intensity of both in-gap features were varied for the fit. The results are shown in Fig. 3.30(b) for a photon energy of 459.4 eV. The model describes the data of the three materials very well. As mentioned before, G1 is centered at about 0.3 eV and is clearly cut by the Fermi function. The intensity ratio between G2, located at about 1 eV, and G1 is also similar for the three materials. Furthermore, from the fit the constant initial state spectra (CIS) can be extracted, which is the intensity of the in-gap states depending on photon energy, see Fig. 3.31. The CIS spectra are also very similar in shape independent of the overlayer material and track rather the Ti^{3+} XAS spectrum than that of Ti^{4+}. Again, this graph elucidates the equal amplitudes of feature G1 for LAO/STO and LGO/STO and its reduced intensity for NGO/STO for all measured photon energies.

In-gap states and CIS spectra were discussed for LAO/STO heterostructures frequently [17, 142, 148, 149]. Almost all studies comply with the number of identified in-gap states, with their spectroscopic shape and with the interpretation of their metallic or localized nature. Berner *et al.* were further able to measure the angle dependence, dispersion of G1 by angle resolved photoemission spectroscopy (ARPES), and could assign the features in the Fermi surface map to heavy Ti $d_{\mathrm{xz/yz}}$ and light Ti d_{xy} bands. The measured band-structure in comparison to first principle calculation provides even more information on the physical properties of the charge carriers, i.e. character, effective mass, concentration. Unfortunately, soft X-ray ARPES suffer from a much worse energy resolution compared to conventional ultraviolet ARPES, but is necessary for adopting resonance conditions
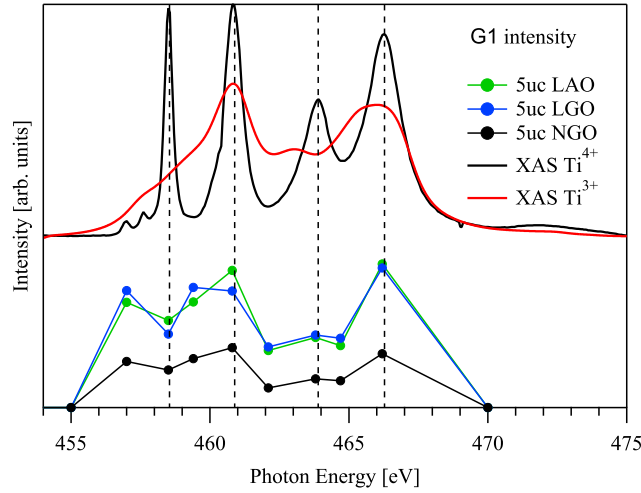
Figure 3.31: Integrated intensity of G1 vs. photon energy (CIS mode) for the three different polar/non-polar heterostructures with $n = 5\,\mathrm{uc}$. The CIS spectra are compared to the Ti^{3+} and Ti^{4+} absorption curves.

to visualize electrons from the buried interface. Thus, it is impossible to observe the quantum well states expected for electrons from Ti atoms at different distances to the interface, and it is even hard to distinguish the weak and heavy bands in the smeared out ARPES maps [148, 149, 156]. In contrast, the dispersion of the 2DEG formed at the bare surface of STO can be mapped well by ultraviolet ARPES [157–160]. This system is closely linked to the physics at the buried interfaces. In fact, the formation of oxygen vacancies triggered by vacuum annealing and light illumination turned out to be the carrier source for the 2DEG at the STO surface, which are affected by buckling and rotations of the oxygen octahedron. Their spectroscopic signs are quite similar to that of LAO/STO. The strongly dispersing parabola of the light Ti $3d_{\mathrm{xy}}$ band and their quantum well states have been well resolved for STO. These electron pockets are centered at the Γ point and extend up to $0.3\,\mathrm{eV}$ in energy, which is equal to the energy position of feature G1 in LAO/STO reported here and elsewhere [142, 149]. Also the circular and elliptical features of the Fermi surface could be reproduced in both systems, STO [156, 157] and LAO/STO [148], as well as the localized in-gap states at around 1–$1.5\,\mathrm{eV}$ denoted with G2 here [142, 158, 160]. The CIS spectra, the intensity of the in-gap states vs. photon energy, can give additional insights into their character. Berner *et al.* reported different CIS spectra for G1 and G2. Whereas G1 resonates over a relative wide photon energy range in their study, G2 matches rather the Ti^{3+} XAS spectra [148]. My thesis reveals by contrast that both features are closely linked to each other and have an equal, Ti^{3+}-like CIS shape. However, G2 is located at lower binding energy compared to the measurement of Berner *et al.*. This could be due to the well oxidizing conditions during

growth or the superposition of the localized in-gap states by the background (leading edge of the valence band V1). In the latter case, the feature G2 might belong rather to the incoherently screened decay channel, whose intensity is expected to follow those of G1. In contrast to the observed Ti^{3+}-like CIS spectra, the intensity of G1 measured by Cancellieri *et al.* is confined to a photon energy region close to the Ti^{3+} absorption maximum [149]. A similar behavior as shown here in Fig. 3.31 was found by Drera *et al.* [142].

Overall, one can conclude that sample history and growth conditions might influence the CIS spectra. However, the equal amplitude, shape and CIS spectrum of the in-gap states for LAO, LGO and NGO grown on STO reveal that the three interfaces exhibit a very similar electronic structure, which originates from that of doped STO predominantly. It was hypothesized that delocalized, metallic G1 and localized G2 states can be associated with superconductivity and ferromagnetism, respectively [148].

Temperature dependence and ResPES at the O *K*-edge
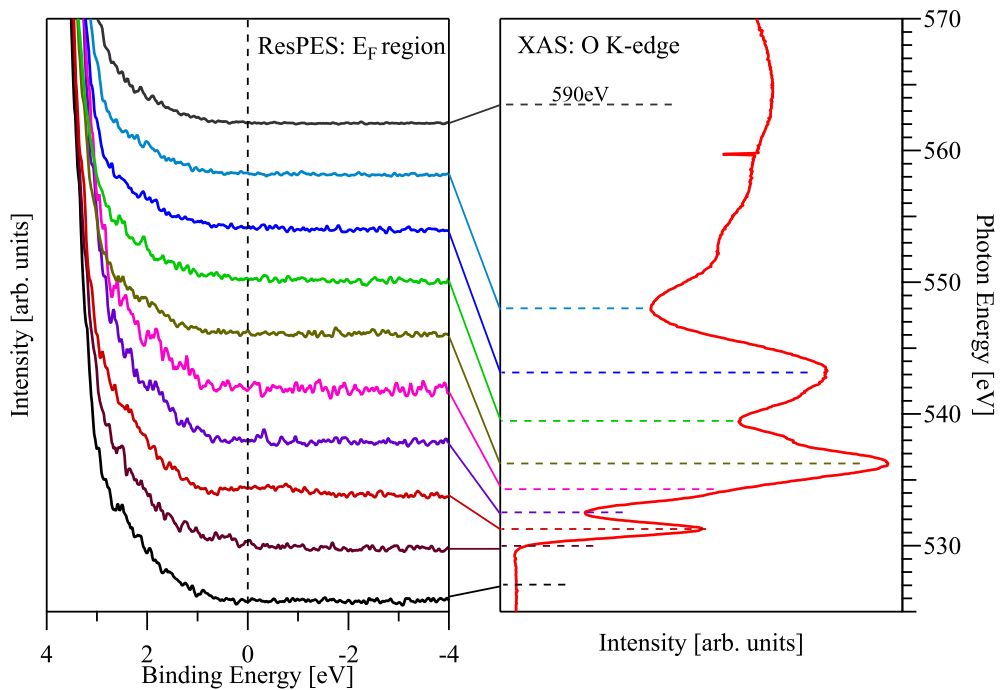

Figure 3.32: Resonant photoemission spectra in vicinity to E_F (left), which were measured at designated photon energies around the O *K* absorption edge (right part). No in-gap states have been found.

So far, the presented measurements were carried out at room temperature and with photon energies around the Ti *L*-edge. Additional effort has been expended to detect in-gap

states by the means of ResPES at the oxygen absorption edge (O K-edge). Hybridization between the O $2p$ valence band and Ti $3d$ states was already proven by the resonating features V1, V2, S1 and S2. In analogous manner, Ti $3d$ related in-gap states should resonate while crossing the photon energy above the O K-edge. A comparison of in-gap states measured at the O K-edge to these measured at the Ti L-edge under consideration of theoretical calculations might provide access to underlying hybridization parameters like the hybridization strength. Despite various measurements, no in-gap excitations have been found at designated photon energies at the O K-edge, see Fig. 3.32. So far, no in-gap states resonating at the O K-edge have been reported for LAO/STO, although they are present in bare STO [145]. Their intensity could be below the detection limit, since the intensity of the Ti $3d$ in-gap states measured at the Ti L-edge is already low and is expected to be still lower at the oxygen absorption edge. Furthermore, the overlayer and possible adsorbates contain oxygen, too, which probably have different resonance effects superimposing and broadening the valence band region.

Additionally, the corresponding absorption edge measured in total yield mode is also given in Fig. 3.32. The samples have been transported *ex situ*, therefore they have a significant amount of contamination on their surface. Among them are carboxyl groups, which contain oxygen by itself bonded in a much different chemical environment than in perovskites. Their XAS signal superimposes the signal coming from the LAO, STO and the interface in-between. Previous bulk sensitive electron energy-loss spectra (EELS), measured with a *transmission electron microscope* (TEM) at the O K-edge, could prove valence changes at the LAO/STO interface [105]. A higher amount of oxygen defects for as-grown LAO/STO samples than for post-growth annealed samples was shown by O K-edge absorption measurements of *in situ* samples [161], but an *in situ* transport to the synchrotron without breaking vacuum was not feasible in this work.
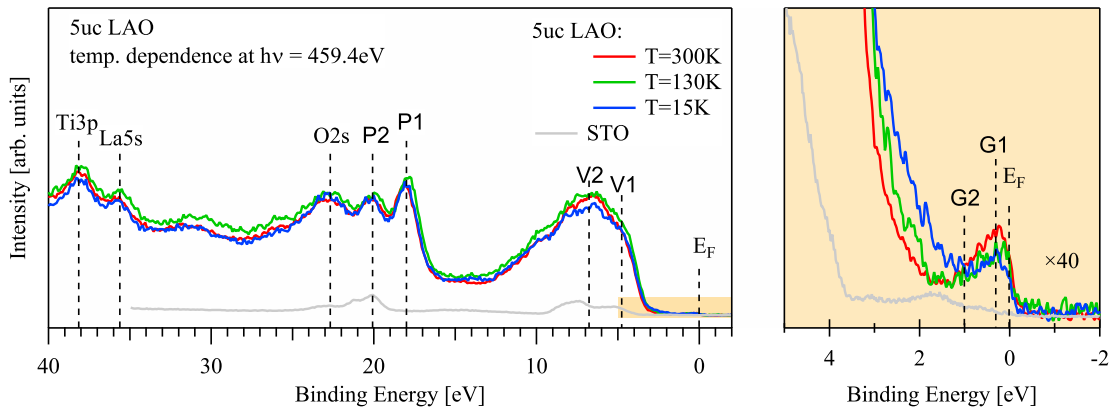
Figure 3.33: Temperature dependency of the in-gap states of a 5 uc LAO/STO sample at a photon energy of $h\nu = 459.4\,\text{eV}$. The region around E_F (yellow background) is magnified in the right part by a factor of 40.

The temperature dependence of resonantly enhanced in-gap states is plotted in Fig. 3.33. The data have been normalized to Ti $3p$ at about $38\,\text{eV}$ binding energy, see extended valence band graph. The E_F region is magnified by a factor of 40. Apparently, spectral weight at E_F is transferred to higher binding energy while cooling the temperature down to $15\,\text{K}$. The `G1` peak shrinks by a factor of about 1.4 and additional intensity rises at about $2\,\text{eV}$, at slightly higher binding energy than for the in-gap states of bare STO caused by oxygen defects. The diminished intensity of metallic states is consistent with the reduction of sheet carrier density upon temperature decrease [21, 115, 162]. The missing electrons seem to be caught by defects probably caused by structural changes upon cooling. Thus, they cannot contribute to metallic transport anymore. At low temperature structural changes and strain can occur in the system. STO is known to undergo a cubic-to-tetragonal phase transition at $110\,\text{K}$ [163, 164], which can also alter the binding energy of the defect states. Additional changes in the valence band cannot be excluded, e.g. a broadening of the whole valence band region by a temperature decrease, but might be able to explain the larger intensity increase at $2\,\text{eV}$ compared to the intensity decrease at E_F.

3.4.3 Band alignment

In the previous section unambiguous Ti $3d$ related charge carriers close to the interface were directly identified for the three polar/non-polar oxide interfaces. But this is not sufficient for a complete description of the electronic properties of these systems. For a comprehensive understanding the knowledge of the energy levels across the heterostructure is necessary. From an experimental point of view, PES is suitable to detect an energy level alignment at interfaces by probing the energy positions of core levels and of the valence band, and their evolution with thickness. Furthermore, band diagrams can be extracted, which are essential to understand the electronic structure and properties of solids and interfaces in detail, and form the basis of future device optimization.

For polar/non-polar oxide heterostructures this concerns both the energy levels of the STO substrate, where band bending effects may occur [139], and that of the overlayer material, where the band positions may be strongly influenced by the presence of electric fields. Especially the latter is theoretically a large effect predicted by density functional theory and the polar catastrophe scenario. The electrostatic potential built-in in the polar overlayer increases by $0.9\,\text{eV}$ per unit cell and shifts the overlayer valence band above the chemical potential [93], which should be easily observable in a photoemission experiment. It leads to a variation of the energy position of all core levels and the valence band of the overlayer as a function of layer number and to a significant line broadening because the

photoemission signal picks up contributions from several layers. However, none of these effects have been observed in a number of previous experiments on LAO/STO, which poses a serious obstacle for the polar catastrophe model in its original form [82–84, 99, 134]. On the other hand, core level shifts of the right sign but an order of magnitude smaller than expected have been observed and rationalized by the creation of oxygen vacancies at the surface of the overlayer and subsequent charge transfer to the interface which balances internal fields [82, 134].

Core level shifts
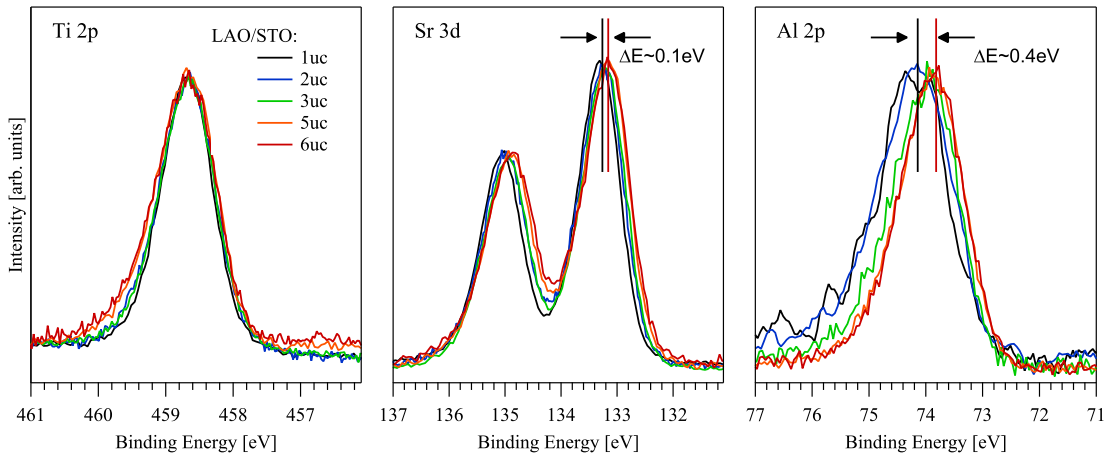
Figure 3.34: Ti $2p$, Sr $3d$ and Al $2p$ core levels from LAO/STO samples with varying thickness aligned to the same Ti $2p$ peak position. The Al $2p$ peak shifts to about $0.4\,\mathrm{eV}$ lower energies for increasing layer number, whereas the Sr $3d$ line stays almost constant.

Fig. 3.34 presents a compilation of LAO/STO Ti $2p$, Sr $3d$ and Al $2p$ core levels as a function of layer number. A notorious practical problem for photoemission experiments of insulating or poorly conducting samples is charging, which may cause energy shifts and deteriorate the binding energy scale in an absolute sense. Here, this problem is circumvented by considering energy differences between certain core levels, which are still reliable even under the presence of moderate charging. Therefore, all spectra in Fig. 3.34 are aligned to the Ti $2p$ position. Ti and Sr belong to the STO substrate, Al belongs to the LAO overlayer. Marginal energy shifts are present for Sr $3d$, whereas a clear shift of the Al $2p$ energy position with increasing layer number towards *lower* values is observed. It amounts to about $0.4\,\mathrm{eV}$ for the 6 uc sample relative to 1 uc. For an accurate analysis the energy positions of the core levels have been determined by standard fitting procedures using Voigt-profiles. Fig. 3.36 summarizes the core level shifts, i.e. the change in energy differences, for LAO/STO, LGO/STO and NGO/STO.

For LGO/STO and NGO/STO the Ti $2p$ - Ga $2p$ separation has been considered. If the STO energy levels including Ti $2p$ were indeed fixed, the LAO upward shift is in agreement with the polar catastrophe, but much smaller: the observed shift would not be enough to bridge the optical gap of STO (3.2 eV). Additionally, one would expect an energy drop at 4 uc if electronic reconstruction sets in, but this is also absent in the data. However, it is also possible that the LAO levels are actually fixed and the STO levels successively shift to higher energy with increasing layer number, which would correspond to a band bending on the STO side of the interface. To discriminate these possibilities either absolute binding energy shifts must be considered, which are not available here, or the dependence of the peak width on layer number, an approach that will be pursued further below.

Valence band shifts

Such shifts naturally appear also for the valence bands, in which they change the relative positions of the valence band onsets of STO and the overlayer. The valence band onset can be easily determined by valence band PES. It is equal to the intersection between the linear extrapolation of the valence band's leading edge and a line at zero intensity, and can be understood as energy gap between valence band maximum and the Fermi energy. The *valence band offset* (VBO), which is by itself an important electronic parameter, is defined as the jump in energy of the valence band at the interface. The Anderson's rule asserts that the vacuum levels of two semiconductors forming an interface should be aligned at the same energy. Then, the VBO can be calculated if the bandgap and electron affinity of both materials are known. Experimentally, the VBO can be inferred directly by PES from a fitting procedure using the valence bands of pure LAO and STO as fitting entities and letting their relative position and amplitude vary. VBOs have been extracted in this way before [81, 103, 148]. Another possibility is to reference the core level energies of the heterostructure to the ones of the constituent materials [14, 81, 103, 148]. Qiao *et al.* reported a VBO value of 0.16 ± 0.10 eV for a 3 uc LAO/STO sample [103], Berner *et al.* $0.3 - 0.4$ eV for 4 uc [148]. The positive sign corresponds to the situation that the LAO valence band maximum is closer to E_F than those of STO. Chambers *et al.* showed a certain sample and sample treatment dependence of the obtained VBOs [14]. A constant VBO as a function of layer number was derived by Berner *et al.* but data are only available for $n \geq 3$ uc. As mentioned above, a shift of the core levels (as seen in Fig. 3.34) must also entail a change of the VBO. Here, a method is introduced to make these shifts visible without relying on bulk STO or LAO reference samples and possible complications due to their surface properties being different from the heterojunction.
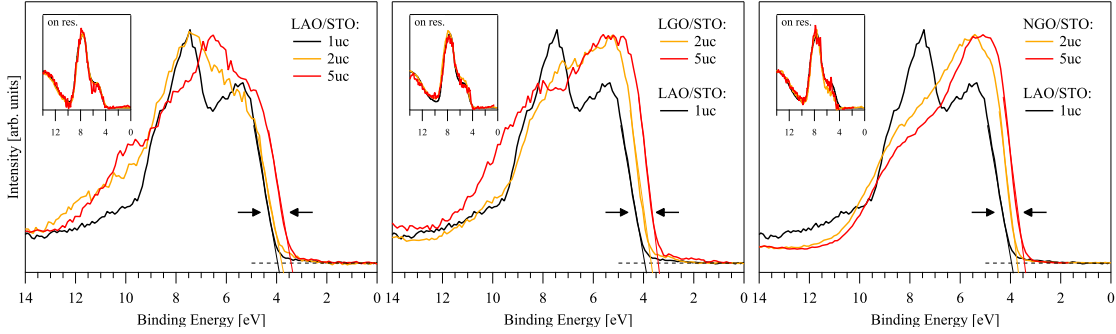
Figure 3.35: Valence band comparison for LAO/STO, LGO/STO and NGO/STO heterostructures with varying thickness. The energy alignment is carried out using the Ti L_3 resonance enhancement (see insets). The shift of the leading edge for different layer numbers corresponds to changes of the valence band offset (see text for details).

The main idea is that the valence band spectra of samples with different layer numbers can be aligned to each other using the Ti $3d$ related resonance enhancement of the main valence band. ("Enhancement" means the difference between on- and off-resonant spectrum.) The insets of Fig. 3.35 show the resonance enhancement at the Ti L_3-edge of the 1 uc LAO and of thicker LAO, LGO and NGO samples. The shape is, as expected, very similar and can be used to align the related off-resonant valence bands precisely. The normalized and aligned valence bands measured off-resonant with 440 eV photon energy are shown in Fig. 3.35. In comparison to the 1 uc LAO sample, one observes a shift of the leading edge for the 2 uc and 5 uc thick samples irrespective of the overlayer material. This can only arise from the overlayer part shifting to lower energies compared to the STO part, which is fixed by the alignment. The values of the energy shifts have been derived by fitting the leading edge to a line and determining its crossing with the energy axes, as shown in the respective graphs of Fig. 3.35. The results are summarized together with the core level shifts in Fig. 3.36. The correspondence between VB and core level analysis is satisfactory, although they come from independent measurements (synchrotron vs. laboratory), which puts further confidence into the results. Fig. 3.36 clearly shows that the VBO increases with increasing layer number.

The energy shifts in Fig. 3.36 are referenced to the 1 uc (LAO/STO) or 2 uc (LGO/STO, NGO/STO) samples, respectively. Due to the absence of overlayer core levels in bare STO the core level shift is set to the VBO value for the thinnest measured sample. The full energy shift in the $n \to 0$ limit, and hence absolute values of the VBO, can be either obtained by extrapolation or by comparison to bare STO. Contrary to the situation described above a free STO surface is involved in the latter. Nevertheless, reliable results can be obtained, although with moderately increased error bars. Apparently, similar core level shifts and similar VBOs in the order of 0.4 eV for all the heterostructures have
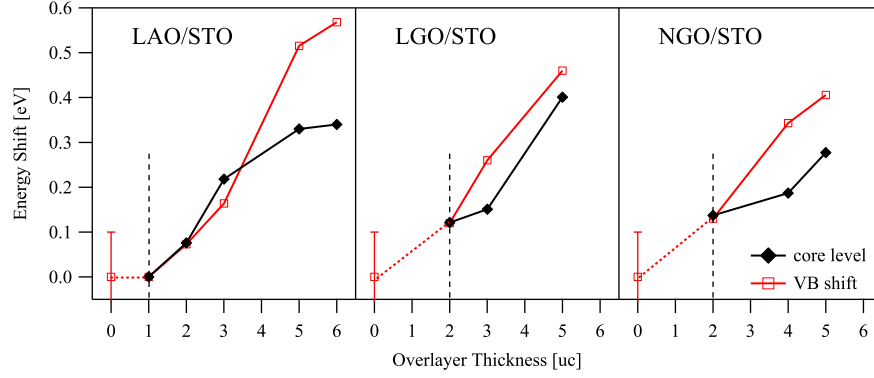
Figure 3.36: Energy shifts obtained from core level and valence band evaluation. The dashed vertical line highlights the reference sample thickness. An overlayer thickness of $n = 0$ uc corresponds to the STO substrate. This data point is given with increased error bars (see text)

been observed. This underlines that a universal mechanism driving the metal insulator transition is at work. The observation of the absence of large energy shifts or giant line broadening is in full agreement with previous studies. The remaining thickness dependent energy shifts are consistent with Refs. [82, 134] both concerning their sign, magnitude ($\Delta E = 0.4$ eV) but also methodologically as they have been obtained by considering energy separations rather than absolute binding energies. Berner *et al.* also found $\Delta E = 0.3 - 0.4$ eV but only for samples with $n \geq 4$ uc, which have little residual thickness dependence [84]. Other studies report VBOs within the same order of magnitude ($\Delta E \leq 0.7$ eV) [14, 81, 83, 103]. Note that details of the sample and surface preparation could play a role as always for the interface properties of oxide heterostructures.

Band bending vs. built-in potential

Let's return to the question raised above whether the observed energy level shift originates at the STO or overlayer side of the heterostructure. A band bending or continuous energy increase due to internal fields would inevitably increase the line-width. In fact, such a broadening is observed in Fig. 3.34 on the high binding energy side of the Ti $2p$ line, whereas it is absent for Al $2p$. The FWHM of these core levels, as well as Sr $3d_{5/2}$, La $3d_{5/2}$ and Ga $2p_{3/2}$ have been evaluated by standard fitting procedures. Fig. 3.37 summarizes all these results divided into STO (a) and overlayer lines (b) respectively and shifted vertically to the same offset in order to enable convenient comparison. The result is very clear: the STO levels show a monotonous increase with increasing thickness, whereas at best a decrease is observable for the overlayer. The latter might be attributed to increasing crystalline quality of the film with increasing layer thickness and the increasing
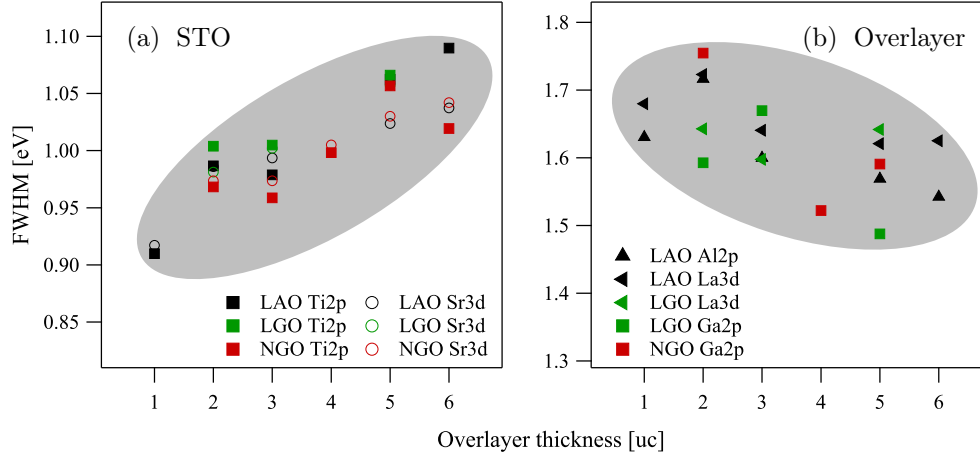
Figure 3.37: Full width half maximum (FWHM) of the specified core levels as a function of layer number. (a) For STO related lines: The energy axis refers to the FWHM of Ti $2p_{3/2}$. The FWHM of Sr $3d_{5/2}$ is shown with an offset of $0.05\,\mathrm{eV}$ to enable convenient comparison. (b) For overlayer related lines: The energy axis refers to Ga $2p_{3/2}$, the offsets for Al $2p$ is $0.2\,\mathrm{eV}$ and for La$3d_{5/2}$ -0.35 eV. The gray contours are guides to the eye.

number of atoms in a true bulk environment. The former must be related to increasing band bending near the interface as the layer number increases. This is in agreement with the small core level shift between Ti $2p$ and Sr $3d$, shown in Fig. 3.34. Ti is located closer to the interface than Sr, due to the TiO_2-termination procedure. Ti experiences therefore a higher averaged band bending, which shifts Ti related states to higher binding energy. Also the broadening of the Ti $2p$ level is a bit larger than those of Sr $3d$. Ti core level shifts of similar amplitude were reported by Drera *et al.* [81]. Band bending has been suggested earlier based on binding energy shifts of the Ti $2p$ line [142]. However, other studies found no or small variations of the peak width [14, 82]. Note, that we observe narrow line widths for the samples with thin overlayers, narrower than previously reported, and this enables the observation of the increase for thicker samples. It is also noteworthy that all three compounds fall on the same trend in Fig. 3.37. The valence band offset without the band bending can be estimated from the energy shift in the limit of $n = 0$ and appears to be close to zero with some uncertainty (in the order of ± 0.15 eV).

The quantitative information upon the electronic structure obtained above can be used to construct the band diagrams for the heterostructures, shown in Fig. 3.38. An important ingredient is the absence of strong electric fields at the overlayer side, confirming previous results. The band bending at the STO side is given with $0.4\,\mathrm{eV}$ here (extracted from Fig. 3.35) but could be somewhat larger directly at the interface due to the integration over several unit cells in the measurements. From the depth sensitive measurements in the previous sections the vertical extension of this region is estimated $\geq 2\,\mathrm{nm}$, i.e. about

the thickness of the 5 uc overlayer. The genuine VBO between STO and the overlayer is estimated near zero but with some uncertainty. The optical gaps between the different overlayers vary considerably, leading to different conduction band offsets. However, the other relevant electronic parameters appear to be universal leading to similar transport properties of the heterostructures. A previous band diagram for LAO/STO derived on the basis of photoemission data gives a lower band bending and a VBO of $\sim -0.35\,\text{eV}$ [84]. The difference lays mainly in the inclusion of 1 uc - 3 uc samples in the present study, which clearly shows changing energy shifts. This is possible because charging related uncertainties could be minimized by relying rather fully on energy separationsthan on absolute binding energies.
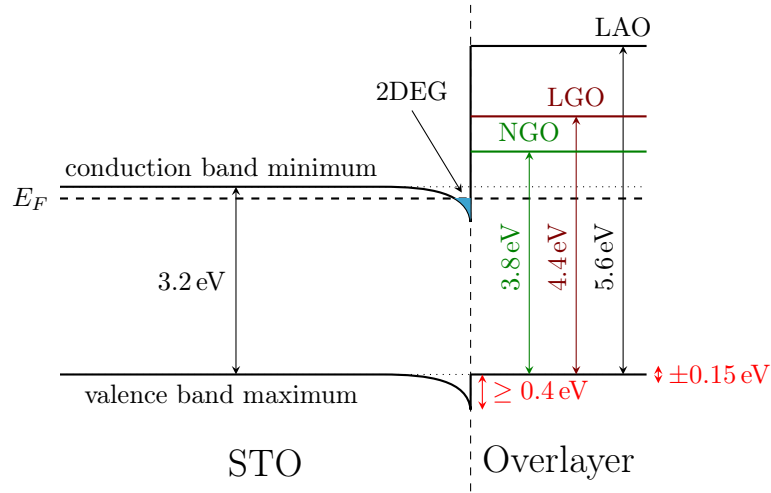
Figure 3.38: Universal band diagram of polar/non-polar oxide heterostructures derived on the basis of the determined core level shifts and valence band offsets. The data have been interpreted in this way that no electric field exists in the polar overlayer, but band bending of at least 0.4 eV occurs at the STO side. The valence band offset without considering the band bending is close to zero ($\pm 0.15\,\text{eV}$).

The absence of observable consequences of electric fields in the overlayer in PES reported earlier and confirmed here has been interpreted in two ways:

- by the creation of oxygen vacancies and subsequent charge transfer to the interface which balances internal fields [82, 84, 134],

- by photoinduced flattening of the internal potential [21, 148].

In the latter scenario, which is described in detail in the following discussion (Fig. 3.41), electron-hole pairs are formed by the photon illumination and become separated by the large field inside the polar overlayer, with little probability to recombine. The accumulation of charges of different signs on the interface and surface respectively compensates the internal field when equilibrium is reached. Both scenarios are fundamentally differ-

ent. In particular, in the photoinduced flattening scenario the internal fields are actually present but suppressed by the experimental technique used here. In another study employing a different technique (electron microscopy), but very similar samples, signatures of a permanent polarization in the overlayer have been found, consistent with the expected polar fields [105]. By contrast, no photon flux dependence of the photoemission results has been seen here and elsewhere [82, 148]. Moreover, the observed charge concentration and profile agrees with transport measurements, which is difficult to reconcile with pure photodoping. A clarification of this important point calls for further investigations, possibly taking into account photoeffects inside the STO and more involved defect chemistry.

3.5 Discussion

Various findings concerning the complexity of polar/non-polar oxide heterostructures grown along (001)-direction have been presented and discussed in the three previous chapters. It is the objective of this chapter to summarize the results of the present thesis and relate them to the body of existing knowledge about polar/non-polar oxide interfaces. Apparently, it is challenging or impossible to consider all aspects from literature including this thesis and merge them to a general description of the various intriguing properties, because the reported results depend subtly on growth conditions and are not always consistent. The oxygen partial pressure during growth and during a possible post-growth annealing step has a strong influence on the electronic properties of all oxide heterostructures. For LAO/STO this was summarized by Huijben *et al.* in a phase diagram presented in Fig. 3.39 [68]. Large carrier mobilities were reported initially by Ohtomo and Hwang, but in fact rest on 3D metallicity of the doped STO substrate in presence of oxygen vacancies [10, 12, 161, 165]. A number of experiments reveal that an interfacial 2DEG is only formed if oxygen vacancies are carefully avoided. In the present thesis only *well oxidized samples* have been investigated, which diminishes extrinsic doping effects of oxygen vacancies. It is assumed that an electronic reconstruction caused by the polar catastrophe scenario drives the intrinsic properties of the LAO/STO interface, i.e. the insulator-metal phase transition at a critical thickness of 4 uc [11, 166]. This scenario may apply to any polar overlayer material grown on any non-polar substrate with some restrictions:

- a small lattice mismatch between both materials to enable an epitaxial 2D growth,

- a larger bandgap for the polar overlayer material,

- favorable interface states to enforce an electronic reconstruction rather than structural or chemical modifications.

Usually, atomic rearrangements occur at conventional group III–V semiconductor interfaces due to the latter fact [108]. In contrast to this, interfaces of multivalent transition metals incorporated in a robust oxide matrix may favor the electronic reconstruction. Based on this novel effect intriguing properties can occur which are additionally promoted by electronic correlations.
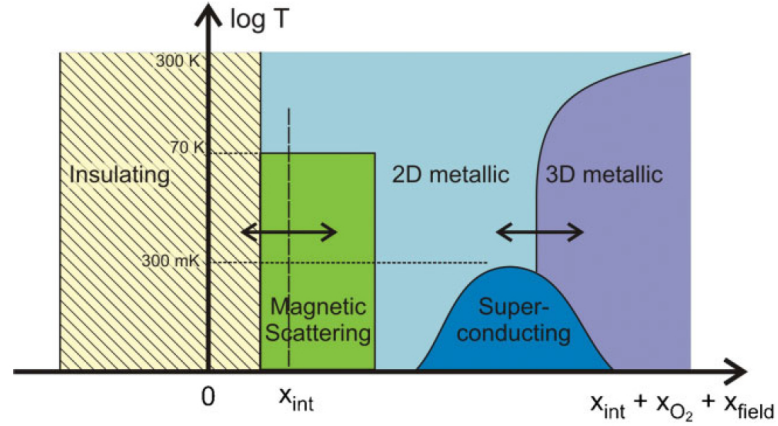
Figure 3.39: Doping versus temperature phase diagram of LAO/STO interfaces, taken from [68]. Three possible doping contributions are considered: intrinsic carrier doping from the electronic reconstruction (x_{int}), carrier doping from oxygen vacancies (x_{O_2}) and carrier doping by applied electric fields (x_{field}). Observed transport effects are insulation at p-type interfaces ($x < 0$) [10], 2D interface metallicity, 3D bulk metallicity [10, 167], negative magneto resistance below 70 K [19], magnetic hysteresis below 300 mK [19], and superconductivity below $T_c = 200$ mK [70].

Up to now, the formation of a 2DEG at the interface of polar/non-polar oxide heterostructures is restricted to STO as substrate material. Reasons for that might be its availability in high crystalline quality and of a reliable single-termination procedure, the possibility for donor-doping, its high dielectric constant as well as the transition element Ti whose valence can be easily reduced in STO. However, the interface between a number of other polar overlayer materials and STO yield properties similar to LAO/STO, but are not well characterized by spectroscopy which can elucidate the origin and properties of the interfacial charge carriers. My thesis adds insights from a comprehensive X-ray spectroscopy study on NGO/STO and LGO/STO heterostructures in comparison to LAO/STO in order to distinguish general from material specific properties.

The Ti $2p$ X-ray photoemission and X-ray absorption spectra presented in section 3.4.1 in addition to the valence band spectra, taken at Ti resonance conditions (ResPES), of section 3.4.2 unambiguously reveal the Ti $3d$ character of the 2DEG. Ti^{3+} features for the three investigated polar overlayer materials, in particular a low binding energy component in Ti $2p$ XPS and Ti $3d^1$ excitations in vicinity to E_F resonantly enhanced for photon energies at the Ti L-edge, appear for LAO/STO with $n \geq 3$ uc which is in good agreement

to the critical thickness of 4 uc for the insulator to metal phase transition. XPS and XAS prove the existence of Ti^{3+} but cannot distinguish between localized and itinerant states, however the ResPES features cut by a Fermi-function are a direct evidence of their metallic nature. The small Ti^{3+} signatures for the 3 uc sample can be understood by finite roughness and a percolation scenario for the electronic reconstruction. In contrast to this LGO/STO and NGO/STO show a steady increase of Ti^{3+} up to 5 uc thickness, whereas NGO/STO seems to have a slightly lower charge carrier concentration. Both heterostructures show a bit larger interface roughness concerning crystallinity, defects and intermixing than LAO/STO [125], which is probably responsible for the observed Ti^{3+} intensity below 4 uc. Additionally, photoconductivity induced by the measurement technique itself (X-rays illumination) might play a role and is discussed in detail in the following section. However, the three different techniques, used here, show consistent results underlining their reliability. The estimated amount of charge carriers is in the order of $10^{14}\,cm^{-2}$, which is in the range of values extracted by transport measurements on samples grown in the same laboratory [21]. By tuning the surface sensitivity of the XPS and XAS measurements only marginal changes of the relative Ti^{3+} signal were found indicating a constant charge carrier concentration within the sensitivity depth of about 2–4 nm. Small sample dependent variations were shown and addressed to slightly different growth conditions or to sample history, since the samples were *ex situ* transported. Hints for deviations from an abrupt interface were discussed in section 3.3 and are present for the three investigated oxide heterostructures. It was argued that the Sr segregating at the surface stems from an initial Sr-overstoichiometry or residual Sr atoms at step edges of the substrate. The Sr diffuse towards the surface during growth and force a thermodynamically favored epitaxial growth with TiO_2-LaO stacking. However, possible doping of the interface by Sr vacancies or by substitution with La as well as modified electrostatics across the overlayer due to polar SrO molecules at the surface cannot be ruled out.

The observed core level and valence band shifts relative to STO contributions have been used to derive a band diagram of the heterostructures. The data show that band bending occurs at the topmost STO layers which is in agreement with the observed occupation of Ti^{3+} states. The bottom of the former empty conduction band of STO, consisting of mainly Ti $3d$ density of states [152], is bent below E_F and hosts the electrons at the interface. The amount of band bending (0.4 eV) coincides with the energy position of the Ti $3d^1$ states in ResPES, also seen in other studies [17, 142, 148, 149]. In a recent work of Drera *et al.* a similar approach was applied to extract the band diagram of 5 uc LAO/STO yielding equal qualitative conclusions but with a slightly larger band bending in STO [168]. They reconciled the shape of the relatively broad ResPES features at E_F with the band bending. Besides the already discussed broadening due to oxygen defect

states or incoherently screened decay channels, they claim that the broadening is caused by the superposition of Ti $3d^1$ signal coming from different distances to the interface and energetically shifted by the band bending. This seems plausible for the excitation in close vicinity to E_F labeled here with G1, but the band bending is not large enough to explain peak G2 at about 1 eV binding energy.
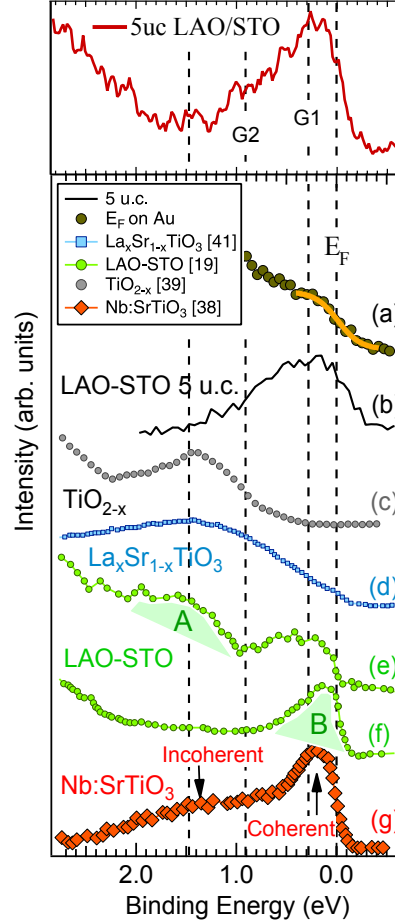
Figure 3.40: Compilation of the Ti $3d$ in-gap states measured by ResPES in various publications, adapted from [168]. The spectrum of the 5 uc LAO/STO sample, measured in this work, is included (top, red spectrum) representatively. The references given in the graph are referred to the original paper ([168]) and can be found here in Refs. [145] (g), [148] (e, f), [169] (d), [170] (c), [168] (a,b).

Drera *et al.* compared also the ResPES in-gap states of various material systems containing TiO_x from different publications [168]. This is shown in Fig. 3.40 including the spectrum of a 5 uc LAO/STO sample representative for the results of my thesis. The dashed lines are guides to the eye and refer to the energy positions of E_F, of the in-gap features G1 and G2, and of excitations occuring at about 1.5 eV far from E_F. At first glance, all LAO/STO spectra have a similar shape with a rather broad and asymmetric

excitation at E_F, except feature A at 1.5 eV (e) found by Berner *et al.* [148]. Since this sample was grown under relative low oxygen partial pressure, peak A is associated with oxygen defect states and is absent in samples grown under higher oxygen partial pressure, i.e. presented by Drera *et al.* (b) and in this thesis (top, red spectrum). This underlines the high quality of the investigated samples having minor defects. It is noteworthy that the oxygen deficient rutile spectrum (TiO_{2-x})(c) and the $La_xSr_{1-x}O_3$ spectrum (d) are considerable different from the LAO/STO and Nb-doped STO spectra [168]. They show no clear excitation at E_F but a rather broad peak at higher binding energy indicating the localized nature of the Ti $3d^1$ electrons. As consequence, one can rule out that finite Sr-La intermixing or oxygen vacancies are the major dopants of the LAO/STO, NGO/STO and LGO/STO heterostructures, examined here. Finally, the incoherent emission of Nb-doped STO (g) is rather broad and distinct from the coherent emission at E_F. In contrast to this, the features G1 and G2 in LAO/STO are not as well separated from each other and have a different line shape. This may exclude the presence of incoherent decay channels as in Nb-doped STO. From my point of view the asymmetric and broad excitations in vicinity to E_F can be most likely associated with band bending in STO and to a changed defect configuration due to the higher oxygen partial pressure during growth.

Photodoping by light illumination

The band bending at the STO side of the interface is in accordance with the formation of the 2DEG, whereas the driving force for the electronic reconstruction at polar/non-polar oxide heterostructures stays elusive in photoemission experiments, i.e. no rising electrostatic potential up to 3 uc overlayer thickness was observed here and in a large number of previous studies [14, 81, 82, 84, 139, 168]. In principle, the increasing potential should broaden and shift all overlayer core levels as well as the valence band to lower binding energies, but much smaller shifts than expected in the polar catastrophe scenario were reported and related to band bending in STO. Several observations comply with a scenario of an electronic reconstruction triggered by electric fields, but the missing energy shifts in PES pose a serious obstacle. Possible explanations are localized defect states at the surface serving as electron source [148], structural distortions in the overlayer causing an opposite polarization [105], and photodoping effects. Especially the latter is often mentioned, but not well investigated and possibly underestimated. It is well known that the electronic properties of oxide heterostructures, including the Ti^{3+} intensity, depend on light illumination, especially for intense synchrotron sources [21, 156]. However, light illumination cannot be avoided in a photoemission experiment and possible artifacts must be discussed. Previous studies argued that photodoping is not dominating high
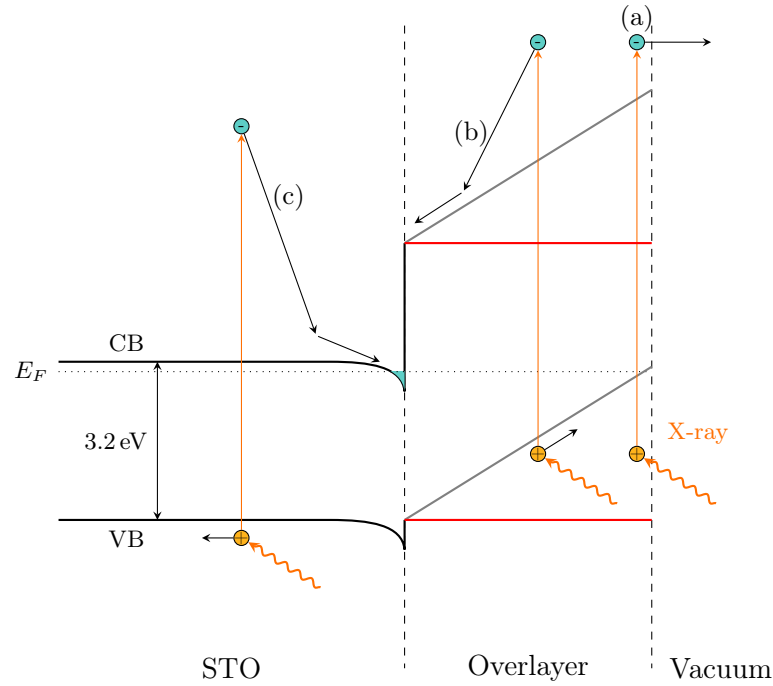
Figure 3.41: Band diagram of polar/non-polar oxide heterostructures. The conduction band minimum (CB) and valence band maximum (VB) in the polar overlayer are expected to increase with thickness until electronic reconstruction takes place (gray line), but might be flattened by light illumination (red). The flattening could be a result of an additional, opposite electric field caused by the spatial separation of photoexcited electron-hole pairs. Electron photoemission leaving behind a hole (a) and separation of the electron-hole pair in the polar overlayer (b) or in the STO substrate (c) can contribute to this effect, due to the accumulation of positive charged holes and negative charged electrons at the surface and interface, respectively.

energy photoemission spectra based on photon intensity variations over three orders of magnitude [84] and quantitative estimations of the photoabsorption [82]. Here, the same conclusion could be drawn, since the Ti^{3+} concentration extracted from laboratory XPS is in qualitative agreement with the synchrotron XAS and ResPES measurements. The effective photon flux per unit area differs by two orders of magnitude in both cases. Nevertheless, a saturation of the photodoping for even lower photon intensities and a possible larger influence on the electrostatic potential in the overlayer cannot be ruled out.

Fig. 3.41 illustrates that during a photoemission experiment electron-hole pairs are generated by the high energetic light and become possibly separated by internal electric fields. Some electrons are emitted away from the sample leaving positive charged holes (Fig. 3.41(a)). In metals the excited charges can relax or recombine fast but in semicon-

ductors and insulators they cause charging or photovoltage effects, due to larger lifetimes [171]. Supported by the band bending in STO (Fig. 3.41(c)) and by the built-in electric field in the overlayer (Fig. 3.41(b)) electrons and holes can accumulate at the interface and surface, respectively. Their electric field is opposite to the polarity of the LAO layers. One would expect an equilibrium between generated and recombined electron-hole pairs canceling the built-in electric field. It was claimed that the spatial separation of electron-hole pairs by the built-in electric field causes the observed persistent photoconductivity even for sub-bandgap photon energies [21, 76]. The effect of these photoinduced charges on the transport properties is smaller for conducting samples in which the electric field is already neutralized. Bare STO also exhibits persistent photoconductivity, which was attributed to the excitation of an electron from a titanium vacancy defect into the conduction band [172]. For $LaCrO_3/SrTiO_3$ interfaces a built-in potential was observed by XPS [173], raising again the question why it is absent in LAO/STO, NGO/STO and LGO/STO. In LAO/STO there is only one direct, experimental evidence for the potential reported in a scanning tunneling microscopy study by Huang *et al.* [174], so far. Further investigations are necessary to get more insights in this crucial question.

It has been shown in the present thesis that the LAO/STO, NGO/STO and LGO/STO interfaces have similar band diagrams as well as similar amplitudes and equal shapes of the Ti^{3+} features, despite of different bandgaps and lattice constants. This strongly indicates a rather universal behavior irrespective of the overlayer. Especially the ResPES results have been discussed in comparison to the 2DEG found at the interface of STO [156, 157]. Various 2DEG properties of polar/non-polar oxide interfaces are similar to those found at the surface of STO or in doped bulk STO, e.g. a superconducting T_c of around $200\,mK$ [70], high mobilities [94] or similar ARPES spectra [148, 157]. This, including the universal behavior of the three different heterostructures investigated here, strengthens the view that most of the intriguing observations are related to strontium titanate. One observes the properties of electron doped STO irrespective of the doping mechanism. For instance donor doping in STO can be reached by the substitution of Ti^{4+} with Nb^{5+}, by annealing in low oxygen atmosphere – creation of oxygen vacancies at the surface penetrating into the bulk, or by the electronic reconstruction induced by a grown polar overlayer. It seems that STO on the one hand has the capability to host a 2DEG and on the other hand it has the capability to exhibit various exciting properties. For possible future applications especially a tunable charge carrier concentration and high mobilities are necessary, available in LAO/STO [10, 77]. Until today, first field-effect devices were fabricated on the basis of LAO/STO [175], but no commercial

application exists. In future, polar/non-polar oxide interfaces could be utilized in sensors, photodetectors, thermoelectrics, and solar cells [176].

4 Electronic and chemical structure of CeMIn$_5$ (M = Co, Rh, Ir) surfaces

In the previous chapter, I have considered the role of d electrons at interfaces, i.e. in an environment of reduced dimensionality. The new phenomena discussed there are driven, in essence, by a change of the valency of the d element (Ti). Valence changes in correlated electron systems in low dimensions are a widespread and important phenomenon especially at surfaces. In this chapter cleaved surfaces of heavy fermion materials are investigated regarding their electronic and chemical properties. Heavy fermion elements / systems are characterized by a subtle interplay of strongly localized f electrons and itinerant conduction electrons, leading to a dramatic increase of the effective mass. Due to the large Coulomb on-site interaction, they belong to the group of strongly correlated electron systems. Classically, the Kondo effect describes how a localized magnetic impurity, incorporated in a metal matrix interacts with the sea of conduction electrons. At low temperatures the magnetic moment of the impurity is screened by a cloud of conduction electrons which acts as large scattering center. The resistivity increases logarithmically with decreasing temperature. In a crystalline heavy fermion material such magnetic impurities, i.e. $4f$ or $5f$ electrons, are arranged in a periodic lattice and can be described with the periodic Anderson impurity model. Below the coherence temperature T^* the f electrons hybridize with the non-f conduction electrons and form flat bands of heavy mass. At high temperatures the hybridization vanishes, the f electrons act as incoherent scatterers and are expelled from the Fermi surface. This causes the anomalous behavior of the conductance, the magnetic susceptibility and the specific heat of heavy fermion materials at low temperatures. In 1979, Steglich *et al.* discovered superconductivity [177] in the heavy fermion compound CeCu$_2$Si$_2$ and proved, contrary to the conclusion drawn at this time, the coexistence of localized magnetic moments and superconductivity in one material. Besides unconventional superconductivity, quantum criticality and non-fermi liquid behavior occur in the phase diagram of the heavy fermion compounds CeMIn$_5$, which attracts the attention of the scientific community.

4.1 Ce*M*In$_5$ compounds

The intermetallic compounds Ce*M*In$_5$ (M = Co, Rh, and Ir) show the above mentioned intriguing properties. One electron in the nearly localized $4f$ level of Ce couples to the sea of conduction electrons and causes heavy-fermion behavior. Ce*M*In$_5$ compounds crystalize in the tetragonal HoCoGa$_5$ structure of alternating CeIn$_3$ and MIn$_2$ layers, shown in Fig. 4.1. Co, Ir and Rh are isovalent but differ in size. Therefore, with decreasing atomic number at the M-site a higher chemical pressure comparing to the parental cubic CeIn$_3$ structure is exerted and tunes the physical properties. In this way, the antiferromagnetic order of CeIn$_3$ (T_{N} = 10 K) and of CeRhIn$_5$ (T_{N} = 3.8 K) are suppressed and superconductivity occurs at remarkably high temperatures of 2.3 K and 0.4 K in CeCoIn$_5$ and CeIrIn$_5$, respectively [24–26]. So far, 2.3 K is the record value for Ce based heavy fermion superconductivity. Under hydrostatic pressure of roughly 20 kbar a superconducting drop down in resistivity was found for the antiferromagnetic representatives, too. These compounds attracted much attention because of the close neighborhood of magnetism and superconductivity and the presence of quantum critical points concerning magnetic field and pressure [178–180]. Experimental observations indicate that the electronic, magnetic and superconducting properties are essentially three dimensional in Ce*M*In$_5$, despite of their layered structure [181]. Very recently, superlattices of heavy fermion compounds and conventional metals were fabricated by *molecular beam epitaxy* (MBE), i.e. superlattices made of CeIn$_3$ and LaIn$_3$ [182], and of CeCoIn$_5$ and YbCoIn$_5$ [181]. By decreasing the thickness of the heavy fermion layer the dimensionality is reduced artificially, and deviations from the standard Fermi liquid behavior at low temperatures were observed [182]. The critical temperature for superconductivity shrinks with decreasing thickness, and for less than 4 uc no superconducting regime but a large anisotropy of the magnetoresistance and still decreasing resistivity below 1 K was detected. These findings attracted much interest, and they indicate that the coupling of the Cooper pairs increases due to the reduced dimensionality [181, 182].

A weak tendency of the Ce*M*In$_5$ material class towards hybridization and a Ce $4f$ occupancy (n_f) close to 1, has been inferred from previous spectroscopic investigations: *X-ray absorption spectroscopy* (XAS) measurements show a small f^0 signal at the Ce $M_{4,5}$-edge [184, 185] and at the L_3-edge [186, 187], the f^1 related spectral weight at E_F is low in *resonant photoemission spectroscopy* (ResPES) at the Ce $4d-4f$ [188, 189] and Ce $3d-4f$ transition [184]. A detailed knowledge of the $4f$ electron count and their hybridization to the conduction electrons is essential to understand the physical properties.

In this chapter the Ce $3d$ line of cleaved single Ce*M*In$_5$ crystals is considered by *X-ray photoemission spectroscopy* (XPS). A simplified version of the *Gunnarsson-Schönhammer*
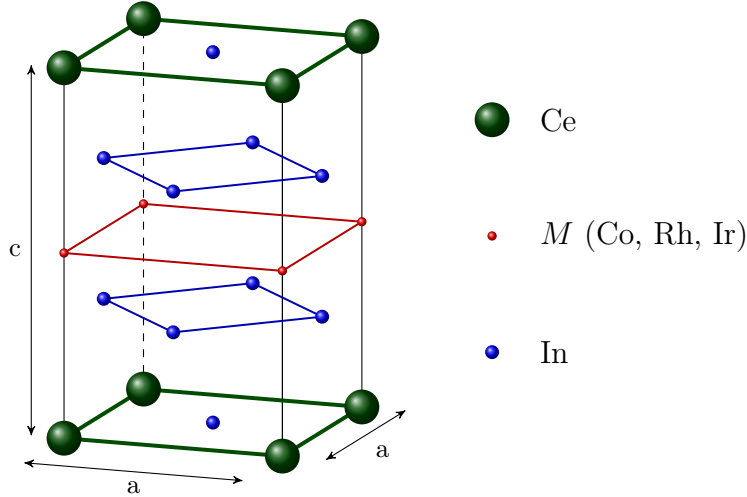
Figure 4.1: HoCoGa$_5$-type tetragonal crystal structure, in which the intermetallic compounds CeMIn$_5$ (M = Co, Rh, and Ir) crystalize. For CeCoIn$_5$ the lattice constants are $a = 4.62$ Å and $a = 7.56$ Å [183].

theory was applied to describe the spectra and obtain the relevant parameters [190]. Photoemission measurements of Ce compounds are often plagued by surface effects. The surface may feature a different hybridization than the bulk [191–193], and, additionally, may degrade very easily since Ce is a very reactive chemical element. In this respect, it is important to disentangle surface and bulk effects. A probe such as temperature and angle dependent Al K_α XPS, used here, seems to be appropriate for this objective, due to its increased bulk sensitivity compared to low energy photoemission. Single crystals of the investigated Ce intermetallic compounds were grown in In flux [25]. The samples were glued on a sample holder by silver epoxy resin and were cooled down to about 30 K by a helium cryostat. Clean surfaces have been prepared by *in situ* cleavage. The base pressure in the experimental chamber was 1×10^{-10} mbar to reduce chemical reactions to residual gas atoms. For binding energy calibration the Au $4f_{7/2}$ signal (84 eV) of a sputtered gold foil was used.

4.2 Spectroscopy on Ce compounds

Crucial physical parameters of heavy fermion materials can be obtained by *photoemission spectroscopy* (PES). However, in Lanthanides the measured excitation spectra are governed not only by the initial state but also strongly by the final state, which requires a careful interpretation. A simplified version of the Gunnarsson-Schönhammer formalism [194] based on the *single impurity Anderson model* [195] was proposed by Imer and Wuilloud [190] to explain the spectroscopic features and to reduce the numerical efforts.

This model was implemented to derive the Ce $4f$ electron count and their hybridization to the conduction electrons by fitting the measured Ce $3d$ spectra.

The photoemission intensity in sudden approximation was already discussed in chapter 2.1.2 (Eq. 2.12). The dipole matrix element is the same for Ce $3d$ core level excitations irrespective of the certain final state of the remaining $(N-1)$ electron system. Therefore the spectral function can be reduced to:

$$I(\varepsilon) \sim \sum_s |\langle F_s \,|\, a_c \,|\, G\rangle|^2 \; \delta(\varepsilon + E_s^{N-1} - E_G^N) \,, \tag{4.1}$$

in which $|G\rangle$ denotes the ground state with an energy E_G^N and $|F_s\rangle$ denote the various final states, that are eigenstates of the $(N-1)$ particle Hamiltonian with an energy E_s^{N-1}. The annihilation operator a_c removes the $3d$ core electron from the initial ground state. Obviously, the energies of the ground state and of the final states define the energy positions of the spectral features and the overlap integral their intensities. These quantities can be evaluated by the single impurity Anderson Hamiltonian [195], which describes local magnetic states incorporated in a metal matrix. In a zero bandwidth limit, the simplified Hamiltonian can be written as [190]:

$$\hat{H} = \hat{H}_0 + V \sum_{\nu=1}^{N_f} \int \mathrm{d}\rho \, (f_\nu^+ \, a_{\rho\nu} + \text{H.c.})$$

$$\hat{H}_0 = \varepsilon_0 \sum_{\nu=1}^{N_f} \int \mathrm{d}\rho \, a_{\rho\nu}^+ \, a_{\rho\nu} + \left[\varepsilon_f - U_{fc}(1 - a_c^+ a_c)\right] \sum_{\nu=1}^{N_f} f_\nu^+ f_\nu$$

$$+ \frac{1}{2} U \sum_{\nu,\mu} f_\nu^+ f_\nu f_\mu^+ f_\mu \; + \; \varepsilon_c \, a_c^+ a_c \,. \tag{4.2}$$

$\hat{H}_0$ is the many-body Hamiltonian of the conduction electrons labeled with ρ and the degenerated f electrons without hybridization. The zero bandwidth limit means that the same energy ε_0 is assumed for all conduction electrons created and annihilated by $a_{\rho\nu}^+$ and $a_{\rho\nu}$. For Ce $4f$ levels and under neglection of spin-orbit interaction the orbital degeneracy is seven. In addition to the spin degeneracy, this leads to a total degeneracy ν of 14 ($N_f = 14$). The energy of the f electrons is ε_f and they are created and annihilated by the respective operators f_ν^+ and f_ν. An on-site Coulomb repulsion energy between f electrons is considered by U. U_{fc} is the core hole Coulomb interaction between f electrons and the core hole created during the photoemission process by the operator a_c^+. The energy of the conduction electrons ε_0 and of the core hole ε_c can be set to zero as

they cause an arbitrary energy shift of the spectrum. One impurity is considered by this model and no interaction between neighboring magnetic sites arranged in a lattice are taken into account. Multiplet effects are entirely neglected in the model, i.e. spin-orbit coupling for the core hole and spin-spin interactions between core hole and unpaired f electrons, whereas the former is taken into account afterwards. The Hamiltonian neglects any electron-phonon interaction ($T = 0$). Finally, the central term taking into account the hybridization or hopping energy between one f electron and a conduction band state is V. Note that for this purpose the hybridization is assumed to be energy and momentum independent.

This many-body system can be described by several final states and a ground state, which are eigenstates of the whole Hamiltonian $\hat{H}$ and can be expressed as linear combinations of eigenstates of the not-hybridized Hamiltonian $\hat{H}_0$ with and without a core hole. In La- and Ce-systems the choice of basis states can be limited to double occupation of the f levels, which results in three $\hat{H}_0$-eigenstates f^0, f^1, f^2 with zero, one or two electrons in a localized f orbital, respectively. An eigenstate with three electrons in the f orbital is unrealistic for La and Ce, due to the large Coulomb repulsion U compared to ε_f. These basis states and their energies with and without core hole are illustrated in Fig. 4.2. The corresponding Hamiltonion, including hybridization, is given in Eq. 4.3 in matrix notation regarding these $\hat{H}_0$-eigenstates. Here, the effective hybridization Δ is linked to the hybridization energy V as it is the average value for all f orbitals and all conduction states:

$$
\hat{H} = \begin{bmatrix} 0 & \Delta & 0 \\ \Delta & \varepsilon_f & \sqrt{2}\Delta \\ 0 & \sqrt{2}\Delta & 2\varepsilon_f + U \end{bmatrix} \xrightarrow{\text{core hole}} \begin{bmatrix} 0 & \Delta & 0 \\ \Delta & \varepsilon_f - U_{fc} & \sqrt{2}\Delta \\ 0 & \sqrt{2}\Delta & 2(\varepsilon_f - U_{fc}) + U \end{bmatrix} . \quad (4.3)
$$

To evaluate the photoemission intensity given in Eq. 4.1 one has to express the ground state and the final states as linear combination of $\hat{H}_0$-eigenstates $|g^i\rangle$ and $|h^i\rangle$ with and without a core hole, respectively, and with i electrons in the $4f$ orbital. This has to be done by diagonalization of the matrices in Eq. 4.3, in particular the calculation of eigenvalues E_G^N, $E^{(}N-1)_s$ and coefficients c_i, $t_{s,j}$. The matrix for the final states
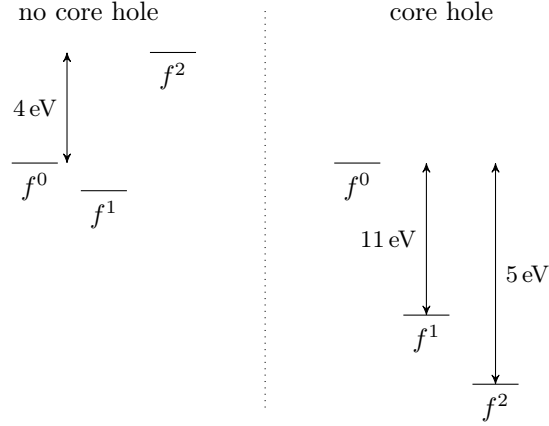
Figure 4.2: Typical energies of different $4f$ configurations of a Ce impurity with and without a core hole, taken from [194]. Configurations are labeled according to the number of f electrons and typical energy differences are indicated.

accounts for the generated core hole by substituting ε_f with $\varepsilon_f - U_{fc}$. $|G\rangle$ and $|F_s\rangle$ are then expressed by:

$$|G\rangle \;=\; \sum_{i=0}^{2} c_i \,|g^i\rangle \;, \tag{4.4}$$

$$|F_s\rangle \;=\; \sum_{j=0}^{2} t_{s,j} \,|h^j\rangle \;. \tag{4.5}$$

Both representations illustrate the mixed valency of Ce in the ground state and final states, i.e. the number n_f of f electrons does not have to be an integer value. The ground state $|G\rangle$ is the eigenstate of $\hat{H}$ with lowest energy and has an f electron count of:

$$n_f = 0 \cdot c_0^2 + 1 \cdot c_1^2 + 2 \cdot c_2^2 \quad , \text{with} \quad \sum_{i=0}^{i=2} c_i^2 = 1 \;. \tag{4.6}$$

Upon photoemission the system has the possibility to remain in three different final states $|F_s\rangle$ with different energies. Since the $\hat{H}_0$-eigenstates are chosen to be orthonormal to each other ($\langle g^i|g^j\rangle = \delta_{ij}$, $\langle h^i|h^j\rangle = \delta_{ij}$, $\langle h^i|a_c|g^j\rangle = \delta_{ij}$), the spectral function is simply:

$$I(\varepsilon) \sim \sum_{s=0}^{2} \left| \sum_{j=0}^{2} t_{sj} c_j \right|^2 \delta(\varepsilon + E_s^{N-1} - E_G^N) \;. \tag{4.7}$$

This formalism yields the relative intensities of three discrete transitions at $E_s^{N-1} - E_G^N$. A more detailed description can be found in reference [190]. It has been implemented to fit the measured Ce $3d$ spectra and to obtain quantitative values for the hybridization parameters Δ and the f occupancy n_f.

For Ce, Δ is usually much smaller than the $f^1 - f^2$ energy separation in the ground state, i.e. $c_2 \sim 0$. Moreover, if the final states are of pure f configuration ($|f^0\rangle$, $|f^1\rangle$, $|f^2\rangle$), often assumed in literature, only the first two final states would couple to the ground state and generate two peaks in the spectrum with spectral weights of $|c_0|^2$ and $|c_1|^2$. Then, n_f is the relative intensity of the f^1 peak. However, a shoulder, which belongs to mainly f^2 character in the final state, is often present in the $3d$ XPS of Ce compounds proving a finite mixing of the f^1 and f^2 final and/or ground states. Gunnarsson and Schönhammer [194] showed that the size of the hybridization Δ can be obtained from the relative intensity of this f^2 spectral component and that the f^0 spectral weight is a semi-quantitative measure of $|c_0|^2 = 1 - n_f$.
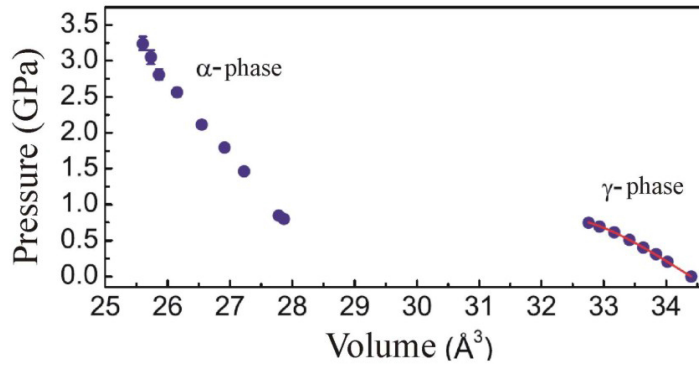
Figure 4.3: At atmospheric pressure the γ-Ce phase is present. It undergoes a phase transition at about $0.7\,\mathrm{GPa}$ to the isostructural α-Ce phase with a drastically reduced unit cell volume, taken from [196].

α- and γ-Ce as prominent examples

The phase transition from γ- to α-Ce is a famous example in order to illustrate the effects of hybridization and the derived formalism for the interpretation of XPS measurements. This isostructural phase transition – both phases share an fcc crystal structure – is usually observed at room temperature under applying pressure or by cooling at atmospheric pressure and is accompanied by a drastic reduction of the lattice constant. The jump in unit cell volume upon pressure induced phase transition is plotted in Fig. 4.3 taken from [196]. The unit cell volume of the low-temperature phase (α-Ce) is about $15\,\%$

smaller than those of γ-Ce due to a different manifestation of the metallic Ce bonds. In particular the symmetry of the bonds and of the Ce electron density is changed [197], which affects the electronic and magnetic properties strongly.
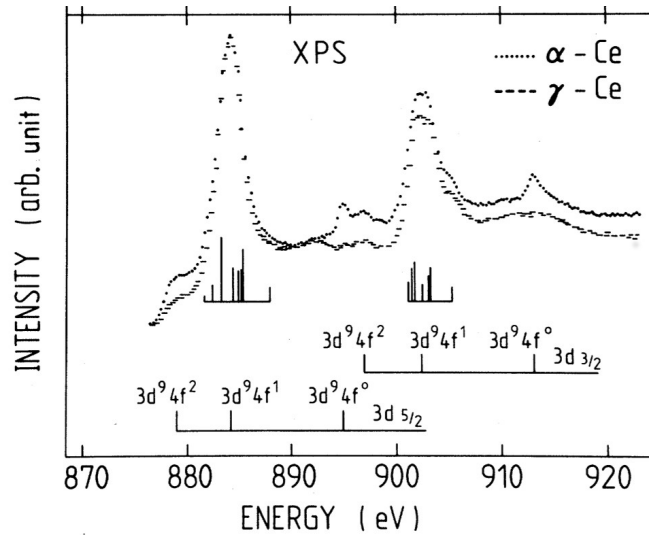

Figure 4.4: Wuilloud *et al.* demonstrated that Ce 3d XPS spectra of γ-Ce and of more strongly hybridized α-Ce are sensitive to the low-energy electronic structure, taken from [198].

An explanation for the different properties is the change in the degree of hybridization between f levels and conduction electrons upon phase transition. At room temperature (γ-Ce) the hybridization is small and the count of localized f electrons per Ce is close to one. Therefore the initial state has a pure $4f^1$ configuration which leads to the absence of a $4f^0$ final state peak in XPS at high binding energy, see Fig. 4.4. In contrast to this, α-Ce exhibits a much larger hybridization leading to a stronger admixture of the $4f^0$ configuration in the initial state, to a decreased number of f electrons and to a larger valency. Hence, in XPS (Fig. 4.4) a peak at high binding energy with a $4f^0$ final state configuration appears as well as a shoulder at the low energy side of the prominent $4f^1$ peak. The latter peak is associated with a $4f^2$ final state configuration. Both peaks are signs for increased f-hybridization and demonstrate that XPS is very sensitive to changes in the low-energy electronic structure.

4.3 Ce 3d core levels

Fig. 4.5 shows the Ce 3d core level spectra for all three CeMIn$_5$ compounds cleaved at $T = 30$ K. The spectra are very similar and have a typical complex lineshape. They are split due to spin-orbit coupling in $d_{5/2}$ and $d_{3/2}$ peaks and each of the spin-orbit compo-
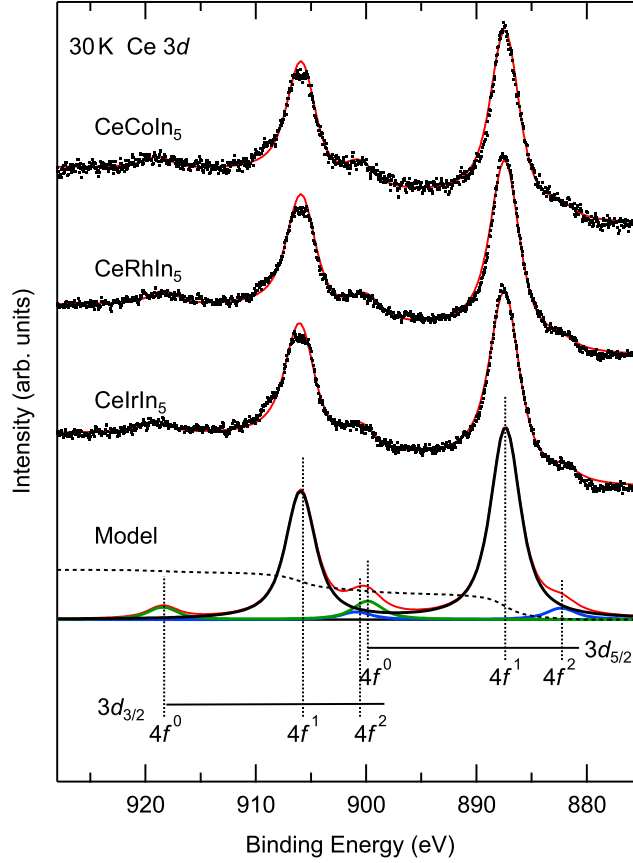
Figure 4.5: Ce $3d$ core level XPS spectra measured with an Al K_α source at normal emission $\Theta = 0°$ (dotted curves). The samples were cleaved at $30\,$K and immediately analyzed. Best fit model calculations are displayed in red solid lines. Spin-orbit doublets with two (blue), one (black) or non (green) f-electrons in the final state are disentangled for the model curve.

nents consists further of three, partly overlapping final states. The most intense doublet belongs to a state of mainly $3d^9 4f^1$ character, whereas the states with mainly $3d^9 4f^2$ and $3d^9 4f^0$ are situated at lower and higher binding energy respectively and are much less intense. These many-body effects in the core level spectra of rare earths compounds have been studied for several decades and are well known [199]. An approximate link to the ground state properties is provided by the low intensity of the $3d_{3/2} - f^0$ peak at $E = 918\,$eV, which indicates that n_f does not deviate much from unity. In fact, the spectra resemble typical γ-like Ce materials [200].

For a more quantitative treatment we have applied the above described simplified version of the Gunnarsson-Schönhammer approach proposed by Imer and Wuilloud [190] to fit the data. The result of the model is shown by red lines in Fig. 4.5. A Shirley background has been added and Gaussian $(1.5\,$eV) and Lorentzian $(2.3\,$eV) broadening were applied

Table 4.1: Parameters extracted from fitting the spectra in Fig. 4.5 with Eq. 4.7. All values are given in eV except for n_f.

sample	ε_f	Δ	U	U_{fc}	n_f
CeCoIn$_5$	-1.26	0.51	8.4	11.8	0.90
CeRhIn$_5$	-1.03	0.47	7.8	11.5	0.88
CeIrIn$_5$	-1.23	0.52	7.9	11.9	0.90

to simulate resolution, multiplet splitting and finite lifetime. The match with the experimental data is satisfactory. Small deviations occur at the high energy side of the $d_{3/2} - f^1$ related peak due to missing multiplet splitting. As a result of this, the intensity of the model for this peak is always larger than the measured spectra. The parameters extracted from the fit are summarized in Tab. 4.1. The obtained spin-orbit splitting of 18.5 eV is the same for all three compounds and coincide with previous reports [201]. The values for U and U_{fc} are in the range of other Ce based materials [202] as well as the values obtained for ε_f [192, 200].
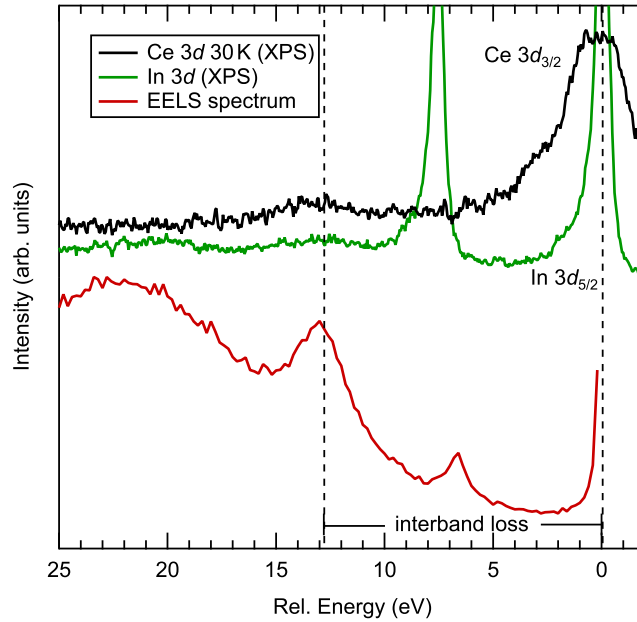
Figure 4.6: Comparison of an EELS (electron energy-loss spectroscopy) measurement of CeRhIn$_5$ with In 3d and Ce 3d photoemission spectra. The position of the interband loss at $E = 13$ eV seen in EELS coincides with the plasmon satellite of the In 3d and Ce 3d lines.

The n_f values are as expected close to 1. In fact, $n_f = 0.9$ has to be still considered as lower boundary because a plasmon satellite is situated below the $3d_{3/2} - f^0$ peak and limits the precision of the analysis. Fig. 4.6 presents an EELS (electron energy-

loss spectroscopy [203]) spectrum of an about 150 nm thick CeRhIn$_5$ film cut with an ultramicrotom. Around $E = 13$ eV a clear peak is observed, which can be assigned to an interband plasmon. This excitation of the electron density appears as satellite peaks in the photoemission spectra as it is shown for the In 3d line. Nevertheless, the values of the hybridization parameter Δ are significantly lower than previous results for strongly hybridized Ce compounds obtained by the same approach [191] and show clearly that CeMIn$_5$ are weakly hybridized systems at $T = 30$ K with an occupation number close to one. This is in qualitative agreement with our ARPES results [189, 204, 205]. n_f values close to 1 have been also extracted from more bulk sensitive XAS at the Ce L_3-edge ($n_f > 0.9$ for CeRhIn$_5$ and CeIrIn$_5$ [186], $n_f \approx 0.9$ for CeCoIn$_5$ [187]). XAS at the Ce $M_{4,5}$-edge showed minimal f^0 admixture for all three compounds, somewhat stronger for CeIrIn$_5$ and CeCoIn$_5$ as compared to CeRhIn$_5$ [185]. A larger f^1 component at the Fermi energy signalling increased hybridization was observed for CeIrIn$_5$ with respect to CeRhIn$_5$ by resonant photoemission [188].

In the standard Kondo-model the f-hybridization should slowly disappear at high temperatures. Therefore, we have studied the temperature dependence of the Ce 3d line by a gradual warming of the cryostat up to room temperature. At certain temperatures additional XPS measurements were performed on the originally at 30 K cleaved sample to evaluate the temperature dependence. Unfortunately, the intrinsic effects, if they are present, are superimposed by surface effects as it is demonstrated in Fig. 4.7 for CeIrIn$_5$. These spectra have been measured at room temperature. They are significantly broadened compared to the 30 K spectra. Cooling the samples down to low temperatures does not recover the narrow line shape. At higher emission angles, i.e. for higher surface sensitivity, the broadening increases. The top spectrum features a sample which has been exposed to oxygen (10 min $p_{O_2} = 1 \times 10^{-7}$ mbar). It strongly resembles Ce$_2$O$_3$ [206–208], i.e. the surface is fully oxidized by this procedure and no more changes with higher oxygen exposure could be observed. The room temperature data in the middle of Fig. 4.7 can be simulated almost perfectly by a superposition of this Ce$_2$O$_3$ type spectrum (Fig. 4.7: gray shaded area) and the narrow low temperature spectrum (Fig. 4.7: red line). In XPS overview spectra, no other contamination besides a small amount of oxygen was discernible that was absent in the 30 K spectra. This indicates that the surface Ce is oxidized when the temperature is increased. The change of the chemical state concerns primarily Ce. Fig. 4.8 presents temperature dependent spectra for Ir and In. While temperature dependent changes are hardly discernible at all, the fully oxidized surface shows a moderate high energy component.

In order to evaluate the extend of oxidation of the surface quantitatively, we applied the fitting procedure from Fig. 4.7 for the full temperature scan. In this way, the relative
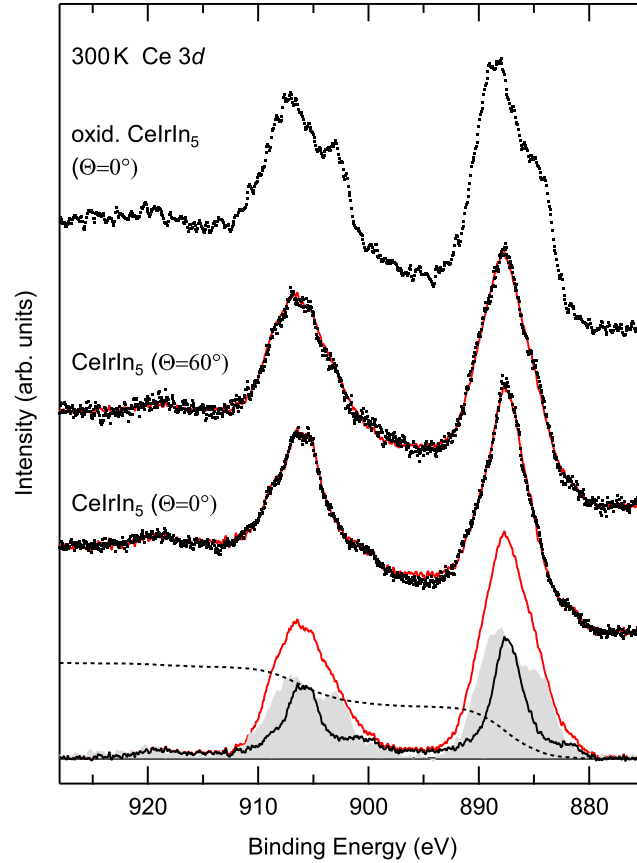
Figure 4.7: Ce $3d$ core level spectra of CeIrIn$_5$ taken at $300\,\mathrm{K}$ and different emission angles Θ with respect to the surface normal. The spectra were superimposed (red curves) with a Shirley background (dashed line), the "$30\,\mathrm{K}$-signal" (black line) and with the spectra of an oxidized crystal (upper spectra and gray shaded area in the lower part), typical for trivalent cerium oxide Ce$_2$O$_3$ [206–208].

intensity of the surface component can be extracted by the integrated intensity ratio of the Ce$_2$O$_3$ type and the whole spectra. Fig. 4.9(a) demonstrates that this component increases monotonically when the temperature is increased starting from $T = 30\,\mathrm{K}$ and shows signs of saturation at higher temperatures. Angle dependent measurements yield higher values, as expected for a surface component, and show in particular, that the oxidation starts already at the lowest temperatures achieved here. The relative intensity can be translated into the thickness of the oxidized surface layer under the assumption that there is a sharp interface and the electron escape length λ is known. The latter has been calculated from the TPP-2M model to be $\lambda = 14\,\text{Å}$[209]. The intensity I of photoexcited electrons at a distance x from the sample surface is damped exponentially by $I(x) \propto e^{-x/\lambda \cos\Theta}$, where Θ is the angle between outgoing electrons and surface normal. Using these assumptions the surface layer thickness has been calculated from the relative intensity of the surface component.
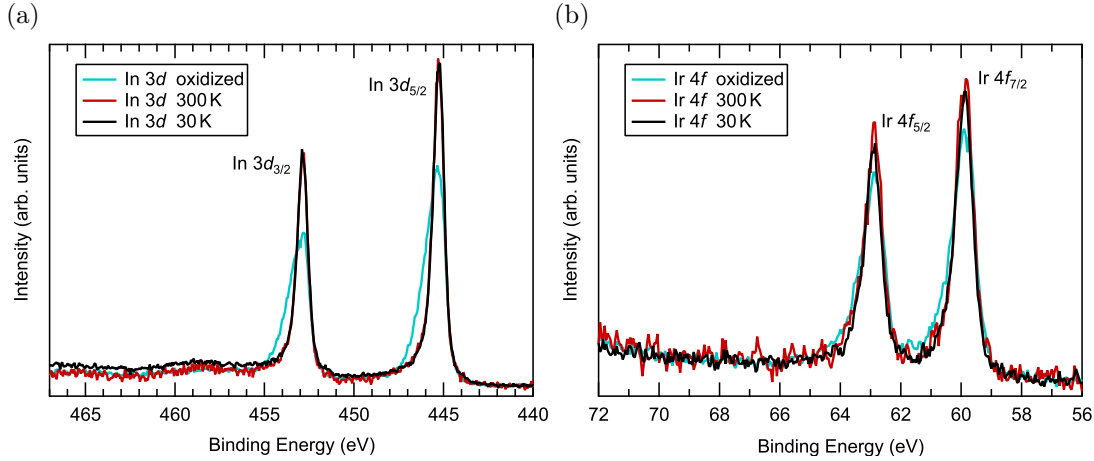
Figure 4.8: Temperature dependence of the In $3d$ (a) and Ir $4f$ (b) lines of CeIrIn$_5$. Contrary to Ce $3d$, the spectral shape and width is nearly unaffected and only moderate changes for the fully oxidized sample can be seen.

Fig. 4.9(b) shows that the oxidized component starts from about a fourth monolayer at low temperatures and levels off around one monolayer at high temperatures, i.e. full surface coverage. The most natural explanation for the formation of the oxide layer is that desorption occurs when the system is warmed up. This process is difficult to avoid and a base pressure of 1×10^{-10} mbar is not enough to prevent it. However, the temperature increase itself may promote surface oxidation as well. The oxidation will take place most easily when the cleavage plane has the CeIn$_3$ layer at the top surface. Formation of a Ce$_2$O$_3$ like phase was also reported as a result of prolonged X-ray irradiation [206]. But in the present case the oxidation process is clearly linked to the temperature development and a slight increase in pressure rather than the irradiation time. This fact is confirmed by the Ce $3d$ spectra of a sample cleaved at room temperature (not shown) which is already broadened in comparison to the "30 K-spectra" and resembles the spectra of the warmed up sample. Previous XPS measurements on polycrystals at room temperature showed also spectral signatures of oxidation [201].

4.4 Concluding remarks

In summary the CeMIn$_5$ family has been investigated by core level photoemission spectroscopy. It has been shown that XPS is sensitive to the low-energy electronic structure, but due to complex final state effects a theoretical model is essential for a correct interpretation. From the Ce $3d$ line at low temperature ($T = 30$ K), a lower bound of the f-occupation number $n_f \geq 0.9$ for all of the three compounds have been obtained,
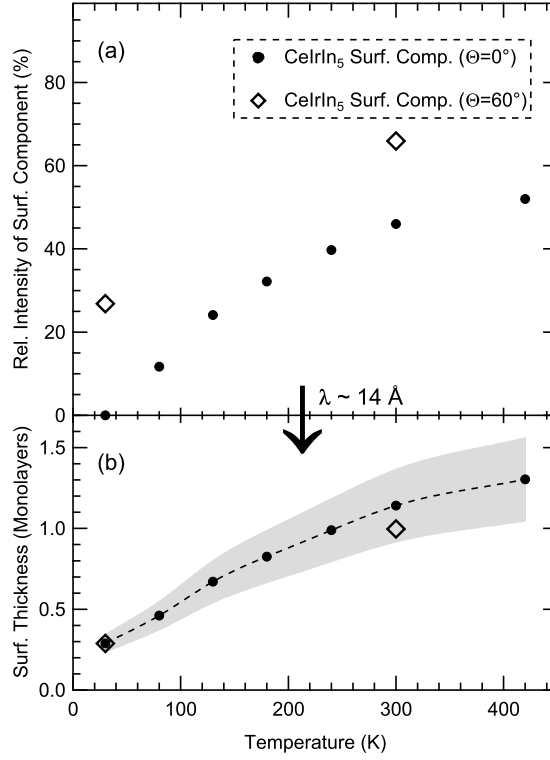
Figure 4.9: (a) Relative intensity of the oxidized signal as a function of temperature extracted by the fitting procedure described in Fig. 4.7. (b) Thickness of the oxidized surface component calculated from the data points in (a) in units of monolayers as a function of temperature.

which characterizes them as weakly hybridized, consistent with previous measurements. Differences in n_f, which were found by other techniques, are masked by plasmonic loss excitations in Ce $3d$ core level photoemission experiments. The surface tends to rapid oxidation independently of the transition metal, in particular when the sample is warmed up. Quantitative analysis shows that the first layer is fully oxidized at room temperature. This effect must be taken into account for temperature dependent and surface sensitive measurement of these and other heavy fermion materials.
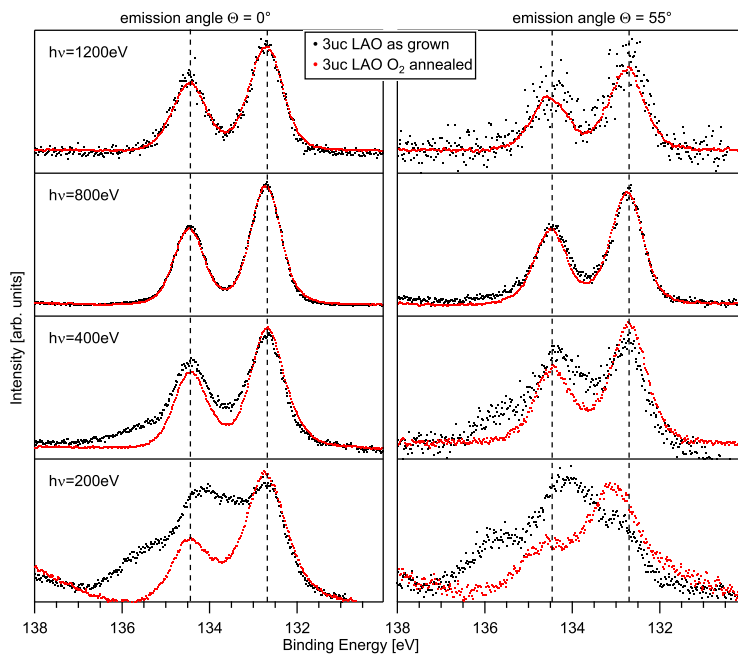
5 Appendix
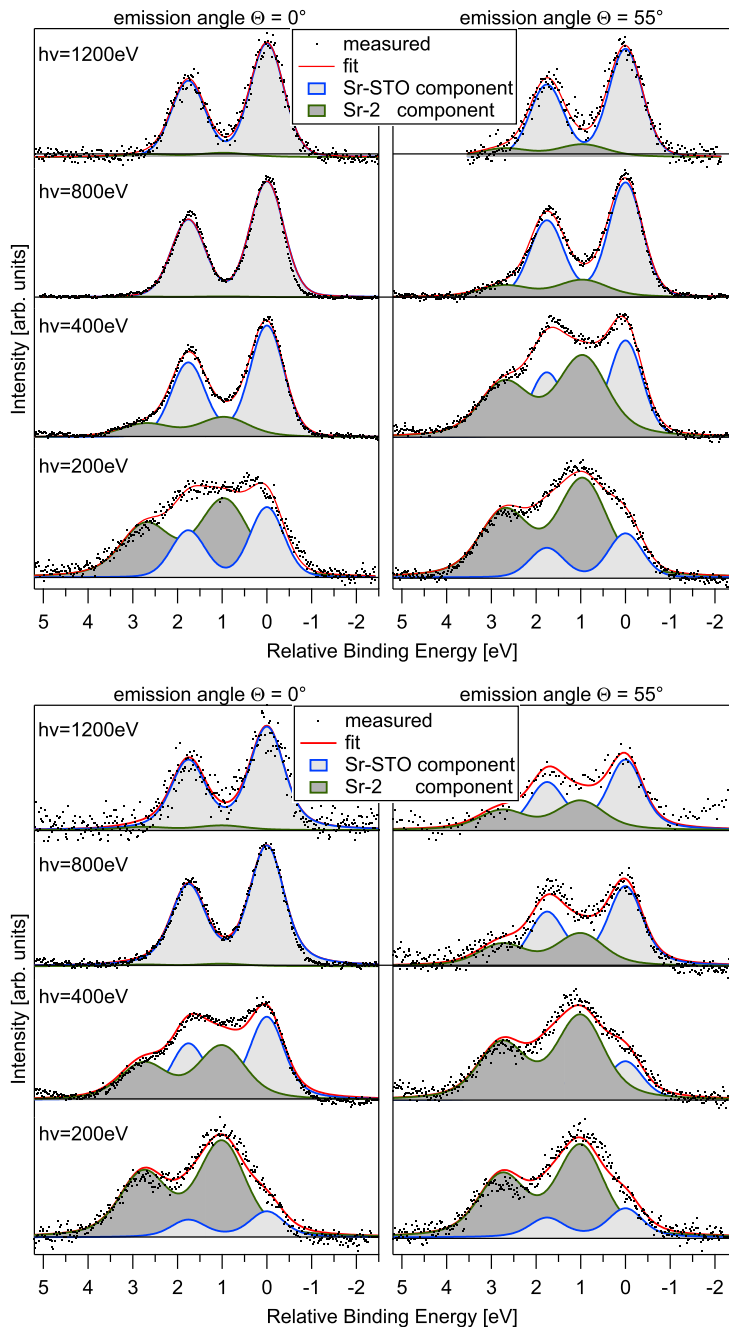
Figure 5.1: Fitted Sr $3d$ core level photoemission spectra of the $3\,\mathrm{uc}$ (top) and $6\,\mathrm{uc}$ (bottom) NGO/STO sample measured at different photon energies $h\nu$ and emission angles Θ. For higher emission angles or lower photon energies (higher surface sensitivity) the second Sr component is enhanced. (see chapter 3.3), page 50)
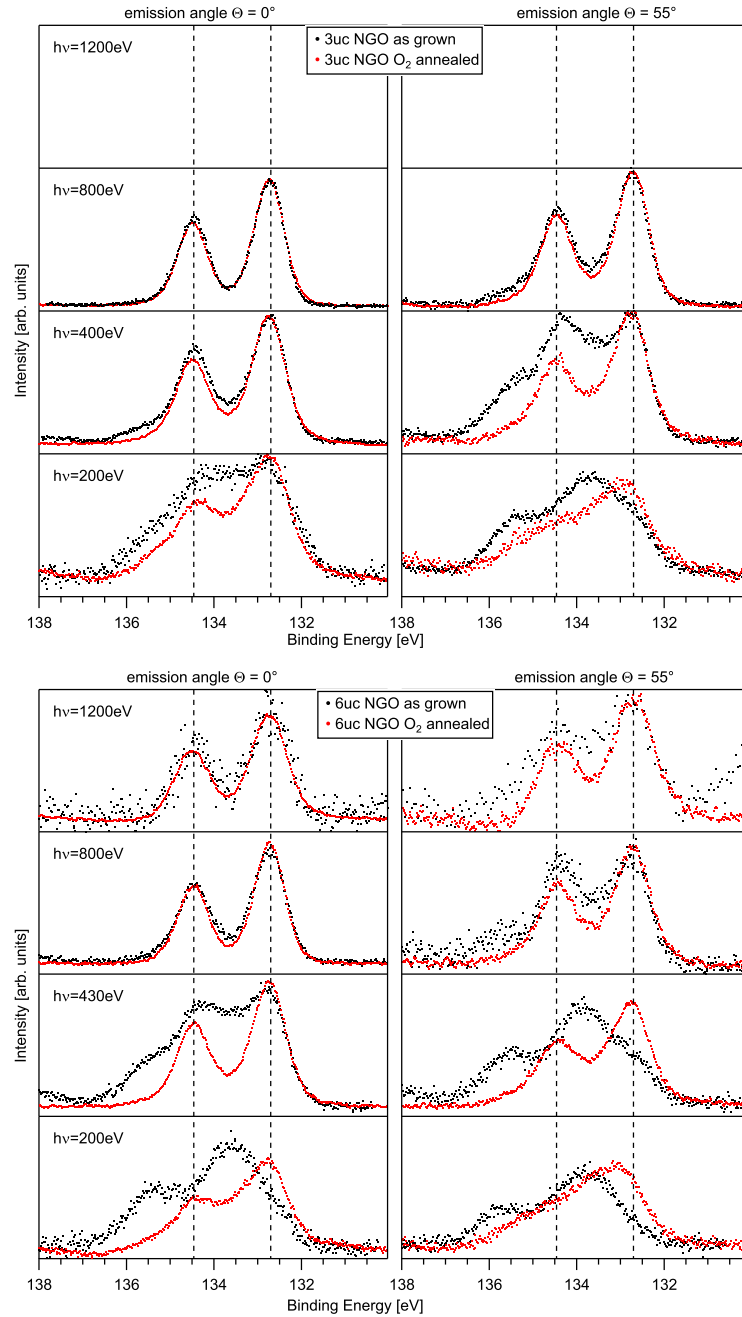
Figure 5.2: Comparison of Sr $3d$ core level photoemission spectra of the 3 uc (top) and 6 uc (bottom) NGO/STO sample at different photon energies $h\nu$ and emission angles Θ. For the red dots the samples were treated by an subsequent post-growth annealing process in oxygen. (see chapter 3.3, page 56)

Figure 5.3: Comparison of Sr $3d$ core level photoemission spectra of the $3\,$uc LAO/STO sample at different photon energies $h\nu$ and emission angles Θ. For the red dots the sample was treated by an subsequent post-growth annealing process in oxygen. (see chapter 3.3, page 56)

Bibliography

[1] A. P. Ramirez, *J. Phys. Condens. Matter* **9**, 8171 (1997), Link.

[2] H. Dulli, P. A. Dowben, S.-H. Liou, and E. W. Plummer, *Phys. Rev. B* **62**, R14629–R14632 (2000), Link.

[3] M. B. Salamon and M. Jaime, *Rev. Mod. Phys.* **73**, 583–628 (2001), Link.

[4] R. Ramesh and N. A. Spaldin, *Nat Mater* **6**, 21–29 (2007), Link.

[5] J. Orenstein and A. J. Millis, *Science* **288**, 468–474 (2000), Link.

[6] Y. Saito, H. Takao, T. Tani, T. Nonoyama, K. Takatori, T. Homma, T. Nagaya, and M. Nakamura, *Nature* **432**, 84–87 (2004), Link.

[7] P. R. Willmott and J. R. Huber, *Rev. Mod. Phys.* **72**, 315–328 (2000), Link.

[8] H. M. Christen and G. Eres, *J. Phys. Condens. Matter* **20**, 264005 (2008), Link.

[9] J. R. Arthur, *Surf. Sci.* **500**, 189–217 (2002), Link.

[10] A. Ohtomo and H. Y. Hwang, *Nature* **427**, 423–426 (2004), Link.

[11] N. Nakagawa, H. Y. Hwang, and D. a. Muller, *Nat. Mater.* **5**, 204–209 (2006), Link.

[12] A. Kalabukhov, R. Gunnarsson, J. Börjesson, E. Olsson, T. Claeson, and D. Winkler, *Phys. Rev. B* **75**, 121404 (2007), Link.

[13] P. R. Willmott, S. A. Pauli, R. Herger, C. M. Schlepütz, D. Martoccia, B. D. Patterson, B. Delley, R. Clarke, D. Kumah, C. Cionca, and Y. Yacoby, *Phys. Rev. Lett.* **99**, 155502 (2007), Link.

[14] S. Chambers, M. Engelhard, V. Shutthanandan, Z. Zhu, T. Droubay, L. Qiao, P. Sushko, T. Feng, H. Lee, T. Gustafsson, E. Garfunkel, A. Shah, J.-M. Zuo, and Q. Ramasse, *Surf. Sci. Rep.* **65**, 317–352 (2010), Link.

[15] M. Salluzzo, J. Cezar, N. Brookes, V. Bisogni, G. De Luca, C. Richter, S. Thiel, J. Mannhart, M. Huijben, a. Brinkman, G. Rijnders, and G. Ghiringhelli, *Phys. Rev. Lett.* **102**, 166804 (2009), Link.

[16] N. Pavlenko and T. Kopp, *Surf. Sci.* **605**, 1114–1121 (2011), Link.

[17] A. Koitzsch, J. Ocker, M. Knupfer, M. C. Dekker, K. Dörr, B. Büchner, and P. Hoffmann, *Phys. Rev. B* **84**, 245121 (2011), Link.

[18] A. D. Caviglia, S. Gariglio, N. Reyren, D. Jaccard, T. Schneider, M. Gabay, S. Thiel, G. Hammerl, J. Mannhart, and J.-M. Triscone, *Nature* **456**, 624–7 (2008), Link.

[19] A. Brinkman, M. Huijben, M. van Zalk, J. Huijben, U. Zeitler, J. C. Maan, W. G. van der Wiel, G. Rijnders, D. H. a. Blank, and H. Hilgenkamp, *Nat. Mater.* **6**, 493–6 (2007), Link.

[20] Y. Xie, Y. Hikita, C. Bell, and H. Y. Hwang, *Nat. Commun.* **2**, 494 (2011), Link.

[21] E. Di Gennaro, U. S. di Uccio, C. Aruta, C. Cantoni, A. Gadaleta, A. R. Lupini, D. Maccariello, D. Marré, I. Pallecchi, D. Paparo, P. Perna, M. Riaz, and F. M. Granozio, *Adv. Opt. Mater.* **1**, 834 (2013), Link.

[22] C. Cen, S. Thiel, G. Hammerl, C. W. Schneider, K. E. Andersen, C. S. Hellberg, J. Mannhart, and J. Levy, *Nat. Mater.* **7**, 298–302 (2008), Link.

[23] K. Andres, J. E. Graebner, and H. R. Ott, *Phys. Rev. Lett.* **35**, 1779–1782 (1975), Link.

[24] H. Hegger, C. Petrovic, E. G. Moshopoulou, M. F. Hundley, J. L. Sarrao, Z. Fisk, and J. D. Thompson, *Phys. Rev. Lett.* **84**, 4986–4989 (2000), Link.

[25] C. Petrovic, P. G. Pagliuso, M. F. Hundley, R. Movshovich, J. L. Sarrao, J. D. Thompson, Z. Fisk, and P. Monthoux, *J. Phys. Condens. Matter* **13**, L337 (2001), Link.

[26] C. Petrovic, R. Movshovich, M. Jaime, P. G. Pagliuso, M. F. Hundley, J. L. Sarrao, Z. Fisk, and J. D. Thompson, *Europhys. Lett.* **53**, 354 (2001), Link.

[27] H. Ibach: *Electron Spectroscopy for Surface Analysis*, Springer-Verlag Berlin (1977).

[28] H. Hertz, *Ann. Phys.* **267**, 983–1000 (1887), Link.

[29] A. Einstein, *Ann. Phys.* **17**, 132 (1905), Link.

[30] C. Berglund and W. Spicer, *Phys. Rev.* **136**, A1044 (1964).

[31] C. Berglund and W. Spicer, *Phys. Rev.* **136**, A1030 (1964).

[32] S. Hüfner: *Photoelectron Spectroscopy*, Springer-Verlag Berlin (1995).

[33] H. Lüth: *Surfaces and Interfaces of Solids*, Springer-Verlag Berlin (1993).

[34] A. Damascelli, Z. Hussain, and Z.-X. Shen, *Rev. Mod. Phys.* **75**, 473–541 (2003), Link.

[35] F. Reinert and S. Hüfner, *New J. Phys.* **7**, 97 (2005), Link.

[36] M. Randeria, H. Ding, J.-C. Campuzano, A. Bellman, G. Jennings, T. Yokoya, T. Takahashi, H. Katayama-Yoshida, T. Mochiku, and K. Kadowaki, *Phys. Rev. Lett.* **74**, 4951–4954 (1995), Link.

[37] P. S. J.F. Moulder W.F. Stickle and K. Bomben: *Handbook of X-ray Photoelectron Spectroscopy*, Perkin-Elmer Cooperation (1992).

[38] D. A. Shirley, *Phys. Rev. B* **5**, 4709 (1972).

[39] M. Henzler and W. Göpel: *Oberflächenphysik des Festkörpers*, B.G. Teubner Stuttgart (1991).

[40] U. Gelius, E. Basilier, S. Svensson, T. Bergmark, and K. Siegbahn, *J. Electron Spectrosc. Relat. Phenom.* **2**, 405 (1973), Link.

[41] F. de Groot, *Coord. Chem. Rev.* **249**, 31–63 (2005), Link.

[42] D. A. Cole, J. R. Shallenberger, S. W. Novak, R. L. Moore, M. J. Edgell, S. P. Smith, C. J. Hitzman, J. F. Kirchhoff, E. Principe, W. Nieveen, F. K. Huang, S. Biswas, R. J. Bleiler, and K. Jones, *J. Vac. Sci. Technol., B* **18**, 440–444 (2000), Link.

[43] R. Paynter, *J. Electron Spectrosc. Relat. Phenom.* **169**, 1–9 (2009), Link.

[44] H. Iwai, J. S. Hammind, and S. Tanuma, *J. Surf. Anal.* **15**, 264–270 (2009).

[45] M. P. Seah et al., *Surf. Interface Anal.* **36**, 1269–1303 (2004), Link.

[46] Y. F. Chen, C. M. Kwei, and C. J. Tung, *J. Phys. D: Appl. Phys.* **25**, 262 (1992), Link.

[47] J. B. Hudson: *Surface Science: An Introduction*, Wiley-Interscience (1998).

[48] M. Seah and W. Dench, *Surf. Interface Anal.* **1**, 2 (1979).

[49] S. Tanuma, C. Powell, and D. Penn, *Surf. Interface Anal.* **35**, 268–275 (2003).

[50] S. Tanuma, C. Powell, and D. Penn, *Surf. Sci.* **192**, L849–L857 (1987).

[51] J. Stöhr: *NEXAFS Spectroscopy*, Springer (1992).

[52] L. Meitner, *Zeitschrift für Physik* **9**, 131–144 (1922).

[53] B. H. Frazer, B. Gilbert, B. R. Sonderegger, and G. D. Stasio, *Surf. Sci.* **537**, 161–167 (2003), Link.

[54] A. Ruosi, C. Raisch, A. Verna, R. Werner, B. A. Davidson, J. Fujii, R. Kleiner, and D. Koelle, URL: `http://arxiv.org/abs/1310.5998` (2013).

[55] M. Haverkort: *Spin and orbital degrees of freedom in transition metal oxides and oxide thin films studied by soft x-ray absorption spectroscopy*. PhD thesis, (2005).

[56] G. Drera, URL: `http://arxiv.org/abs/1210.8000` (2012).

[57]   A. Tanaka and T. Jo, *J. Phys. Soc. Jpn.* **63**, 2788–2807 (1994), Link.

[58]   F. M. F. de Groot, J. C. Fuggle, B. T. Thole, and G. A. Sawatzky, *Phys. Rev. B* **41**, 928–937 (1990), Link.

[59]   F. de Groot, *J. Electron Spectrosc. Relat. Phenom.* **67**, 529–622 (1994), Link.

[60]   P. A. Brühwiler, O. Karis, and N. Mårtensson, *Rev. Mod. Phys.* **74**, 703–740 (2002), Link.

[61]   J. Als-Nielsen and D. McMorrow: *Elements of Modern X-ray Physics*, John Willey & Sons Ltd (2011).

[62]   A. S. Bhalla, R. Guo, and R. Roy, *Mater. Res. Innovations* **4**, 3–26 (2000), Link.

[63]   M. Johnsson and P. Lemmens, *J. Phys. Condens. Matter* **20**, 264001 (2008), Link.

[64]   G. H. Haertling, *J. Am. Ceram. Soc.* **82**, 797–818 (1999), Link.

[65]   D. Serrate, J. M. D. Teresa, and M. R. Ibarra, *J. Phys. Condens. Matter* **19**, 023201 (2007), Link.

[66]   N. F. Mott: *Metal-insulator transition*, Taylor & Francis, London (1990).

[67]   J. Hubbard, *Proc. R. Soc. London, Ser. A* **276**, 238–257 (1963), Link.

[68]   M. Huijben, A. Brinkman, G. Koster, G. Rijnders, H. Hilgenkamp, and D. H. A. Blank, *Adv. Mater.* **21**, 1665–1677 (2009), Link.

[69]   A. D. Caviglia, S. Gariglio, C. Cancellieri, B. Sacépé, A. Fête, N. Reyren, M. Gabay, A. F. Morpurgo, and J.-M. Triscone, *Phys. Rev. Lett.* **105**, 236802 (2010), Link.

[70]   N. Reyren, S. Thiel, A. D. Caviglia, L. F. Kourkoutis, G. Hammerl, C. Richter, C. W. Schneider, T. Kopp, A.-S. Rüetschi, D. Jaccard, M. Gabay, D. A. Muller, J.-M. Triscone, and J. Mannhart, *Science* **317**, 1196–1199 (2007), Link.

[71]   S. Gariglio, N. Reyren, A. D. Caviglia, and J.-M. Triscone, *J. Phys. Condens. Matter* **21**, 164213 (2009), Link.

[72]   J. A. Bert, B. Kalisky, C. Bell, M. Kim, Y. Hikita, H. Y. Hwang, and K. A. Moler, *Nat. Phys.* **7**, 767–771 (2011), Link.

[73]   B. Kalisky, J. A. Bert, B. B. Klopfer, C. Bell, H. K. Sato, M. Hosoda, Y. Hikita, H. Y. Hwang, and K. A. Moler, *Nat Commun* **3**, 922 (2012), Link.

[74]   M. Ben Shalom, M. Sachs, D. Rakhmilevitch, A. Palevski, and Y. Dagan, *Phys. Rev. Lett.* **104**, 126802 (2010), Link.

[75]   X. Wang, W. M. Lü, a. Annadi, Z. Q. Liu, K. Gopinadhan, S. Dhar, and T. Venkatesan, *Phys. Rev. B* **84**, 075312 (2011), Link.

[76] A. Tebano, E. Fabbri, D. Pergolesi, G. Balestrino, and E. Traversa, *ACS Nano* **6**, 1278–1283 (2012), Link.

[77] S. Thiel, G. Hammerl, A. Schmehl, C. W. Schneider, and J. Mannhart, *Science* **313**, 1942–1945 (2006), Link.

[78] Ariando, X. Wang, G. Baskaran, Z. Q. Liu, J. Huijben, J. B. Yi, A. Annadi, A. R. Barman, A. Rusydi, S. Dhar, Y. P. Feng, J. Ding, H. Hilgenkamp, and T. Venkatesan, *Nat. Commun.* **2**, 188 (2011), Link.

[79] U. S. di Uccio, C. Aruta, C. Cantoni, E. Di Gennaro, A. Gadaleta, A. R. Lupini, D. Maccariello, D. Marré, I. Pallecchi, D. Paparo, P. Perna, M. Riaz, and F. Miletto Granozio, URL: http://arxiv.org/abs/1206.5083 (2012).

[80] Y. Chen, N. Pryds, J. E. Kleibeuker, G. Koster, J. Sun, E. Stamate, B. Shen, G. Rijnders, and S. Linderoth, *Nano Lett.* **11**, 3774–3778 (2011), Link.

[81] G. Drera, G. Salvinelli, A. Brinkman, M. Huijben, G. Koster, H. Hilgenkamp, G. Rijnders, D. Visentin, and L. Sangaletti, *Phys. Rev. B* **87**, 075435 (2013), Link.

[82] E. Slooten et al., *Phys. Rev. B* **87**, 085128 (2013), Link.

[83] Y. Segal, J. H. Ngai, J. W. Reiner, F. J. Walker, and C. H. Ahn, *Phys. Rev. B* **80**, 241107 (2009), Link.

[84] G. Berner, A. Müller, F. Pfaff, J. Walde, C. Richter, J. Mannhart, S. Thiess, A. Gloskovskii, W. Drube, M. Sing, and R. Claessen, *Phys. Rev. B* **88**, 115111 (2013), Link.

[85] M. Park, S. Rhim, and A. Freeman, *Phys. Rev. B* **74**, 205416 (2006), Link.

[86] R. Pentcheva and W. Pickett, *Phys. Rev. B* **74**, 035112 (2006), Link.

[87] R. Pentcheva and W. E. Pickett, *Phys. Rev. Lett.* **99**, 016802 (2007), Link.

[88] J.-M. Albina, M. Mrovec, B. Meyer, and C. Elsässer, *Phys. Rev. B* **76**, 165103 (2007), Link.

[89] U. Schwingenschlögl and C. Schuster, *Europhys. Lett.* **81**, 17007 (2008), Link.

[90] S. Okamoto and A. J. Millis, *Nature* **428**, 630–633 (2004), Link.

[91] S. Okamoto, A. Millis, and N. Spaldin, *Phys. Rev. Lett.* **97**, 056802 (2006), Link.

[92] F. Lechermann, L. Boehnke, and D. Grieger, *Phys. Rev. B* **87**, 241101 (2013), Link.

[93] R. Pentcheva and W. E. Pickett, *J. Phys. Condens. Matter* **22**, 043001 (2010), Link.

[94] A. Spinelli, M. A. Torija, C. Liu, C. Jan, and C. Leighton, *Phys. Rev. B* **81**, 155110 (2010), Link.

[95]   Z. Q. Liu, C. J. Li, W. M. Lü, X. H. Huang, Z. Huang, S. W. Zeng, X. P. Qiu, L. S. Huang, A. Annadi, J. S. Chen, J. M. D. Coey, T. Venkatesan, and Ariando, *Phys. Rev. X* **3**, 021010 (2013), Link.

[96]   G. Rijnders and D. H. A. Blank, *Nat. Mater.* **7**, 270–271 (2008), Link.

[97]   Z. Q. Liu, D. P. Leusink, X. Wang, W. M. Lü, K. Gopinadhan, A. Annadi, Y. L. Zhao, X. H. Huang, S. W. Zeng, Z. Huang, A. Srivastava, S. Dhar, T. Venkatesan, and Ariando, *Phys. Rev. Lett.* **107**, 146802 (2011), Link.

[98]   O. N. Tufte and P. W. Chapman, *Phys. Rev.* **155**, 796–802 (1967), Link.

[99]   S. A. Chambers, *Surf. Sci.* **605**, 1133–1140 (2011), Link.

[100] V. Vonk, M. Huijben, K. Driessen, P. Tinnemans, A. Brinkman, S. Harkema, and H. Graafsma, *Phys. Rev. B* **75**, 235417 (2007), Link.

[101] V. Vonk, J. Huijben, D. Kukuruznyak, A. Stierle, H. Hilgenkamp, A. Brinkman, and S. Harkema, *Phys. Rev. B* **85**, 045401 (2012), Link.

[102] A. S. Kalabukhov, Y. A. Boikov, I. T. Serenkov, V. I. Sakharov, V. N. Popok, R. Gunnarsson, J. Börjesson, N. Ljustina, E. Olsson, D. Winkler, and T. Claeson, *Phys. Rev. Lett.* **103**, 146101 (2009), Link.

[103] L. Qiao, T. C. Droubay, V. Shutthanandan, Z. Zhu, P. V. Sushko, and S. A. Chambers, *J. Phys. Condens. Matter* **22**, 312201 (2010), Link.

[104] L. Qiao, T. C. Droubay, T. Varga, M. E. Bowden, V. Shutthanandan, Z. Zhu, T. C. Kaspar, and S. A. Chambers, *Phys. Rev. B* **83**, 085408 (2011), Link.

[105] C. Cantoni, J. Gazquez, F. Miletto Granozio, M. P. Oxley, M. Varela, A. R. Lupini, S. J. Pennycook, C. Aruta, U. S. di Uccio, P. Perna, and D. Maccariello, *Adv. Mater.* **24**, 3952–7 (2012), Link.

[106] M. Salluzzo, S. Gariglio, X. Torrelles, Z. Ristic, R. Di Capua, J. Drnec, M. M. Sala, G. Ghiringhelli, R. Felici, and N. B. Brookes, *Adv. Mater.* **25**, 2333–2338 (2013), Link.

[107] F. Schoofs, M. A. Carpenter, M. E. Vickers, M. Egilmez, T. Fix, J. E. Kleibeuker, J. L. MacManus-Driscoll, and M. G. Blamire, *J. Phys. Condens. Matter* **25**, 175005 (2013), Link.

[108] A. Frey, U. Bass, S. Mahapatra, C. Schumacher, J. Geurts, and K. Brunner, *Phys. Rev. B* **82**, 195318 (2010), Link.

[109] F. J. Wong, S.-H. Baek, R. V. Chopdekar, V. V. Mehta, H.-W. Jang, C.-B. Eom, and Y. Suzuki, *Phys. Rev. B* **81**, 161101 (2010), Link.

[110] Y. Hotta, T. Susaki, and H. Y. Hwang, *Phys. Rev. Lett.* **99**, 236805 (2007), Link.

[111] P. Perna, D. Maccariello, M. Radovic, U. Scotti di Uccio, I. Pallecchi, M. Codda, D. Marré, C. Cantoni, J. Gazquez, M. Varela, S. J. Pennycook, and F. M. Granozio, *Appl. Phys. Lett.* **97**, 152111 (2010), Link.

[112] C. Aruta, S. Amoruso, R. Bruzzese, X. Wang, D. Maccariello, F. M. Granozio, and U. S. di Uccio, *Appl. Phys. Lett.* **97**, 252105 (2010), Link.

[113] S. Amoruso, C. Aruta, P. Aurino, R. Bruzzese, X. Wang, F. M. Granozio, and U. S. di Uccio, *Appl. Surf. Sci.* **258**, 9116–9122 (2012), Link.

[114] C. Aruta, S. Amoruso, G. Ausanio, R. Bruzzese, E. Di Gennaro, M. Lanzano, F. Miletto Granozio, M. Riaz, A. Sambri, U. Scotti di Uccio, and X. Wang, *Appl. Phys. Lett.* **101**, 031602 (2012), Link.

[115] A. Annadi, A. Putra, Z. Q. Liu, X. Wang, K. Gopinadhan, Z. Huang, S. Dhar, T. Venkatesan, and Ariando, *Phys. Rev. B* **86**, 085450 (2012), Link.

[116] M. Cardona, *Phys. Rev.* **140**, A651–A655 (1965), Link.

[117] K. van Benthem, C. Elsässer, and R. H. French, *J. Appl. Phys.* **90**, 6156–6164 (2001), Link.

[118] S.-G. Lim, S. Kriventsov, T. N. Jackson, J. H. Haeni, D. G. Schlom, A. M. Balbashov, R. Uecker, P. Reiche, J. L. Freeouf, and G. Lucovsky, *J. Appl. Phys.* **91**, 4500–4505 (2002), Link.

[119] K. Ogisu, A. Ishikawa, Y. Shimodaira, T. Takata, H. Kobayashi, and K. Domen, *J. Phys. Chem. C* **112**, 11978–11984 (2008), Link.

[120] A. H. Reshak, M. Piasecki, S. Auluck, I. V. Kityk, R. Khenata, B. Andriyevsky, C. Cobet, N. Esser, A. Majchrowski, M. Świrkowicz, R. Diduszko, and W. Szyrski, *J. Phys. Chem. B* **113**, 15237–15242 (2009), Link.

[121] Y. A. Abramov, V. G. Tsirelson, V. E. Zavodnik, S. A. Ivanov, and I. D. Brown, *Acta Crystallogr. Sect. B* **51**, 942–951 (1995), Link.

[122] C. J. Howard, B. J. Kennedy, and B. C. Chakoumakos, *J. Phys. Condens. Matter* **12**, 349 (2000), Link.

[123] W. Marti, P. Fischer, F. Altorfer, H. J. Scheel, and M. Tadin, *J. Phys. Condens. Matter* **6**, 127 (1994), Link.

[124] C. S. Koonce, M. L. Cohen, J. F. Schooley, W. R. Hosler, and E. R. Pfeiffer, *Phys. Rev.* **163**, 380–389 (1967).

[125] F. M. Granozio: *private communication*.

[126] J. M. Van Hove, P. Pukite, P. I. Cohen, and C. S. Lent, *J. Vac. Sci. Technol., A* **1**, 609–613 (1983), Link.

[127]   M. Riaz: *Transport Properties of Transition Metal Oxide Thin Films and Interfaces under Light Irradiation*. PhD thesis, (2011).

[128]   A. Gunhold, K. Gömann, L. Beuermann, M. Frerichs, G. Borchardt, V. Kempter, and W. Maus-Friedrichs, *Surf. Sci.* **507–510**, 447–452 (2002), Link.

[129]   W. Jung and H. L. Tuller, *Energy Environ. Sci.* **5**, 5370–5378 (2012), Link.

[130]   M. Radovic, M. Salluzzo, Z. Ristic, R. Di Capua, N. Lampis, R. Vaglio, and F. Miletto Granozio, *J. Chem. Phys.* **135**, 034705 (2011), Link.

[131]   R. Ciancio, E. Carlino, C. Aruta, D. Maccariello, F. M. Granozio, and U. Scotti di Uccio, *Nanoscale* **4**, 91–94 (2012), Link.

[132]   F. Gunkel, P. Brinks, S. Hoffmann-Eifert, R. Dittmann, M. Huijben, J. E. Kleibeuker, G. Koster, G. Rijnders, and R. Waser, *Appl. Phys. Lett.* **100**, 052103 (2012), Link.

[133]   J. Yeh and I. Lindau, *At. Data. Nucl. Data Tables* **32**, 1–155 (1985), Link.

[134]   M. Takizawa, S. Tsuda, T. Susaki, H. Y. Hwang, and a. Fujimori, *Phys. Rev. B* **84**, 245124 (2011), Link.

[135]   K. Szot, W. Speier, U. Breuer, R. Meyer, J. Szade, and R. Waser, *Surf. Sci.* **460**, 112–128 (2000), Link.

[136]   P. van der Heide, Q. Jiang, Y. Kim, and J. Rabalais, *Surf. Sci.* **473**, 59–70 (2001), Link.

[137]   R. Vasquez, *J. Electron Spectrosc. Relat. Phenom.* **56**, 217–240 (1991), Link.

[138]   N. Menou et al., *J. Appl. Phys.* **106**, 094101 (2009), Link.

[139]   K. Yoshimatsu, R. Yasuhara, H. Kumigashira, and M. Oshima, *Phys. Rev. Lett.* **101**, 026802 (2008), Link.

[140]   M. P. Warusawithana et al., *Nat. Commun.* **4**, 2351 (2013), Link.

[141]   G. D. Maria and V. Piacente, *J. Chem. Thermodyn.* **6**, 1–7 (1974), Link.

[142]   G. Drera, F. Banfi, F. F. Canova, P. Borghetti, L. Sangaletti, F. Bondino, E. Magnano, J. Huijben, M. Huijben, G. Rijnders, D. H. A. Blank, H. Hilgenkamp, and A. Brinkman, *Appl. Phys. Lett.* **98**, 052907 (2011), Link.

[143]   M. Sing, G. Berner, K. Goß, a. Müller, a. Ruff, a. Wetscherek, S. Thiel, J. Mannhart, S. Pauli, C. Schneider, P. Willmott, M. Gorgoi, F. Schäfers, and R. Claessen, *Phys. Rev. Lett.* **102**, 176805 (2009), Link.

[144]   K. Okada and A. Kotani, *J. Electron Spectrosc. Relat. Phenom.* **62**, 131–140 (1993), Link.

[145] Y. Ishida, R. Eguchi, M. Matsunami, K. Horiba, M. Taguchi, A. Chainani, Y. Senba, H. Ohashi, H. Ohta, and S. Shin, *Phys. Rev. Lett.* **100**, 056401 (2008), Link.

[146] S. S. a. Seo, Z. Marton, W. S. Choi, G. W. J. Hassink, D. H. a. Blank, H. Y. Hwang, T. W. Noh, T. Egami, and H. N. Lee, *Appl. Phys. Lett.* **95**, 082107 (2009), Link.

[147] G. Berner, S. Glawion, J. Walde, F. Pfaff, H. Hollmark, L.-C. Duda, S. Paetel, C. Richter, J. Mannhart, M. Sing, and R. Claessen, *Phys. Rev. B* **82**, 241405 (2010), Link.

[148] G. Berner, M. Sing, H. Fujiwara, A. Yasui, Y. Saitoh, A. Yamasaki, Y. Nishitani, A. Sekiyama, N. Pavlenko, T. Kopp, C. Richter, J. Mannhart, S. Suga, and R. Claessen, *Phys. Rev. Lett.* **110**, 247601 (2013), Link.

[149] C. Cancellieri, M. L. Reinle-Schmitt, M. Kobayashi, V. N. Strocov, T. Schmitt, P. R. Willmott, S. Gariglio, and J.-M. Triscone, *Phys. Rev. Lett.* **110**, 137601 (2013), Link.

[150] L. C. Davis, *J. Appl. Phys.* **59**, R25–R64 (1986), Link.

[151] K. Ichikawa, O. Aita, K. Aoki, M. Kamada, and K. Tsutsumi, *Phys. Rev. B* **45**, 3221–3229 (1992), Link.

[152] S. Piskunov, E. Heifets, R. Eglitis, and G. Borstel, *Comp. Mater. Sci.* **29**, 165–178 (2004), Link.

[153] Z. Zhang, S.-P. Jeng, and V. E. Henrich, *Phys. Rev. B* **43**, 12004–12011 (1991), Link.

[154] T. Higuchi, T. Tsukamoto, N. Sata, M. Ishigame, Y. Tezuka, and S. Shin, *Phys. Rev. B* **57**, 6978–6983 (1998), Link.

[155] M. Takizawa et al., *Phys. Rev. Lett.* **97**, 057601 (2006), Link.

[156] N. C. Plumb, M. Kobayashi, M. Salluzzo, E. Razzoli, C. Matt, V. N. Strocov, K.-J. Zhou, C. Monney, T. Schmitt, M. Shi, J. Mesot, L. Patthey, and M. Radovic, URL: http://arxiv.org/abs/1304.5948 (2013).

[157] A. F. Santander-Syro et al., *Nature* **469**, 189–193 (2011), Link.

[158] W. Meevasana, P. D. C. King, R. H. He, S.-K. Mo, M. Hashimoto, A. Tamai, P. Songsiririthigul, F. Baumberger, and Z.-X. Shen, *Nat. Mater.* **10**, 114–118 (2011), Link.

[159] R. Di Capua, M. Radovic, G. M. De Luca, I. Maggio-Aprile, F. Miletto Granozio, N. C. Plumb, Z. Ristic, U. Scotti di Uccio, R. Vaglio, and M. Salluzzo, *Phys. Rev. B* **86**, 155425 (2012), Link.

[160]   N. C. Plumb et al., URL: http://arxiv.org/abs/1302.0708 (2013).

[161]   W. Siemons, G. Koster, H. Yamamoto, W. Harrison, G. Lucovsky, T. Geballe, D. Blank, and M. Beasley, *Phys. Rev. Lett.* **98**, 196802 (2007), Link.

[162]   W. Siemons, G. Koster, H. Yamamoto, T. Geballe, D. Blank, and M. Beasley, *Phys. Rev. B* **76**, 155111 (2007), Link.

[163]   L. Rimai and G. A. de Mars, *Phys. Rev.* **127**, 702–710 (1962), Link.

[164]   P. A. Fleury, J. F. Scott, and J. M. Worlock, *Phys. Rev. Lett.* **21**, 16–19 (1968), Link.

[165]   G. Herranz, M. Basletić, M. Bibes, C. Carrétéro, E. Tafra, E. Jacquet, K. Bouze-houane, C. Deranlot, a. Hamzić, J.-M. Broto, A. Barthélémy, and A. Fert, *Phys. Rev. Lett.* **98**, 216803 (2007), Link.

[166]   R. Pentcheva and W. E. Pickett, *Phys. Rev. Lett.* **102**, 107602 (2009), Link.

[167]   M. Basletic, J.-L. Maurice, C. Carrétéro, G. Herranz, O. Copie, M. Bibes, E. Jacquet, K. Bouzehouane, S. Fusil, and a. Barthélémy, *Nat. Mater.* **7**, 621–5 (2008), Link.

[168]   G. Drera, G. Salvinelli, F. Bondino, E. Magnano, M. Huijben, A. Brinkman, and L. Sangaletti, *Phys. Rev. B* **90**, 035124 (2014), Link.

[169]   A. Fujimori, I. Hase, M. Nakamura, H. Namatame, Y. Fujishima, Y. Tokura, M. Abbate, F. M. F. de Groot, M. T. Czyzyk, J. C. Fuggle, O. Strebel, F. Lopez, M. Domke, and G. Kaindl, *Phys. Rev. B* **46**, 9841–9844 (1992), Link.

[170]   G. Drera, L. Sangaletti, F. Bondino, M. Malvestuto, L. Malavasi, Y. Diaz-Fernandez, S. Dash, M. C. Mozzati, and P. Galinetto, *J. Phys. Condens. Matter* **25**, 075502 (2013), Link.

[171]   D. K. Schroder, *Meas. Sci. Technol.* **12**, 16 (2001).

[172]   M. C. Tarun, F. A. Selim, and M. D. McCluskey, *Phys. Rev. Lett.* **111**, 187403 (2013), Link.

[173]   S. A. Chambers, L. Qiao, T. C. Droubay, T. C. Kaspar, B. W. Arey, and P. V. Sushko, *Phys. Rev. Lett.* **107**, 206802 (2011), Link.

[174]   B.-C. Huang, Y.-P. Chiu, P.-C. Huang, W.-C. Wang, V. T. Tra, J.-C. Yang, Q. He, J.-Y. Lin, C.-S. Chang, and Y.-H. Chu, *Phys. Rev. Lett.* **109**, 246807 (2012), Link.

[175]   R. Jany, C. Richter, C. Woltmann, G. Pfanzelt, B. Förg, M. Rommel, T. Reindl, U. Waizmann, J. Weis, J. A. Mundy, D. A. Muller, H. Boschker, and J. Mannhart, *Adv. Mater. Interfaces* **1**, (2014), Link.

[176]   D. Bogorin, P. Irvin, C. Cen, and J. Levy, URL: `http://arxiv.org/abs/1011.5290` (2010).

[177]   F. Steglich, J. Aarts, C. D. Bredl, W. Lieke, D. Meschede, W. Franz, and H. Schäfer, *Phys. Rev. Lett.* **43**, 1892–1896 (1979), Link.

[178]   V. A. Sidorov, M. Nicklas, P. G. Pagliuso, J. L. Sarrao, Y. Bang, A. V. Balatsky, and J. D. Thompson, *Phys. Rev. Lett.* **89**, 157004 (2002), Link.

[179]   A. Bianchi, R. Movshovich, I. Vekhter, P. G. Pagliuso, and J. L. Sarrao, *Phys. Rev. Lett.* **91**, 257001 (2003), Link.

[180]   J. Paglione, M. A. Tanatar, D. G. Hawthorn, E. Boaknin, R. W. Hill, F. Ronning, M. Sutherland, L. Taillefer, C. Petrovic, and P. C. Canfield, *Phys. Rev. Lett.* **91**, 246405 (2003), Link.

[181]   Y. Mizukami, H. Shishido, T. Shibauchi, M. Shimozawa, S. Yasumoto, D. Watanabe, M. Yamashita, H. Ikeda, T. Terashima, H. Kontani, and Y. Matsuda, *Nat. Phys.* **7**, 849–853 (2011), Link.

[182]   H. Shishido, T. Shibauchi, K. Yasu, T. Kato, H. Kontani, T. Terashima, and Y. Matsuda, *Science* **327**, 980–983 (2010), Link.

[183]   Y. Kalychak, V. Zaremba, V. Baranyak, V. Bruskov, and P. Zavalii, *Russ. Metall.* , 213–215 (1989).

[184]   S. Fujimori, T. Okane, J. Okamoto, K. Mamiya, Y. Muramatsu, A. Fujimori, H. Harima, D. Aoki, S. Ikeda, H. Shishido, Y. Tokiwa, Y. Haga, and Y. Ōnuki, *Phys. Rev. B* **67**, 144507 (2003), Link.

[185]   T. Willers et al., *Phys. Rev. B* **81**, 195114 (2010), Link.

[186]   M. Daniel, S.-W. Han, C. H. Booth, A. L. Cornelius, P. G. Pagliuso, J. L. Sarrao, and J. D. Thompson, *Phys. Rev. B* **71**, 054417 (2005), Link.

[187]   C. H. Booth, T. Durakiewicz, C. Capan, D. Hurt, A. D. Bianchi, J. J. Joyce, and Z. Fisk, *Phys. Rev. B* **83**, 235117 (2011), Link.

[188]   S. Fujimori, A. Fujimori, K. Shimada, T. Narimura, K. Kobayashi, H. Namatame, M. Taniguchi, H. Harima, H. Shishido, S. Ikeda, D. Aoki, Y. Tokiwa, Y. Haga, and Y. Ōnuki, *Phys. Rev. B* **73**, 224517 (2006), Link.

[189]   A. Koitzsch, S. V. Borisenko, D. Inosov, J. Geck, V. B. Zabolotnyy, H. Shiozawa, M. Knupfer, J. Fink, B. Büchner, E. D. Bauer, J. L. Sarrao, and R. Follath, *Phys. Rev. B* **77**, 155128 (2008), Link.

[190]   J.-M. Imer and E. Wuilloud, *Z. Phys. B–Condens. Matter* **66**, 153–160 (1987), Link.

[191] C. Laubschat, E. Weschke, C. Holtz, M. Domke, O. Strebel, and G. Kaindl, *Phys. Rev. Lett.* **65**, 1639–1642 (1990), Link.

[192] H.-D. Kim, O. Tjernberg, G. Chiaia, H. Kumigashira, T. Takahashi, L. Duò, O. Sakai, M. Kasaya, and I. Lindau, *Phys. Rev. B* **56**, 1620–1624 (1997), Link.

[193] L. Braicovich, N. B. Brookes, C. Dallera, M. Salvietti, and G. L. Olcese, *Phys. Rev. B* **56**, 15047–15055 (1997), Link.

[194] O. Gunnarsson and K. Schönhammer, *Phys. Rev. B* **28**, 4315–4341 (1983), Link.

[195] P. W. Anderson, *Phys. Rev.* **124**, 41–53 (1961), Link.

[196] I.-K. Jeong, T. W. Darling, M. J. Graf, T. Proffen, R. H. Heffner, Y. Lee, T. Vogt, and J. D. Jorgensen, *Phys. Rev. Lett.* **92**, 105702 (2004), Link.

[197] A. V. Nikolaev and A. V. Tsvyashchenko, *Physics Uspekhi* **55**, 2 (2012).

[198] E. Wuilloud, H. R. Moser, W. Schneider, and Y. Baer, *Phys. Rev. B* **28**, 7354–7357 (1983), Link.

[199] J. C. Fuggle, F. U. Hillebrecht, Z. Zołnierek, R. Lässer, C. Freiburg, O. Gunnarsson, and K. Schönhammer, *Phys. Rev. B* **27**, 7330–7341 (1983), Link.

[200] L. Z. Liu, J. W. Allen, O. Gunnarsson, N. E. Christensen, and O. K. Andersen, *Phys. Rev. B* **45**, 8934–8941 (1992), Link.

[201] M. Gamza, A. Slebarski, and J. Deniszczyk, *J. Phys. Condens. Matter* **20**, 115202 (2008), Link.

[202] W.-D. Schneider, B. Delley, E. Wuilloud, J.-M. Imer, and Y. Baer, *Phys. Rev. B* **32**, 6819–6831 (1985), Link.

[203] J. Fink, *Adv. Electron. El. Phys.* **75**, 121–232 (1989), Link.

[204] A. Koitzsch, I. Opahle, S. Elgazzar, S. V. Borisenko, J. Geck, V. B. Zabolotnyy, D. Inosov, H. Shiozawa, M. Richter, M. Knupfer, J. Fink, B. Büchner, E. D. Bauer, J. L. Sarrao, and R. Follath, *Phys. Rev. B* **79**, 075104 (2009), Link.

[205] A. Koitzsch, T. K. Kim, U. Treske, M. Knupfer, B. Büchner, M. Richter, I. Opahle, R. Follath, E. D. Bauer, and J. L. Sarrao, *Phys. Rev. B* **88**, 035124 (2013), Link.

[206] E. Paparazzo, *Surf. Sci.* **234**, L253–L258 (1990), Link.

[207] W. Xiao, Q. Guo, and E. Wang, *Chem. Phys. Lett.* **368**, 527–531 (2003), Link.

[208] E. Bêche, P. Charvin, D. Perarnau, S. Abanades, and G. Flamant, *Surf. Interface Anal.* **40**, 264–267 (2008), Link.

[209] S. Tanuma, C. J. Powell, and D. R. Penn, *Surf. Interface Anal.* **35**, 268–275 (2003), Link.

Publications

[1] U. Treske, F. Ortmann, B. Oetzel, K. Hannewald, and F. Bechstedt: *Electronic and transport properties of graphene nanoribbons*, *Phys. Status Solidi A* **207**, 304–308 (2010), Link.

[2] F. Zhu, M. Grobosch, U. Treske, M. Knupfer, L. Huang, S. Ji, and D. Yan: *Interfacial energy level bending in a crystalline p/p-type organic heterostructure*, *Appl. Phys. Lett.* **98**, 203303 (2011), Link.

[3] F. Zhu, M. Grobosch, U. Treske, L. Huang, W. Chen, J. Yang, D. Yan, and M. Knupfer: *Hole Transparent and Hole Blocking Transport in Single-Crystal-Like Organic Heterojunction: When Rods Hold up Disks*, *ACS Appl. Mater. Interfaces* **3**, 2195–2199 (2011), Link.

[4] D. Haberer, C. E. Giusca, Y. Wang, H. Sachdev, A. V. Fedorov, M. Farjam, S. A. Jafari, D. V. Vyalikh, D. Usachov, X. Liu, U. Treske, M. Grobosch, O. Vilkov, V. K. Adamchuk, S. Irle, S. R. P. Silva, M. Knupfer, B. Buechner, and A. Grueneis: *Evidence for a New Two-Dimensional C_4H-Type Polymer Based on Hydrogenated Graphene*, *Adv. Mater.* **23**, 4497+ (2011), Link.

[5] S. Lindner, U. Treske, M. Grobosch, and M. Knupfer: *Charge transfer at $F_{16}CoPc$ and CoPc interfaces to Au*, *Appl. Phys. A* **105**, 921–925 (2011), Link.

[6] L. Huang, F. Zhu, C. Liu, U. Treske, M. Grobosch, H. Tian, J. Zhang, Y. Geng, M. Knupfer, and D. Yan: *Crystalline Organic Heterostructures Engineering Based on Vanadyl Phthalocyanine and Rod-Like Conjugated Organic Semiconductors with Selected Central Groups*, *Adv. Funct. Mater.* **22**, 4598–4607 (2012), Link.

[7] S. Lindner, U. Treske, and M. Knupfer: *The complex nature of phthalocyanine/gold interfaces*, *Appl. Surf. Sci.* **267**, 62–65 (2013), Link.

[8] A. Koitzsch, T. K. Kim, U. Treske, M. Knupfer, B. Büchner, M. Richter, I. Opahle, R. Follath, E. D. Bauer, and J. L. Sarrao: *Band-dependent emergence of heavy quasiparticles in $CeCoIn_5$*, *Phys. Rev. B* **88**, 035124 (2013), Link.

[9]   U. Treske, N. Heming, M. Knupfer, B. Büchner, A. Koitzsch, E. Di Gennaro, U. Scotti di Uccio, F. Miletto Granozio, and S. Krause: *Observation of strontium segregation in LaAlO$_3$/SrTiO$_3$ and NdGaO$_3$/SrTiO$_3$ oxide heterostructures by X-ray photoemission spectroscopy*, *APL Materials* **2**, 012108 (2014), Link.

[10] U. Treske, M. S. Khoshkhoo, F. Roth, M. Knupfer, E. D. Bauer, J. L. Sarrao, B. Büchner, and A. Koitzsch: *X-ray photoemission study of CeTIn$_5$ (T=Co, Rh, Ir)*, *J. Phys. Condens. Matter* **26**, 205601 (2014), Link.

[11] S. Lindner, B. Mahns, U. Treske, O. Vilkov, F. Haidu, M. Fronk, D. R. T. Zahn, and M. Knupfer: *Epitaxial growth and electronic properties of well ordered phthalocyanine heterojunctions MnPc/F$_{16}$CoPc*, *J. Chem. Phys.* **141**, 094706 (2014), Link.

[12] P. Philipp, L. Bischoff, U. Treske, B. Schmidt, J. Fiedler, R. Hübner, F. Klein, A. Koitzsch, and T. Mühl: *The origin of conductivity in ion-irradiated diamond-like carbon – Phase transformation and atomic ordering*, *Carbon*, pre–print: http://dx.doi.org/10.1016/j.carbon.2014.09.012 (2014), Link.

Danksagung

Selbstständigkeitserklärung

Hiermit versichere ich, dass ich die vorliegende Arbeit ohne unzulässige Hilfe Dritter und ohne Benutzung anderer als der angegebenen Hilfsmittel angefertigt habe; die aus fremden Quellen direkt oder indirekt übernommenen Gedanken sind als solche kenntlich gemacht. Die Arbeit wurde bisher weder im Inland noch im Ausland in gleicher oder ähnlicher Form einer anderen Prüfungsbehörde vorgelegt.

Die vorliegende Dissertation wurde unter der wissenschaftlichen Betreuung von Herrn Prof. Dr. B. Büchner im Institut für Festkörperforschung am Leibniz-Institut für Festkörper- und Werkstoffforschung in Dresden angefertigt.

Bis zum jetzigen Zeitpunkt habe ich keinerlei erfolglose Promotionsverfahren absolviert.

Ich erkenne die Promotionsordnung der Fakultät für Mathematik und Naturwissenschaften der Technischen Universität Dresden an.

Dresden, den 06.10.2014   _____

                                        Dipl.-Phys. Uwe Treske